



KOCAELI JOURNAL OF SCIENCE AND ENGINEERING

Owner

Prof. Dr. Nuh Zafer CANTÜRK - (Kocaeli University)

Editor in Chief

Dr. K. Süleyman YİĞİT - (Kocaeli University)

Editors

Dr. H. Hakan GÜREL - (Kocaeli University)

Dr. Mihriban CİVAN - (Kocaeli University)

Dr. Murat HOŞÖZ - (Kocaeli University)

Dr. Recep Kaya GÖKTAŞ - (Kocaeli University)

Production Editor

Lecturer Yusuf YAĞCI - (Kocaeli University)

Assistant Editors

Dr. Alp Eren ŞAHİN - (Kocaeli University)

Burak SEYYAR - (Kocaeli University)

Sevgi AYDIN - (Kocaeli University)

Büşra BERBEROĞLU - (Kocaeli University)

English Language Editors

Lecturer İsmail Hakkın PASLI - (Kocaeli University)

Secretary

Hüsnü TEMKİNER - (Kocaeli University)

Section Editors

Dr. Adnan SÖZEN (Gazi University)

Dr. Ahmet Ziyaettin ŞAHİN (KFUPM, S.A.)

Dr. Alaattin Metin KAYA (Bursa Uludağ University)

Dr. Aleksandrs SOSTAKS (University of Latvia)

Dr. Ata ATUN (Cyprus Science University)

Dr. Atakan ALKAN (Kocaeli University)

Dr. Ayşe Nilgün AKIN (Kocaeli University)

Dr. Bülent ORUÇ (Kocaeli University)

Dr. Cihan KARAKUZU (Bilecik Şeyh Edebali University)

Dr. Dong LI (Northeast Petroleum University)

Dr. Emre KİSHALI (Kocaeli University)

Dr. Engin ÖZDEMİR (Kocaeli University)

Dr. Erhan PULAT (Bursa Uludağ University)

Dr. Fatma GÜLTEKİN (Karadeniz Technical University)

Dr. Günay ÖZTÜRK (İzmir Demokrasi University)

Dr. Halil YİĞİT (Kocaeli University)

Dr. Halim Aytekin ERGÜL (Kocaeli University)

Dr. Hamid EL-QARNIA (Cadi Ayyad University)

Dr. Helena AZEVEDO (Queen Mary University of London)

Dr. Hüseyin Metin ERTUNÇ (Kocaeli University)

Dr. Iulian STANASEL (University of Oradea)

Dr. Kamaruzzaman SOPIAN (The National University of Malaysia)

Dr. Kerem KÜÇÜK (Kocaeli University)

Dr. Mehmet ARIK (Özyeğin University)

Dr. Mehmet Ufuk KASIM (Kocaeli University)

Dr. Müslüm ARICI (Kocaeli University)

Dr. Nilgün FİĞLALI (Kocaeli University)

Dr. Nurhan Turgut DUNFORD (Oklahoma State University)

Dr. Oscar CASTILLO (Tijuana Institute of Technology)

Dr. Recep Taygun GÜRAY (Kocaeli University)

Dr. Şaban Hakan ATAPEK (Kocaeli University)

Dr. Tahsin ENGİN (İTÜ)

Dr. Tamer SINMAZÇELİK (Kocaeli University)

Dr. Wang FUQIANG (Harbin Institute of Technology)

Dr. Yunus Emre ERDEMLİ (Kocaeli University)

Dr. Zerrin ALADAĞ (Kocaeli University)

Advisory Board

Dr. Ali KILIÇARSLAN (Hitit University)

Dr. Ali SÜRMEK (Uludağ University)

Dr. Ayşe Arzu ARI (Kocaeli University)

Dr. Burcu ONAT (Istanbul University)

Dr. Canan Dilek EREN (Kocaeli University)

Dr. Cenk SAYIN (Marmara University)

Dr. Fadime SERTÇELİK (Kocaeli University)

Dr. Hasan KÜRÜM (Fırat University)

Dr. Hikmet SÜRMEK (Mersin University)

Dr. Kasım BAYNAL (Kocaeli University)

Dr. Murat Selim ÇEPNİ (Kocaeli University)

Dr. Nil Pembe ÖZER (Kocaeli University)

Dr. Raşit KÖKER (Sakarya University)

Dr. Serdar İPLİKÇİ (Pamukkale University)

Dr. Sezai TOKAT (Pamukkale University)

Dr. Şeref Naci ENGİN (Yıldız Technical University)

Dr. Mustafa ÇANAKCI (Kocaeli University)

Printed By

Kocaeli University - Graduate School of Natural and Applied Sciences - Umuttepe Campus 41001, Kocaeli / TURKEY

Tel: +090 (262) 303 35 56 Fax: +090 (262) 303 30 33 E-mail: kojose@kocaeli.edu.tr



COVER PAGE	I
EDITORIAL AND ADVISORY BOARDS	II
TABLE OF CONTENTS	III

Süleyman ÇETİNKAYA, Ali DEMİR

On the Solution of Mathematical Model Including Space-Time Fractional Diffusion Equation in Conformable Derivative, Via Weighted Inner Product..... 1-6
(*Research Paper*)

Babak KARIMI

Finite Element Modeling of a Stone Layer Under a Strip Footing to Estimate Soil Behavior and Determine Optimal Stone Layer Width and Depth..... 7-12
(*Research Paper*)

Mehmet ÖZÇELİK

The Benefits of Uncertainty and Risk Assessment Studies on the M5 Metro Line (Istanbul - Turkey)..... 13-25
(*Research Paper*)

Selman CAGMAN, Aşkın YILDIZ, Alpaslan GÜVEN, Ümit ÜNVER

Energy Efficiency Research In Fans and Experimental Investigation of the Effect of Motor Frequency..... 26-34
(*Research Paper*)

Emin ÖLMEZ, Orhan AKBULUT, Ahmet SERTTAŞ

A Low-Dimensional Feature Vector Representation for Gait-based
Parkinson's Disease Detection 35-43
(Research Paper)

Sertaç ERMAN

Undetermined Coefficients Method for Sequential Fractional Differential Equations 44-50
(Research Paper)

Ogün BOZKAYA

Chemical Characterization of Ultra High Molecular Weight Polyethylene
Based Tibial Inserts After Ethylene Oxide Sterilization 51-60
(Research Paper)

Mustafa Murat YAVUZ, Nurbanu ERDAL

Investigation of The Effect of Knitting Row on Vibration Structure for A Wide
Chimney Made With Brick Bar 61-68
(Research Paper)

Yıldız UYGUN CEBECİ



Design, Synthesis, and Biological Evaluation of 1,2,4-Triazole Derivatives
as Potential Antimicrobial Agents 69-77
(Research Paper)

Cihan KARAKUZU, Emin TOPAL

Optimization of Traffic Network Signal Durations with Heuristic Algorithm
and the Effect of Number of Individuals 78-88
(Research Paper)



On the Solution of Mathematical Model Including Space-Time Fractional Diffusion Equation in Conformable Derivative, Via Weighted Inner Product

Suleyman CETINKAYA ^{1,*} , Ali DEMIR ² 

¹ Department of Mathematics, Kocaeli University, Kocaeli, 41001, Turkey, **ORCID:** 0000-0002-8214-5099

² Department of Mathematics, Kocaeli University, Kocaeli, 41001, Turkey, **ORCID:** 0000-0003-3425-1812

Article Info

Research paper

Received : February 18, 2022

Accepted : July 22, 2022

Keywords

Conformable fractional derivative.
Initial-boundary-value problems.
Space-time fractional differential equation.
Spectral method.

Abstract

This research aims to accomplish an analytic solution to mathematical models involving space-time fractional differential equations in the conformable sense in series form through the weighted inner product and separation of variables method. The main advantage of this method is that various linear problems of any kind of differential equations can be solved by using this method. First, the corresponding eigenfunctions are established by solving the Sturm-Liouville eigenvalue problem. Secondly, the coefficients of the eigenfunctions are determined by employing weighted inner product and initial condition. Thirdly, the analytic solution to the problem is constructed in the series form. Finally, an illustrative example is presented to show how this method is implemented for fractional problems and exhibit its effectiveness and accuracy.

1. Introduction

Since the role of fractional partial differential equations has come into prominence, the focus of numerous scientists in various fields is directed to this subject. As a result, fractional differential equations are employed in the modeling of processes in diverse research areas such as applied mathematics, physics chemistry, power systems, control theory, system theory, optimization, signal processing, epidemic model of childhood disease, epidemic system of HIV/AIDS transmission etc., [1-13]. The main reason for this increase in interest is that the fractional derivative is a non-local operator, which allows us to analyze the behavior of the complex non-linear processes much better than by using the alternatives.

Dealing with fractional derivatives is more complicated than ordinary derivatives as several difficulties are encountered when solving fractional

differential equations. Essential properties of ordinary derivatives such as the product rule and the chain rule are not held by the majority of the fractional derivatives. However, conformable fractional derivative holds almost all properties of ordinary derivative, which allows us to handle and accomplish the solution of mathematical models, including fractional differential equations in the conformable sense without any difficulty [14-16]. Therefore, in this research, we look for the solution to models given in the following form :

$$\frac{\partial^\alpha u(x,t;\alpha,\beta)}{\partial t^\alpha} = A \frac{\partial^{2\beta} u(x,t;\alpha,\beta)}{\partial x^{2\beta}} + B \frac{\partial^\beta u(x,t;\alpha,\beta)}{\partial x^\beta} + C \quad (1)$$

$$u(0,t) = u(L,t) = 0, \quad (2)$$

$$u(x,0) = f(x,\beta), \quad (3)$$

where $0 \leq x \leq L$, $0 \leq t \leq T$, $0 < \alpha \leq 1$, $1 < 2\beta \leq 2$, $A, B, C \in R$, $A \neq 0$.

The primary motivation for this study is the fact that diverse scientific processes are modeled by fractional diffusion equations. Subsequently, solving this kind of fractional diffusion problem has drawn the attention of

* Corresponding Author: suleyman.cetinkaya@kocaeli.edu.tr



many scientists in various branches.

2. Preliminary Results

The definition and fundamental properties of the conformable fractional derivative are presented in this section.

Definition: The conformable fractional derivative of function $f(x)$ for $0 < \alpha \leq 1$ is introduced as follows [11]:

$$\frac{d^\alpha f(x)}{dx^\alpha} = \frac{f(x+\epsilon x^{1-\alpha})-f(x)}{\epsilon}.$$

We list fundamental properties of the conformable fractional derivatives of certain functions as:

1. If f is differentiable then $\frac{d^\alpha}{dx^\alpha} f(x) = x^{1-\alpha} \frac{d}{dx} f(x)$.
2. $\frac{d^\alpha}{dx^\alpha} (af(x) + bg(x)) = a \frac{d^\alpha f(x)}{dx^\alpha} + b \frac{d^\alpha g(x)}{dx^\alpha}$.
3. $\frac{d^\alpha}{dx^\alpha} (x^p) = px^{p-\alpha}$ for all $p \in \mathbb{R}$.
4. $\frac{d^\alpha}{dx^\alpha} (f(x)g(x)) = f(x) \frac{d^\alpha g(x)}{dx^\alpha} + g(x) \frac{d^\alpha f(x)}{dx^\alpha}$.
5. $\frac{d^\alpha}{dx^\alpha} \left(\frac{f(x)}{g(x)} \right) = \frac{g(x) \frac{d^\alpha f(x)}{dx^\alpha} - f(x) \frac{d^\alpha g(x)}{dx^\alpha}}{g^2(x)}$.
6. $\frac{d^\alpha}{dx^\alpha} (\lambda) = 0$, for all constant functions $f(x) = \lambda$.

Additionally, the conformable fractional derivative of basic functions are computed in the following form:

$$\begin{aligned} \frac{d^\alpha}{dx^\alpha} x^p &= px^{p-\alpha}, \\ \frac{d^\alpha}{dx^\alpha} \sin\left(\frac{1}{\alpha} x^\alpha\right) &= \cos\left(\frac{1}{\alpha} x^\alpha\right), \\ \frac{d^\alpha}{dx^\alpha} \cos\left(\frac{1}{\alpha} x^\alpha\right) &= -\sin\left(\frac{1}{\alpha} x^\alpha\right), \\ \frac{d^\alpha}{dx^\alpha} \exp\left(\frac{1}{\alpha} x^\alpha\right) &= \exp\left(\frac{1}{\alpha} x^\alpha\right). \end{aligned}$$

Notice that the corresponding ordinary derivatives of the functions given above are obtained for $\alpha = 1$.

Even though some functions such as $f(x) = 2\sqrt{x}$ are not differentiable, they could be α -differentiable in the conformable sense, for example, $\frac{d^{\frac{1}{2}} f(x)}{dx^{\frac{1}{2}}} = 1$ and $\frac{d^{\frac{1}{2}} f(0)}{dx^{\frac{1}{2}}} = 1$.

This is another distinct property of conformable fractional derivative.

3. Main Results

By means of the separation of variables method, the generalized solution to problem (1)-(3) is constructed in the following form:

$$u(x, t; \alpha, \beta) = X(x; \beta) T(t; \alpha, \beta) \tag{4}$$

where $0 \leq x \leq L, 0 \leq t \leq T$.

As indicated above, the function X depends on the spatial fractional order β , while the function T depends on both time and spatial fractional orders α and β , respectively.

Substituting (4) into (1) and rearranging yields

$$\frac{d^\alpha T(t; \alpha, \beta)}{dt^\alpha} \frac{1}{T(t; \alpha, \beta)} = A \frac{d^{2\beta} X(x; \beta)}{dx^{2\beta}} \frac{1}{X(x; \beta)} + B \frac{d^\beta X(x; \beta)}{dx^\beta} \frac{1}{X(x; \beta)} + C = -\lambda(\beta) \tag{5}$$

Notice that λ is a function of β . Taking equation (5) into account, two fractional differential equations of unknown functions X and T are obtained separately. The fractional differential equation of X subject to the boundary conditions is given as follows:

$$A \frac{d^{2\beta} X(x; \beta)}{dx^{2\beta}} \frac{1}{X(x; \beta)} + B \frac{d^\beta X(x; \beta)}{dx^\beta} \frac{1}{X(x; \beta)} + \lambda(\beta) X(x; \beta) = 0, \tag{6}$$

$$X(0; \beta) = X(L; \beta) = 0. \tag{7}$$

This problem is called the fractional Sturm-Liouville problem, and its solutions are obtained by applying the exponential function in the following form:

$$X(x; \beta) = \exp\left(r \frac{x^\beta}{\beta}\right). \tag{8}$$

This yields the following characteristic equation:

$$Ar^2 + Br + \lambda(\beta) = 0. \tag{9}$$

In order to solve this equation, the following 3 cases are taken into account:

Case 1, $B^2 - 4A\lambda(\beta) > 0$:

There are two real and distinct solutions r_1, r_2 providing the solution to problem (6)-(7) in the following form:

$$X(x; \beta) = c_1 \exp\left(r_1 \frac{x^\beta}{\beta}\right) + c_2 \exp\left(r_2 \frac{x^\beta}{\beta}\right).$$

First boundary condition yields

$$X(0; \beta) = c_1 + c_2 = 0 \implies c_2 = -c_1. \tag{10}$$

Hence, the solution becomes

$$X(x; \beta) = c_1 \left(\exp\left(r_1 \frac{x^\beta}{\beta}\right) - \exp\left(r_2 \frac{x^\beta}{\beta}\right) \right). \tag{11}$$

Similarly, last boundary condition yields

$$X(L; \beta) = c_1 \left(\exp \left(r_1 \frac{L^\beta}{\beta} \right) - \exp \left(r_2 \frac{L^\beta}{\beta} \right) \right) = 0, \quad (12)$$

which indicates that

$$\exp \left(r_1 \frac{L^\beta}{\beta} \right) \neq \exp \left(r_2 \frac{L^\beta}{\beta} \right). \quad (13)$$

As a result, we have

$$c_1 = 0 \quad (14)$$

which implies that there is no solution for Case 1.

Case 2, $B^2 - 4A\lambda(\beta) = 0$:

There is a corresponding coincident as the solutions are equal $r_1 = r_2$, which provides the solution to problem (6)-(7) in the following form:

$$X(x; \beta) = c_1 \exp \left(r_1 \frac{x^\beta}{\beta} \right) + c_2 \frac{x^\beta}{\beta} \exp \left(r_1 \frac{x^\beta}{\beta} \right). \quad (15)$$

First boundary condition yields

$$X(0) = c_1 = 0. \quad (16)$$

Hence the solution becomes

$$X(x; \beta) = c_2 \frac{x^\beta}{\beta} \exp \left(r_1 \frac{x^\beta}{\beta} \right). \quad (17)$$

Similarly last boundary condition yields

$$X(L) = c_2 \frac{L^\beta}{\beta} \exp \left(r_1 \frac{L^\beta}{\beta} \right) \Rightarrow c_2 = 0, \quad (18)$$

which implies that there is no solution for Case 2.

Case 3, $B^2 - 4A\lambda(\beta) < 0$:

There are two complex roots $-\frac{B}{2A} \pm i \frac{\sqrt{4A\lambda(\beta) - B^2}}{2A}$ which provides the solution to problem (6)-(7) in the following form:

$$X(x; \beta) = \exp \left(-\frac{B}{2A} \frac{x^\beta}{\beta} \right) \left[c_1 \cos \left(\frac{\sqrt{4A\lambda(\beta) - B^2}}{2A} \frac{x^\beta}{\beta} \right) + c_2 \sin \left(\frac{\sqrt{4A\lambda(\beta) - B^2}}{2A} \frac{x^\beta}{\beta} \right) \right]. \quad (19)$$

First boundary condition yields

$$X(0; \beta) = c_1 = 0 \quad (20)$$

Hence the solution becomes

$$X(x; \beta) = c_2 \exp \left(-\frac{B}{2A} \frac{x^\beta}{\beta} \right) \sin \left(\frac{\sqrt{4A\lambda(\beta) - B^2}}{2A} \frac{x^\beta}{\beta} \right). \quad (21)$$

Similarly last boundary condition yields

$$X(L) = c_2 \exp \left(-\frac{B}{2A} \frac{L^\beta}{\beta} \right) \sin \left(\frac{\sqrt{4A\lambda(\beta) - B^2}}{2A} \frac{L^\beta}{\beta} \right) = 0 \quad (22)$$

which indicates that

$$\sin \left(\frac{\sqrt{4A\lambda(\beta) - B^2}}{2A} \frac{L^\beta}{\beta} \right) = 0. \quad (23)$$

Hence the corresponding eigenvalues become

$$\lambda_n(\beta) = \frac{(2n\pi\beta A)^2 + B^2 L^{2\beta}}{4AL^{2\beta}}, \quad 0 < \lambda_1(\beta) < \lambda_2(\beta) < \lambda_3(\beta) \dots \quad (24)$$

As a result, the solution to the problem (6)-(7) is concluded in the following form:

$$X_n(x; \beta) = \exp \left(-\frac{B}{2A} \frac{x^\beta}{\beta} \right) \sin \left(n\pi \frac{x^\beta}{L^\beta} \right), \quad n = 1, 2, 3, \dots \quad (25)$$

The fractional differential equation of T for each eigenvalue $\lambda_n(\beta)$ is given as follows:

$$\frac{d^\alpha T(t; \alpha, \beta)}{dt^\alpha} = (C - \lambda(\beta))T(t; \alpha, \beta) \quad (26)$$

which has the following solutions

$$T_n(t; \alpha, \beta) = \exp \left(\left(C - \frac{(2n\pi\beta A)^2 + B^2 L^{2\beta}}{4AL^{2\beta}} \right) \frac{t^\alpha}{\alpha} \right), \quad n = 1, 2, 3, \dots \quad (27)$$

Hence the function corresponding to each eigenvalue $\lambda_n(\beta)$ is defined as

$$u_n(x, t; \alpha, \beta) = \exp \left(\left(C - \frac{(2n\pi\beta A)^2 + B^2 L^{2\beta}}{4AL^{2\beta}} \right) \frac{t^\alpha}{\alpha} \right) \exp \left(-\frac{B}{2A} \frac{x^\beta}{\beta} \right) \sin \left(n\pi \frac{x^\beta}{L^\beta} \right) \quad (28)$$

which satisfies equation (1) and boundary conditions but not the initial condition. In order to acquire the solution to problem (1)-(3), we construct the following series

$$u(x, t; \alpha, \beta) = \sum_{n=1}^{\infty} d_n \exp \left(\left(C - \frac{(2n\pi\beta A)^2 + B^2 L^{2\beta}}{4AL^{2\beta}} \right) \frac{t^\alpha}{\alpha} \right) \exp \left(-\frac{B}{2A} \frac{x^\beta}{\beta} \right) \sin \left(n\pi \frac{x^\beta}{L^\beta} \right) \quad (29)$$

which also satisfies both the fractional equation (1) and boundary condition (2). In order to make this solution satisfy the initial condition (3), we must determine the coefficients d_n accurately. Taking the initial condition (3), we get

$$u(x, 0) = \sum_{n=1}^{\infty} d_n \exp \left(-\frac{B}{2A} \frac{x^\beta}{\beta} \right) \sin \left(n\pi \frac{x^\beta}{L^\beta} \right) = f(x; \beta) \exp \left(-\frac{B}{2A} \frac{x^\beta}{\beta} \right). \quad (30)$$

Utilizing the weighted inner product, the coefficients d_n are computed for $n = 1, 2, 3, \dots$ as follows:

$$d_n = \frac{2\beta}{L^\beta} \int_0^L f(x; \beta) \sin \left(n\pi \frac{x^\beta}{L^\beta} \right) \frac{1}{x^{1-\beta}} dx, \quad n = 1, 2, 3, \dots \quad (31)$$

where the weighted inner product of two functions $f(x), g(x)$ is defined as follows:

$$\langle f(x), g(x) \rangle = \frac{2\beta}{L^\beta} \int_0^L f(x)g(x) \exp \left(\frac{B}{A} \frac{x^\beta}{\beta} \right) \frac{1}{x^{1-\beta}} dx.$$

4. Illustrative Example

In this section, we present an example to illustrate how to implement the method explained in this study and to acquire the solution via this method.

Firstly, we consider the following initial boundary value problem with integer-order derivatives:

$$u_t(x, t) = u_{xx}(x, t) + u_x(x, t) - u(x, t), \quad (32)$$

$$u(0, t) = 0, u(2, t) = 0, \quad (33)$$

$$u(x, 0) = \sin \left(\frac{\pi}{2} x \right) \exp \left(-\frac{1}{2} x \right), \quad (34)$$

which has the solution in the following form:

$$u(x, t) = \sin \left(\frac{\pi}{2} x \right) \exp \left(-\frac{1}{2} x \right) \exp \left(-\left(\frac{\pi^2}{4} + \frac{5}{4} \right) t \right) \quad (35)$$

where $0 \leq x \leq 2, t \geq 0$.

Now, take the same problem with space and time fractional derivatives:

$$\frac{\partial^\alpha u(x, t; \alpha, \beta)}{\partial t^\alpha} = \frac{\partial^{2\beta} u(x, t; \alpha, \beta)}{\partial x^{2\beta}} + \frac{\partial^\beta u(x, t; \alpha, \beta)}{\partial x^\beta} - u(x, t; \alpha, \beta), \quad (36)$$

$$u(0, t; \alpha, \beta) = u(2, t; \alpha, \beta) = 0, \quad (37)$$

$$u(x, 0; \alpha, \beta) = \sin \left(\pi \frac{x^\beta}{2^\beta} \right) \exp \left(-\frac{1}{2} \frac{x^\beta}{\beta} \right), \quad (38)$$

where $0 < \alpha \leq 1, 1 < 2\beta \leq 2, 0 \leq x \leq 2, 0 \leq t \leq T$.

Carrying out the separation of the variables to (36) yields

$$\frac{d^\alpha T(t; \alpha, \beta)}{dt^\alpha} \frac{1}{T(t; \alpha, \beta)} = \frac{d^{2\beta} X(x; \beta)}{dx^{2\beta}} \frac{1}{X(x; \beta)} + \frac{d^\beta X(x; \beta)}{dx^\beta} \frac{1}{X(x; \beta)} - 1 = -\lambda(\beta) \quad (39)$$

which has the corresponding fractional Sturm-Liouville problem:

$$\frac{d^{2\beta} X(x; \beta)}{dx^{2\beta}} + \frac{d^\beta X(x; \beta)}{dx^\beta} + \lambda(\beta) X(x; \beta) = 0, \quad (40)$$

$$X(0; \beta) = X(2; \beta) = 0. \quad (41)$$

The corresponding eigenvalues $\lambda_n(\beta)$ and solutions $X_n(x; \beta)$ to the problem (40)-(41) for $n = 1, 2, 3, \dots$ are acquired in the following form:

$$\lambda_n(\beta) = \frac{(2n\pi\beta)^2 + 2^{2\beta}}{4 \cdot 2^{2\beta}}, \quad 0 < \lambda_1(\beta) < \lambda_2(\beta) < \lambda_3(\beta) < \dots \quad (42)$$

$$X_n(x; \beta) = \exp \left(-\frac{1}{2} \frac{x^\beta}{\beta} \right) \sin \left(n\pi \frac{x^\beta}{2^\beta} \right). \quad (43)$$

The fractional differential equation of T for each eigenvalue $\lambda_n(\beta)$ is given as follows:

$$\frac{d^\alpha T(t; \alpha, \beta)}{dt^\alpha} = \left(-1 - \frac{(2n\pi\beta)^2 + 2^{2\beta}}{4 \cdot 2^{2\beta}} \right) T(t; \alpha, \beta). \quad (44)$$

The solution of which becomes

$$T_n(t; \alpha, \beta) = \exp \left(\left(-1 - \frac{(2n\pi\beta)^2 + 2^{2\beta}}{4 \cdot 2^{2\beta}} \right) \frac{t^\alpha}{\alpha} \right), \quad n = 1, 2, 3, \dots \quad (45)$$

Therefore, the specific solutions to problem (36)-(38) for $n = 1, 2, 3, \dots$ are in the following form:

$$u_n(x, t; \alpha, \beta) = \exp \left(\left(-1 - \frac{(2n\pi\beta)^2 + 2^{2\beta}}{4 \cdot 2^{2\beta}} \right) \frac{t^\alpha}{\alpha} \right) \exp \left(-\frac{1}{2} \frac{x^\beta}{\beta} \right) \sin \left(n\pi \frac{x^\beta}{2^\beta} \right). \quad (46)$$

As a result, the general solution to problem (36)-(38) becomes

$$u(x, t; \alpha, \beta) = \sum_{n=1}^{\infty} d_n \exp \left(\left(-1 - \frac{(2n\pi\beta)^2 + 2^{2\beta}}{4 \cdot 2^{2\beta}} \right) \frac{t^\alpha}{\alpha} \right) \exp \left(-\frac{1}{2} \frac{x^\beta}{\beta} \right) \sin \left(n\pi \frac{x^\beta}{2^\beta} \right). \quad (47)$$

In order to determine the unknown coefficients d_n , we plug $t = 0$ into the general solution (47) and proceed taking the initial condition (38) into account:

$$u(x, 0) = \sum_{n=1}^{\infty} d_n \exp\left(-\frac{1}{2} \frac{x^\beta}{\beta}\right) \sin\left(n\pi \frac{x^\beta}{2\beta}\right) = \sin\left(\pi \frac{x^\beta}{2\beta}\right) \exp\left(-\frac{1}{2} \frac{x^\beta}{\beta}\right). \tag{48}$$

Through the inner product, the coefficients d_n for $n = 1, 2, 3, \dots$ are determined as

$$d_n = \frac{2\beta}{2\beta} \int_0^2 \sin\left(\pi \frac{x^\beta}{2\beta}\right) \exp\left(-\frac{1}{2} \frac{x^\beta}{\beta}\right) \exp\left(-\frac{1}{2} \frac{x^\beta}{\beta}\right) \sin\left(n\pi \frac{x^\beta}{2\beta}\right) \exp\left(\frac{x^\beta}{\beta}\right) dx$$

After rearrangement, we have

$$d_n = \frac{2\beta}{2\beta} \int_0^2 \sin\left(\pi \frac{x^\beta}{2\beta}\right) \sin\left(n\pi \frac{x^\beta}{2\beta}\right) \frac{1}{x^{1-\beta}} dx.$$

Orthogonality property provides us that $d_n = 0$ for $n \neq 1$ and for $n = 1$, therefore we get

$$d_1 = \frac{2\beta}{2\beta} \int_0^2 \left(\pi \frac{x^\beta}{2\beta}\right) \frac{1}{x^{1-\beta}} dx = 1.$$

Thus the general solution to the time-space fractional problem is obtained in the following form:

$$u(x, t; \alpha, \beta) = \exp\left(-1 - \frac{(2\pi\beta)^2 + 2^{2\beta}}{4.2^{2\beta}} \frac{t^\alpha}{\alpha}\right) \exp\left(-\frac{1}{2} \frac{x^\beta}{\beta}\right) \sin\left(\pi \frac{x^\beta}{2\beta}\right). \tag{49}$$

Notice that as fractional orders α and β gets close to 1, the solution (49) to the time-space fractional problem (36)-(38) approaches to the solution (35) of the corresponding initial boundary value problem (32)-(34). This points to the accuracy of the obtained solution.

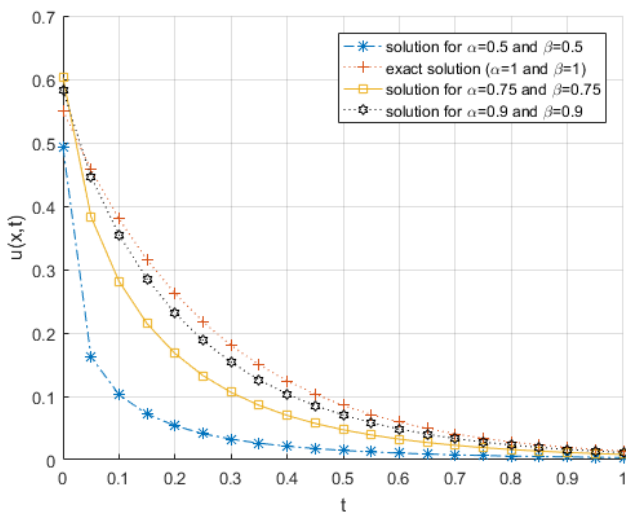


Figure 1. The graph of solutions $x = 0.5$ for various values of α and β .

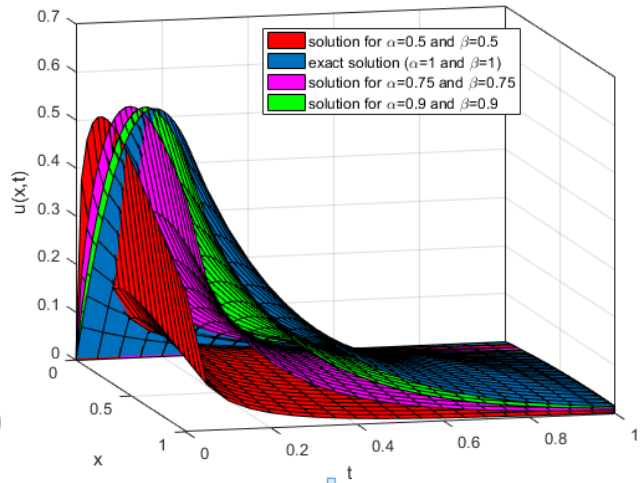


Figure 2. 3D graphs of solutions for various values of α and β .

5. Conclusions

In this research, analytic solutions to space-time fractional problems are calculated by means of the separation of variables method and inner product in one dimension. As the application of this method to initial boundary value problems of ordinary derivatives is performed, the corresponding Sturm-Liouville problem is taken into account to determine the eigenvalues of the problem, and then specific solutions are formed. Finally, with the help of the initial condition and orthogonality of the inner product, the general solution to the problem is acquired. An illustrative example is also provided to prove the effectiveness of the method for space-time fractional differential equations.

In future studies, fuzzy space-time fractional problems will be considered as other applications of this method.

Declaration of Ethical Standards

The authors of this article declare that the materials and methods used in this study do not require ethical committee permission and/or legal-special permissions.

Conflict of Interest

The authors declare that they have no known competing financial interests or personal relationships that could have appeared to influence the work reported in this paper.

References

- [1] Cetinkaya S., Demir A., 2021. Numerical Solutions of Nonlinear Fractional Differential Equations via Laplace Transform. *Facta Universitatis Ser. Math. Inform*, **36**(2), pp. 249-257.
- [2] Cetinkaya S., Demir A., Baleanu D., 2021. Analysis of Fractional Fokker-Planck Equation with Caputo and Caputo-Fabrizio derivatives. *Annals of the University of Craiova, Mathematics and Computer Science Series*, **48**(2), pp. 334-348.
- [3] Cetinkaya S., Demir A., 2021. On the Solution of Bratu's Initial Value Problem in the Liouville-Caputo Sense by ARA Transform and Decomposition Method. *Comptes rendus de l'Academie bulgare des Sciences*, **74**(12), pp. 1729-1738.
- [4] Kodal Sevindir H., Cetinkaya S., Demir A., 2021. On Effects of a New Method for Fractional Initial Value Problems. *Advances in Mathematical Physics*, **2021**, Article ID 7606442.
- [5] Cetinkaya S., Demir A., Kodal Sevindir, H., 2021. Solution of Space-Time Fractional Problem by Shehu Variational Iteration Method. *Advances in Mathematical Physics*, **2021**, Article ID 5528928.
- [6] Cetinkaya S., Demir A., 2021. On Solutions of Hybrid Time Fractional Heat Problem. *Bulletin of the Institute of Mathematics Academia Sinica New Series*, **16**(1), pp. 49-62.
- [7] Podlubny I., 1999. *Fractional Differential Equations*, Academic Press.
- [8] Kilbas A. A., Srivastava H. M., Trujillo J. J., 2006. *Theory and Applications of Fractional Differential Equations*, Elsevier.
- [9] Miller K. S., 1993. *An Introduction to Fractional Calculus and Fractional Differential Equations*, J. Wiley and Sons.
- [10] Oldham K., Spanier J., 1974. *The Fractional Calculus, Theory and Applications of Differentiation and Integration of Arbitrary Order*, Academic Press.
- [11] Gao W., Günerhan H., Başkonuş H.M., 2020. Analytical and approximate solutions of an epidemic system of HIV/AIDS transmission. *Alexandria Engineering Journal*, **59**(5), pp. 3197-3211.
- [12] Srivastava H.M., Günerhan H., 2019. Analytical and approximate solutions of fractional-order susceptible-infected-recovered epidemic model of childhood disease. *Mathematical Methods in the Applied Sciences*, **42**, pp. 935-941.
- [13] Dutta H., Günerhan H., Ali K.K, Yilmazer R., 2020. Exact Soliton Solutions to the Cubic-Quartic Non-linear Schrödinger Equation With Conformable Derivative. *Frontiers in Physics*, **8**, pp. 1-7.
- [14] Khalil R., Al Horani M., Yousef A., Sababheh M., 2014. A new definition of fractional derivative. *J. Comput. Appl. Math.*, **264**, pp. 65-70.
- [15] Abdeljawad T., On conformable fractional calculus. *J. Comput. Appl. Math.*, **279**, pp. 57-66.
- [16] Abu Hammad M., Khalil R., 2014. Conformable fractional heat differential equation. *International Journal of Pure and Applied Mathematics*, **94**(2), pp. 215-221.



Finite Element Modeling of a Stone Layer Under a Strip Footing to Estimate Soil Behavior and Determine Optimal Stone Layer Width and Depth

Babak KARIMI^{1,*}

¹ Department of Civil Engineering, Erzurum Technical University, Erzurum, 25050, Türkiye, **ORCID:** 0000-0001-7897-9085

Article Info

Research paper

Received : May 27, 2022

Accepted : August 3, 2022

Keywords

FEM
Finite Element Method
Plaxis
Soil Improvement

Abstract

Various methods can be applied to improve soil behavior in order to increase the bearing capacity or reduce the settlement of footings. These methods can be categorized as stabilization or improvement of soil by use of different geosynthetics; injection methods; grouting or replacing weak soil with stronger materials. One of the most common methods and materials that can be used for improving soils, is placing a stone layer under the footing. In this study, a stone layer under a strip footing is simulated with the finite element method (FEM) to estimate the soil behavior in different conditions. A strip footing with a width of 1m and length of 8m with a 100 kN/m² uniform load was modelled. Different widths of stone layer from 1B to 3B (B was the strip footing width) with different depths of 0.5B, 1B, 1.5B, and 2B were modelled in Plaxis 3D and results were obtained from the simulation. By reviewing the results, it was found that the optimum dimensions of the stone layer to place under the presented strip footing was 2B width and 1B depth. This result can be applied to real projects with similar conditions.

1. Introduction

Having more settlement and less bearing capacity of soil is the most common problem in foundation applications. There are different methods and strategies in use to improve soil bearing capacity or settlement of footing in weak soils. For example, improving soils by injection or grouting, piles, stone columns, compaction or using stone layers under footing can be applied as some alternative procedures for improving soil properties to increase bearing capacity or reduce the settlement of soil [1].

Plastic piles, stone blockage, and stone columns are some of the most common methods used in recent years to improve the soil structure. Several theoretical and experimental studies were done to simulate and test various methods to evaluate the soil behavior under different conditions of dimension and loading [2-4].

Improving the soil and creating a stronger layer under the footing is one of the methods that can be used to

improve the geotechnical properties of soil under footings. This stronger layer will transfer the loads to the under layers and will positively affect the shear failure surfaces and bearing capacity of the soil. Additionally, it can also reduce the vertical and lateral displacements of soil. Different methods and materials can be used for improving the soil [5-8]. Fiber reinforced soils, geosynthetic-reinforced soils, and compaction in a variety of ways [9-11] can be given as examples. There are different numerical methods to understand the soil's behavior at different conditions. The Finite element method (FEM) is one of the most commonly used methods for simulating geotechnical problems. Different conditions and materials can be modelled with different software[12-14].

The type of soil and foundation must be taken into consideration when selecting the improvement method. Experiments can be carried out on both granular and fine cohesive soils. In a study, direct shear tests were applied to study the mechanisms of fiber reinforcement [15]. Different materials were used for reinforcing the soil, for example, granular soils were reinforced with fiber to investigate the effects of reinforcement [16]. Results of this work showed that the reinforcement of granular soil with

* Corresponding Author: babak.karimi@erzurum.edu.tr



fiber was more effective in fine graded than in medium-grained sands. At the same time, the effect of reinforcement was more considerable with sub-rounded particles in comparison to sub-angular particles [16].

One of the methods that can be applied to weak soil with engineering problems is removing the weak soil and replacing it with stronger soil or materials. In this case, the weak layer of soil under the footing can be replaced with a stone layer at a different depth and width. In this study, a strip footing lying on weak soil was modeled with the Plaxis 3D software, and weak soil under the footing was replaced with a strong stone layer to obtain the optimum depth and width of the new replaced stone mass.

2. Materials and Methods

In this study, three kinds of soil materials were used for modelling and simulation. A soft, weak, sandy soil, a stone mat used beneath the footing as a stone layer, and concrete for the footing. The Mohr-Coulomb model was used to simulate the sand and stone in the drained condition that has been used in similar previous studies [17-19]. As the stone blockage is not massive rock and the behaviour of this improved layer is not similar to rock with cracks inside rock mass or stone blocks, Mohr-Coulomb was chosen for material type in the simulation. A strip footing with a dimension of 1*8 m was modeled in this study. The footing was put on a drained, weak sandy soil. A 100 kN/m² uniform load was applied to the model footing, and the maximum vertical settlement and shear failure mechanism of the soil under the footing were investigated. At the next step, weak soil under footing was replaced with a stone layer with different depths and width, and the behavior, shear failure mechanism, and settlements were compared with normal conditions. Plaxis 3D finite

element software was used for modeling the footing, soil, and stone.

The finite element method was developed for simulating various engineering analyses for modeling and analyzing complex systems in the area of civil and mechanical engineering. Seven material parameters are used to define the materials associated with this model, namely unsaturated unit weight (γ_{unsat}), saturated unit weight (γ_{sat}), Young's modulus (E), Poisson's ratio (ν), effective friction angle (ϕ'), effective cohesion (c') and dilation angle (ψ). A stone layer is defined as a uniformly drained soil material. The footing used for the simulation was a rigid concrete footing with a thickness of 80 cm. The soil used for the modeling was a weak soil that caused big settlements under loading of footing. The properties of footing, soil, and stone are presented in Table 1.

A strip footing was simulated with FEM. The width (B) and length (L) of the footing are 1 and 8 m, respectively. The first simulation was done without any stone layer under the footing, and vertical deformation of soil and shear failure surfaces were obtained. Then a strong stone layer with a width of strip footing (B) and a depth of 0.5B was placed under the footing and simulated again. After that, by increasing the depth of the stone layer, a strip footing was modeled with a stone layer of 1B, 1.5B, and 2B. At the next step, the width of the stone layer was increased on two sides. This increment was 0.5B and 1B on each side. In other words, four different depths of 0.5B, 1B, 1.5B, and 2B with three different widths of B, 2B, and 3B of stone layer were simulated under a strip footing with constant width and uniform loading. And finally, maximum deformation and soil behavior at each condition were studied. The schematic shape of the foundation and stone blockage under footing is shown in figure 1.

Table 1. Properties of Elements Used for FEM Modelling

Parameter	Unit	Value		
		Soil	Stone	Strip Footing
Model		Mohr-Coulomb	Mohr-Coulomb	-
Unsaturated Unit Weight	(kN/m ³)	17	19	-
Saturated Unit Weight	(kN/m ³)	18.5	21	-
Young's Modulus	(kN/m ²)	8500	45000	-
Poisson's Ratio		0.15	0.1	-
Cohesion	(kN/m ²)	1	1	-
Friction Angle	°	30	40	-
Dilation Angle	°	30	10	-
Material type		-	-	Elastic and Isotropic
d	m	-	-	0.8
Unit Weight	(kN/m ³)	-	-	20
Young's Modulus	(kN/m ²)	-	-	32x10 ⁶

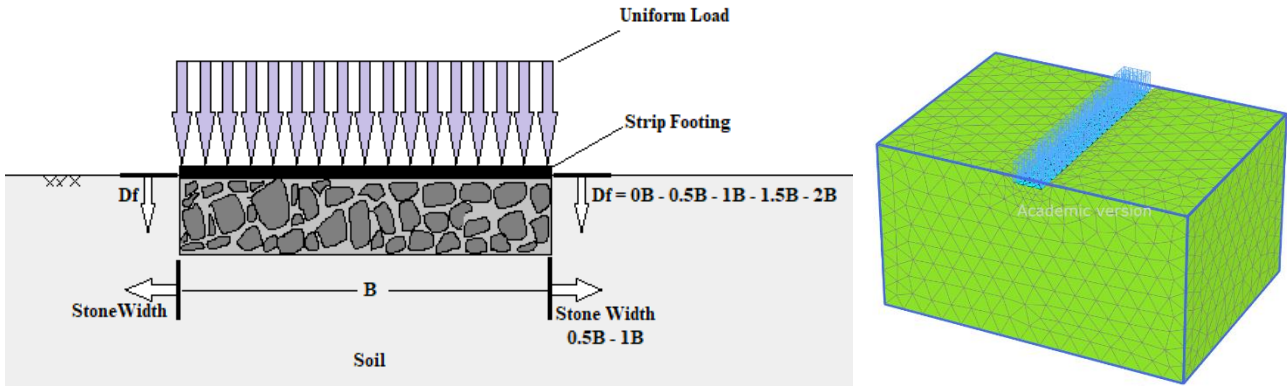


Figure 1. Schematic Shape of Foundation and Stone Blockage Modelling

In the material properties definition, the value of R_{inter} at the interface is 0.95 for sand and 1 for stone. As the simulations were done at drained conditions, the head of water for soil layers was at the bottom of the total soil layers. Therefore, as there was no water level in the simulation, the effect of an increase or decrease in water level was not taken into consideration. The mesh generated for simulation is a medium-sized mesh that is finer under footing. Plaxis 3D applied boundary conditions automatically and as there were no special conditions, the default boundary conditions did not change. In Plaxis modeling, the width of the stone layer was increased by $0.5B$ from each side of the footing to obtain a $2B$ width, and at the next step, $0.5B$ was added to the width once again to estimate a $3B$ stone layer width. The depth of the stone layer increased by $0.5B$ at each step, and four different depths of $0.5B$, $1B$, $1.5B$ and $2B$ of stone depth were simulated. At the simulation's staged construction step, the calculation type was "K0 procedure." Three phases were performed for the analysis, such as defining the soil and stone layer volumes, placing the plate as a foundation, and finally applying the 100 kN/m^2 uniform load. For soil properties, the value of Young's Modulus was entered as 8500 kN/m^2 , cohesion of 1 kN/m^2 and friction angle of 30° , which defines a weak, loose sandy soil.

3. Results and Discussion

The strip footing under a load of 100 kN/m^2 was modeled and simulated, and results containing maximum displacements and shear failure surfaces were obtained from the models. Figure 2 shows the total displacement of soil under the load of a footing. As seen in this figure, punching shear failure surfaces happened in normal soil without any stone layer. That is because of the loose structure of soil.

In continuation, stone layers were placed under strip footing at different depths and widths. Figure 3 shows the

displacement of soil and stone layer with $1B$ width at different depths. Because of the plane strain condition in simulation and to better view the shear failure mechanism of soil, all figures were shown perpendicular to the third dimension in 2D format.

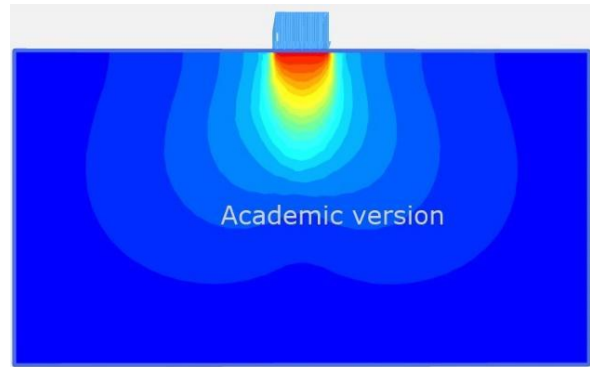


Figure 2. Total Displacement of Soil Mass without any Blockage

As seen in figure 3, by increasing the depth of the stone layer, the total affected depth of soil did not change significantly, but the punching areas were moved down and, due of the stronger materials used in the stone layer, the shear failure surfaces on two sides of this strong layer were more considerable than those inside it.

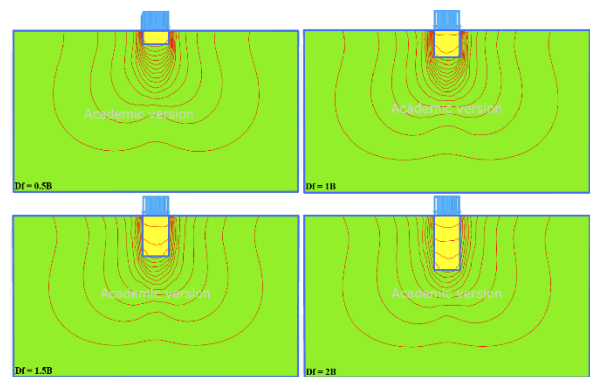


Figure 3. Shear Failure Surfaces of Soil and Stone Layers with B Width and Different Depths

But generally, the failure surface was punching at different depths. Continuing by increasing the width of the stone layer to 2B (1B under footing and 0.5B from each side of footing), different conditions were simulated and the results are shown in figure 4.

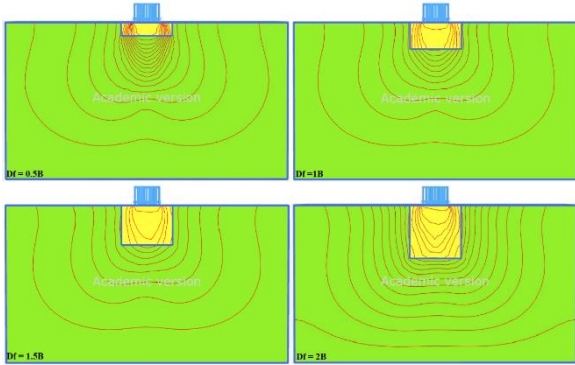


Figure 4. Shear Failure Surfaces of Soil and Stone Layers with 2B Width and Different Depths

In the stone layer modelling with 2B width and 0.5B depth, the failure surface was punching too, and even main stresses were seen in the stone mass. But by increasing the depth of stone, local shear failure surfaces started to form, and the load was distributed over a wider area under the footing. But the most critical area was still under the footing, and placing the stronger stony layer under the footing helped the total soil mass carry the applied load.

Finally, the width of the stone layer under footing increased to 3B (1B under footing and 1B from each side of footing) and 4 different conditions with the same loading and strip properties were simulated in Plaxis 3D and the results are shown in figure 5. In the condition of 0.5B depth, like all other conditions of stone mass width, the failure surfaces were punching. But as the depth of stone increased, the type of failure surface moved toward the local failure surface. In a stone mass with 3B width and 2B depth, the main load is carried by a stone layer that can lead to the increasing of the bearing capacity and fewer settlements. Settlements of footing in different conditions of stone layer width and depth were shown in figures 6 and 7. Figure 6 shows the settlement via stone layer depth and Figure 7 shows the settlement changed by stone layer widths.

The amount of settlement before placing any stone layer under the footing was 49 mm. As it is seen in previous studies, this settlement can be in an acceptable range, but as the main object of this paper is studying the effect of stone blockage, the effect of soil improvement was investigated by placing stone under the footing. As seen in figures 6 and 7, the settlement is reduced by increasing the width and depth of the stone layer. A rigid strip footing was simulated in this paper, so settlements in the corner and middle of the footing were equal.

As it can be deduced from the results, the settlement decreased from 49mm to 40mm by using a stone layer with a 1B width and 0.5B depth. The amount of settlement was 34, 29 and 25 mm while the depth of the stone layer increased to 1B, 1.5, and 2B respectively.

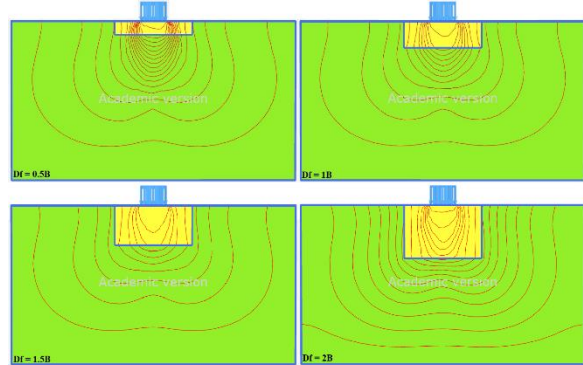


Figure 5. Shear Failure Surfaces of Soil and Stone Layers with 3B Width and Different Depths

By increasing the width of this stronger layer, settlement reached 36mm at 0.5B depth. It decreased to 25, 21, and 17mm while the stone blockage depth was 1B, 1.5B, and 2B respectively.

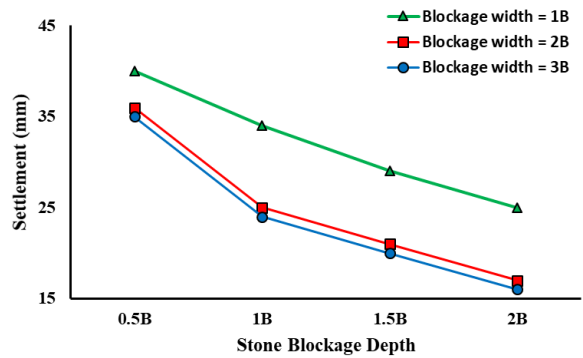


Figure 6. Settlement of footing changed with Stone Blockage Depth

Increasing the blockage width to 3B led to a decrease in settlement of the footing, but the differences were not so considerable. The amount of settlement in 3B blockage width was 35, 24, 20, and 16mm in depths of 0.5B, 1B, 1.5B, and 2B respectively.

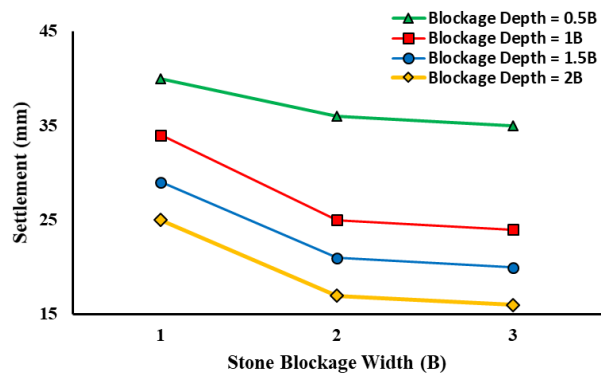


Figure 7. Settlement of footing changed with Stone Blockage Width

Figure 7 shows the change of footing settlement by stone layer width at different stone layer depths. As seen in this figure, the difference between 0.5B and 1B depth and 1B and 2B blockage width was more considerable than in other conditions, and after the width of 2B, the amount of settlement did not change significantly. The settlements of footing in different conditions are presented in Table 2.

Table 2. Settlement of Footing at Different Conditions

Depth	Settlement (mm)			
	Stone Blockage Width			
	0B	1B	2B	3B
0.5B	49	40	36	35
1B	49	34	25	24
1.5B	49	29	21	20
2B	49	25	17	16

4. Conclusions

By reviewing the results of shear failure surfaces and settlements, it was found that placing a stone layer under strip footing will reduce the settlement of the foundation and change the shear failure surface of soil. Generally, increasing the width and depth of the stone layer in all conditions reduced the settlement, but there were not so many differences in the settlement of footing in 2B and 3B widths. Additionally, settlement between 2B and 3B width of the stone layer was not so considerable. Therefore the optimum width and depth that can be selected for the simulated stone layer can be decided as 2B width (1B + 0.5B from each side of the footing) and 1B depth. In applications with similar conditions these dimensions can be selected as the optimum dimensions for the stone layer under strip footings.

This manuscript helps better understand the behaviour of improved soil layers under strip footings. The results can be used for choosing the optimum depth and width of stone blockage under footings under the conditions presented in this paper.

Declaration of Ethical Standards

The author of this article declares that the materials and methods used in this study do not require ethical committee permission or legal-special permission.

Conflict of Interest

The author declares that they have no known competing financial interests or personal relationships that could have appeared to influence the work reported in this paper.

Acknowledgements

The author thanks so much to Erzurum Technical University for providing Plaxis 3D software for using and simulating the model.

References

- [1] Bergado D. T., Anderson L. R., Miura N., 1994. Balasubramaniam AS., ASCE press, **4**, 427.
- [2] Lo S. R., Zhang r., Mak j., 2010. Geosyntheticencased stone columns in soft clay: A numerical study. *Geotextiles Geomembranes*, **28**, pp. 292-302.
- [3] Al-Kaisi, A. A. R., Ali H. H., 2013. Mathematical estimation for the bearing capacity of sand column inserted in soft clay soil. *Eng. Technol. J.*, **31**, pp. 816-827.
- [4] Al-Saoudi N. K. S., Al-Kaissi M. M., Rajab N. A. A., 2014. Treatment of soft soil by sand columns. *Eng. Technol. J.*, **32**, pp. 2106-2118.
- [5] Sánchez-Garrido A. J., Navarro I. J., Yepes V., 2022. Evaluating the sustainability of soil improvement techniques in foundation substructures. *Journal of Cleaner Production*, **1**(351), pp.131463.
- [6] Bagriacik B., 2021. Utilization of alkali-activated construction demolition waste for sandy soil improvement with large-scale laboratory experiments. *Construction and Building Materials*, **4**(302), pp.124-173.
- [7] Naghizadeh A., Ekolu S. O., 2022. Activator - related effects of sodium hydroxide storage solution in standard testing of fly ash geopolymer mortars for alkali – silica reaction. *Materials and Structures*, **55**(22), pp. 1-16. <https://doi.org/10.1617/s11527-021-01875-8>
- [8] Naghizadeh A., Ekolu S. O., 2021. Effects of compositional and physico – chemical mix design parameters on properties of fly ash geopolymer mortars. *Journal of Silicon*, **13**(12), pp. 4669-4680. <https://doi.org/10.1007/s12633-020-00799-2>
- [9] Zornberg J. G., 2002. Peak versus residual shear strength in geosynthetic-reinforced soil design. *Geosynthetics International*, **9**(4), pp. 301-318. <https://doi.org/10.1680/gein.9.0220>
- [10] Murray J. J., Frost J. D., Wang Y., 2000. Behavior of a sandy silt reinforced with discontinuous recycled fiber inclusions, *Recycled and Secondary Materials. Soil Remediation, and in Situ Testing*, **1714**, pp. 9-17, *Transportation Research Record*.

- [11] Consoli N. C., Montardo J. P., Prietto P. D. M., Pasa G. S., 2002. Engineering behavior of a sand reinforced with plastic waste. *J. of Geotech. and Geoenviron. Engrg., ASCE*, **128**(6), pp. 462-472.
- [12] Yu Y., Damians I. P., Bathurst R. J., 2015. Influence of choice of FLAC and PLAXIS interface models on reinforced soil–structure interactions. *Computers and Geotechnics*, **1**(65), pp.164-174.
- [13] Wulandari P. S., Tjandra D., 2015. Analysis of geotextile reinforced road embankment using PLAXIS 2D. *Procedia Engineering*, **1**(125), pp. 358-362.
- [14] Srivastava S., Sinha A., Kumar R., 2022. Simulating the assembly size on seismic response of building clusters using PLAXIS. *Materials Today: Proceedings*.
- [15] Gray D. H., Ohashi H., 1983. Mechanics of fiber-reinforcement in sand. *J of Geotech Engrg., ASCE*, **109**(3), pp.335-353.
- [16] Al-Refeai T. O., 1991. Behavior of antigranulocytes soils reinforced with discrete randomly oriented inclusions. *Geotextiles and Geomembranes*, **10**(4), pp. 319-333.
- [17] Yoo C., 2015. Settlement Behaviour of Embankment on Geosynthetic-Encased Stone Column Installed Soft Ground - A Numerical Investigation. *Geotextiles and Geomembranes*, **43**, pp. 484-492. DOI: 10.1016/j.geotexmem.2015.07.014
- [18] Kaliakin V., Khabbazian M., Meehan C., 2012. Modelling the Behaviour of Geosynthetic Encased Columns: Influence of Granular Soil Constitutive Model. *International Journal of Geomechanics*, **12**(4), pp. 357–369. DOI: 10.1061/(ASCE)GM.1943-5622.0000084
- [19] Ambily A., Gandhi S., 2007. Behaviour of Stone Columns Based on Experimental and FEM Analysis. *Journal of Geotechnical and Geo-Environmental Engineering*, **133**(4), pp. 405-415. DOI: 0.1061/(ASCE)1090-0241(2007)133:4(405).



The Benefits of Uncertainty and Risk Assessment Studies on the M5 Metro Line (Istanbul - Turkey)

Mehmet OZCELIK ^{1,*} 

¹ Department of Geological Engineering, Süleyman Demirel University, Isparta, Turkey, **ORCID:** 0000-0003-4511-1946

Article Info

Research paper

Received : December 30, 2021

Accepted : August 16, 2022

Keywords

Uncertainty
Underground Construction
Risk Assessment
Tunnel

Abstract

Uncertainty is often the most significant source of risk associated with a project in tunnel and underground construction. Unforeseen uncertainties can lead to significant construction problems leading to reduced tunnel advances and delays, cost increases, damage to existing infrastructure and/or damage to building equipment. The M5 metro line, which is the subject of the study, is located in Uskudar – Umraniye - Cekmekoy - Sancaktepe district on the Asian side of Istanbul. The line is approximately 17.5 km long and has 16 cut and cover stations. M5 metro line was used the four earth pressure balance (EPB) tunnel boring machines. The effect of uncertainty on risk assessment and decision-making is increasingly given priority, particularly for large infrastructure projects such as tunnels where uncertainty is often the primary source of risk. This article is intended to explain the tangible benefits of underground uncertainty and risk assessment of the M5 metro construction for underground project stakeholders, local authorities, designers, practitioners and researchers.

1. Introduction

Tunnels and underground construction are in high demand in many engineering projects around the world [1]. The construction of tunnels has provided a powerful boost to rapid economic growth over the last 10 years. However, due to a variety of risk factors related to complex project environments, breaches of safety law often occur in tunnel construction, leading to serious problems with related project activities [2-4]. Tunnels and underground construction are always present with uncertainties and risks [5-6]. Decisions will be affected at every step of the project, from design, planning to execution, uncertainties, particularly geotechnical ones. The effect of uncertainty is known as risk to the target. These risks may have an impact on the functioning, productivity of construction and the environment [7]. It is essential for successful risk management to have competence with a thorough understanding of the risk situation [8]. Reducing the risk will be at the center of the risk management process. Various approaches can be implemented depending on the

problem. Significant problems emerge from complexities in tunnel engineering and the need to integrate them into research, design and practice. Different types of uncertainties can affect a specific site's engineering efficiency, geological analysis, site characterization, geotechnical data provision, safe and efficient construction. Fluctuations in construction time and cost estimates arise from natural variation in construction results, as well as the occurrence of special events such as tunnel collapse [9].

Numerous methods of risk analysis are available, such as fault tree analysis, event tree analysis, consequence or cause-consequence analysis, probabilistic risk analysis, decision analysis, multi-risk analysis, preliminary hazard analysis, Bayesian Networks, hazard and operability analysis, bow-tie analysis and fault mode analysis [10-15]. Sousa and Einstein [16] describe the Bayesian Network model, which estimates the expected utility as the sum of the expected costs and the risk of a tunnel collapse. Probabilistic risk analysis by Spackova et al. [17] of tunnel construction time and statistical data processing technique for determining inputs.

* Corresponding Author: ozcelikmehmet@sdu.edu.tr



The metro line M5, located on the Asian side of Istanbul, is a 17.5 km (double tube) with 26.985 km EPB-TBM tunnel, 18.666 km of the New Austrian Tunneling System (NATM) tunnel and 16 stations. It has several other features as well as being a fully tunneled station. The geological setting of the M5 metro line is highly complex, consisting of limestone, sandstone, siltstone, mudstone, claystone, andesite and quartzite. Geological units are often cut by dykes of the andesite, which have significantly fractured contact zones. These zones are potentially dangerous areas at more than 20 sites that are likely to face collapse. The project area is very densely populated and the overloading of tunnel lines between 10-80 m and historic buildings is one of the most significant risks to be faced during tunnel operations. It is expected that in some areas there are likely to be some ancient water wells, which may cause some serious settlement problems [16]. The complex geometry and geology of the station dictated the utmost care for the NATM sections' excavation and final liner design to ensure stability during excavation and adequate structural capacity in case of a seismic event [19]. M5 metro construction started in 2012 and was completed in 2017. This paper outlines the tangible benefits of the underground uncertainty and risk assessment of the M5 metro construction for key underground project stakeholders, local authorities, designers, practitioners, and researchers.

1. Material and Methods

Due to the complexity and variability of the surrounding medium in tunnel and underground construction, it is difficult to predict some underground responses to excavation processes. Uncertainty refers to a scenario in which there is insufficient and/or unknown knowledge to accurately depict the current state, future consequences, or multiple possible outcomes [18]. Uncertainty and risk analysis are becoming more and more common in the fields of science and engineering, including design, project management, and finance and insurance [21-22]. In order to determine the geological and geotechnical uncertainties in the M5 metro line, which is the subject of the study, drilling studies and field tests were carried out at suitable locations along the route. Then, laboratory experiments were carried out on the samples obtained from the drillings. The tunneling activity was started and completed with the evaluation of route research together with field and laboratory experiments. M5 metro transports 1.5 million people in a day and travels in 27 minutes between Uskudar and Sancaktepe (Figure 1). It has significantly reduced traffic on the Asian side, and passengers save 33 minutes per journey. The reduction in traffic has resulted in a reduction in CO₂ emissions to the atmosphere about 77 thousand 246 metric tons per year [23].

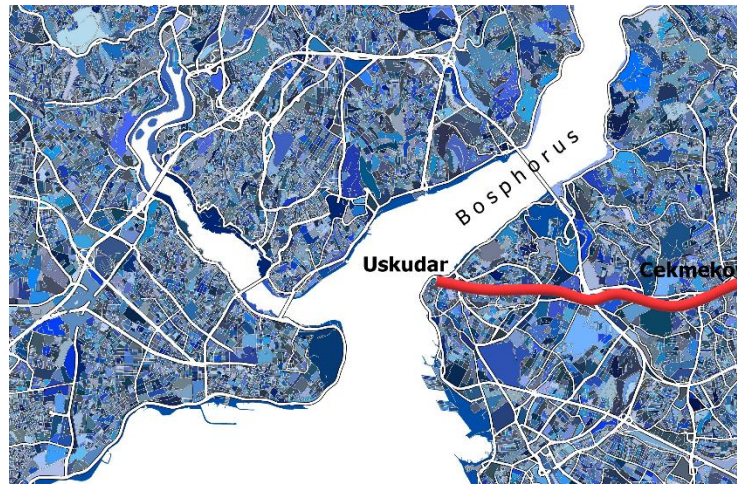


Figure 1. M5 tunnel route map [24]

2. Uncertainty Assessment

Uncertainty is an inevitable part of rock engineering. Natural variation in rock mass properties, inadequate data, measurement errors, sampling bias, load uncertainty, model simplifications and assumptions are the sources of uncertainty [15; 25-27]. Management of uncertainty is a critical problem for any underground project, and a certain degree of flexibility and responsiveness must be included in

the design process to avoid the expensive effects of unexpected circumstances [28].

2.1. Uncertainties and Risks Related to Tunnel Engineering

Tunnel design and construction in dense urban environments present unique risks and challenges. The parameters that make up the risks are still unknown, some

are intrinsic, and some emerge from the lack of knowledge of certain parameters.

2.1.1. Geological Uncertainties

Tunneling and underground construction are associated with inherent dangers due to a lack of awareness of the site's geological features and other unknowns [29]. Geological uncertainties not only affect the design of underground structures, but also have an impact on the construction process. Due to a lack of awareness of the site's geological features and other unknowns, tunneling and underground construction are connected with inherent dangers. It is unavoidable that the geological conditions will not be fully understood before the tunnel is excavated, and even then, errors in estimating geological behavior can occur [30]. Tunnel and underground excavations can be

complicated by poor geological conditions. Some possible ambiguities exist in the geological features of Istanbul's Asian side. The Paleozoic continuous sedimentary succession in the Istanbul area is well-developed, unmetamorphosed, and poorly deformed. During the excavation, the Trakya, Tuzla, Kurtköy, Gözdağ, Dalayoba, and Sultanbeyli Formations were identified. The Gözdağ Formation, which is found at the top of the Kurtköy Formation, is made up primarily of high-strength claystone-shale layers and quartzite rocks that are rich in feldspar and abrasive. Trakya Formation consists of claystone, sandstone and limestone. Thin laminated mudstones found at Tuzla Formation. The geological structure of the Kurtköy Formation is important for tunnel excavation. Quartzite is the main unit of the Kurtköy Formation and generally consists of sandstone and mudstone (Figure 2).



Figure 2. Tunnel face in Kurtköy Formation in M5 metro line Umraniye station

2.1.2. Geotechnical Uncertainties

Geology is the primary source of uncertainty in geotechnical engineering. Unidentified ground features can cause unexpected behavior, whereas identified ground variables may not be quantifiable or have unknown behavior [28]. The more geotechnical data is collected and examined, the more likely profile correlation and modification will

occur, resulting in cost savings. It is necessary to install a support system in tunnels to ensure geotechnical stability in top and bench excavation (Figure 3 a, b). Planning decisions may be incorrect if reliable geological information is not available [31]. Disruptions, weathering, and tectonic contacts in geological formation transition zones are examples of geotechnical uncertainties.

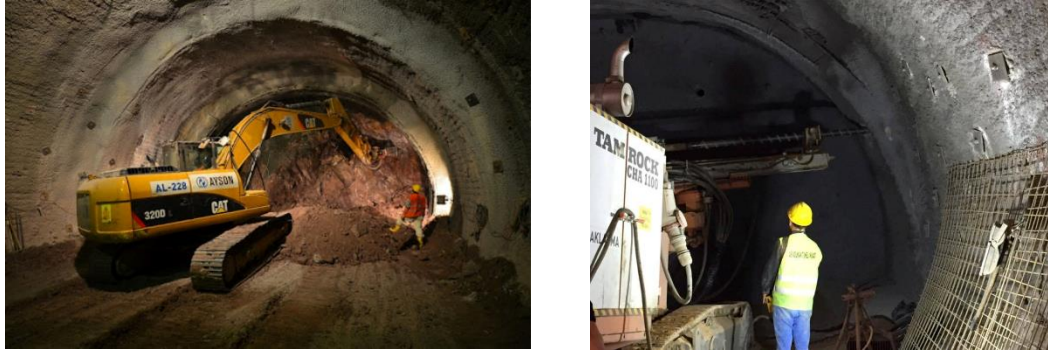


Figure 3. Top and bench excavation (a) and installation of the support system (b)

Furthermore, unexpected uncertain conditions can be used to illustrate the location of dykes, fault zones, local weathering zones, and groundwater levels. The details of the above conditions, and their position projections, are often very difficult. Despite potential uncertainties, both geological and geotechnical scenarios are potentially assessed along the tunnel route. Underground structures are generally man-made objects built within a complex and heterogeneous natural environment. Therefore, it is important to define the actions of the geological

environment according to the criteria that can be used in the structural analysis and in the planning and monitoring of the construction process for the planning and design of the structures. The geotechnical parameters along the tunnel line are given in Table 1. The uncertainty analysis performed includes rock mass quality assessment based on the Q-system (Q), Rock Mass Rating (RMR) and Geological Strength Index (GSI) of rock mass classification for the M5 metro line (Table 2).

Table 1. Summary results of the geotechnical parameters [32-38]

Formation characteristics			Geotechnical Properties				
Formation	Unit	Unit weight (kN/m ³)	Cohesion c (kPa)	Strength parameters		Deformation parameters	
				Uniaxial Compressive Strength (MPa)	Internal friction angle Ø (°)	Young modulus E (GPa)	Poisson ratio ν
Trakya Formation	Claystone	28.6-28.9	18-20	67-185	30-34	4.9-5.40	0.16-0.22
	Sandstone	27.2-27.4		16.7	20-26		0.23-0.30
	Limestone	26.0-28.0		15-105	55-58		0.14-0.40
Tuzla Formation	Limestone	26.3-28.4	7.5	40-165	40-56	1.90-4.58	0.23-0.39
	Claystone-Shale	25.5-27.0		15-65	30-35		0.28-0.26
Kurtköy Formation	Claystone	23.4-27.6	7.5	12-17	20-55	1.90-4.58	0.20-0.24
	Quartzite	26.5-26.9		48.2-49.3	45-50		0.37
Gözdağ Formation	Claystone	22.0-27.0	7.5	9-21	41-48	1.90-4.58	0.23-0.47
	Claystone-Mudstone	25.7-26.0		7-8			
	Sandstone	26.8-27.2		26-28			
Dalayoba Formation	Andesite	26.2-26.8	7.5	7-38.3	53-54	1.90-4.58	0.27-0.40
	Limestone	26.4-27.5		18.1-52.5	56-57		0.43
Sultanbeyli Formation	Claystone-Shale	22-24	7.5	20-60	15-20	1.90-4.58	0.12-0.28
	Claystone	26.0-27.7		18-28			

Table 2. Summary results of the rock mass classification in the study area

Lithology	Q- system (Q)	Rock Mass Rating (RMR)	Geological Strength Index (GSI)
Limestone	0.08-0.09	24-30	28-39
Claystone-Sandstone	0.06-0.08	26-31	30-35
Claystone-Shale	1.20-1.65	45-58	35-45
Quartzite	2.20-3.50	60-62	40-60
Andesite	10.5-11.5	65-69	50-65

2.1.3. Hydrogeological uncertainties

In terms of M5 subway tunnel excavation works, basic hydrogeological issues that should be considered as potential sources of uncertainty or risk are important. In EPB-TBM and NATM methods, attention was paid to the hydrogeological properties of rock units, in particular their permeability. During the excavation, the characteristics of

the groundwater (chemical composition, temperature, etc.) were checked and their impact on the quality of the concrete was investigated. Consideration was provided to the hydraulic load at the construction depth because the station at Umraniye, where the excavation had started, was below sea level. The pace at which the water inlet was entering the excavation works was always under control (Figure 4).



Figure 4. Water in tunnel

2.1.4. Uncertainties Surrounding Fundamental Structures

Rock masses are often and rarely cut by andesite and diabase dykes. M5 metro tunnels have often recorded collapses during construction and low progression rates in complex geological conditions characterized by faults, dykes connected to dissolved and fractured zones [39]. Furthermore, a dense cataclysm zone in contact with the main rock was found locally. Magmatic intrusions take place every 50-70 meters during tunnel construction. İBB [39] mapped a total of 39 dykes in the Istanbul settlement area. The thickness of these dykes ranges from a few decimeters to a few meters.

Weathering and fracturing effects: The fractured rock mass is weathered by active tectonic movements. Because they are formed from the fractured rock mass process, the weak zones and the fault zones provide an intensifying weathering environment. As a result, the weathering effect may be below the surface more than a hundred meters. Tunneling in such a setting must be dealt with carefully in the preparation and implementation phases in relation to the evaluation of rock mass consistency. At some underground depths, the formation of weathered rock is undisclosed and irregular. In transition zones, the weathered rock can pass

from a rock zone to a good rock mass, then return to a weathered rock mass. Nevertheless, due to changes in continental mineralogy or weathering, in weathered or calcified rock, "undifferentiated blocks" of varying sizes can be used as "floating blocks." It should be noted that karstic cavities may exist in the limestone zones. The (dissociated or undifferentiated) ground cover, as well as the calcareous rock masses, may provide essential conditions for these morphologies.

High abrasive rock effect: The presence of abrasive rock environments at the M5 metro was reported based on field and laboratory test results. Those are the quartzite, andesite, and diabase dyke lithology.

Squeezing of the soil and its effects: Due to the formation of Sultanbeyli clay there was no evidence of severe swelling problems. Nevertheless, it is critical that the risk of local swelling in the Sultanbeyli Formation is not ignored.

Adhesion: The formation of clay lithology of the Sultanbeyli Formation has such a potential according to laboratory test results.

Karst structures: This is particularly important for the Trakya Formation limestone lithology in the project region. Water may fill the voids, even without water. Important conditions can occur in both calcareous rock masses and in

their interactions with weathered or unweathered rock masses for these morphologies.

Collapse risk: Collapses in tunnel linings may occur because of lateral pressure in areas where low-strength rocks are present. It is accompanied by the presence of dykes in the project's most vulnerable locations, as well as the threat of huge fragmented rock in small areas. As a percentage of the size of the shattered rocks created, such scenarios can also cause the crushed rock to reach the surface of near-surface tunnels, posing a threat to tunnel excavators and personnel.

Block stability: The rock conditions encountered during the excavation are properties that may block instability depending on the degree of discontinuity and tunnel geometry. Discontinuity and geometry of the intersection may cause such instability to occur as a slip or fall.

2.1.5. Risk of Earthquake Events

The world's most earthquake-prone countries include China, Indonesia, Iran, and Turkey. There is a high chance that a tunnel will be damaged if it undergoes intense shaking, is located near an earthquake fault, or has problematic geological or building conditions. M5 metro tunnel line is located approximately 20 km from the North Anatolian Fault Zone, in a seismically active area (Figure 5). Two flexible seismic joints / segments for extraction / reduction with a shear displacement limit of 50 mm and a shear limit of 75 mm have been invented, specially designed, and installed in marine sediments near both ends of the section to reduce the seismic stress / stress below the permissible level. The tunnel's behavior during an earthquake was built for Mw = 7.25, and it was tested for operation and safety using earthquakes with return periods of 500 and 2500 years [40].

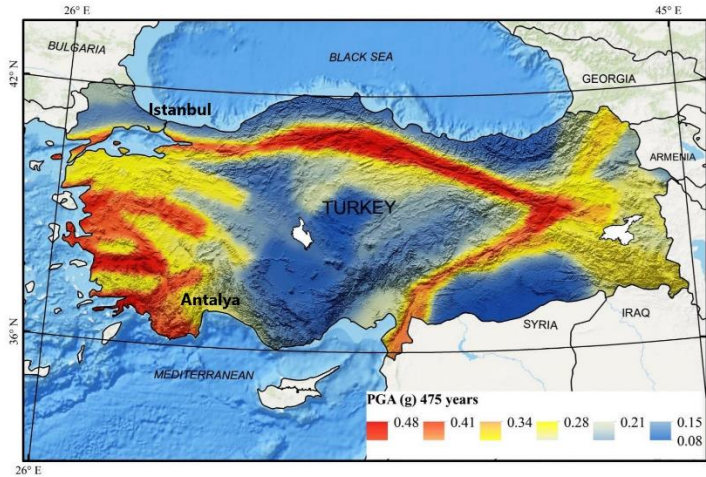


Figure 5. Probabilistic seismic hazard map from the National Seismic Hazard Model [41]

3. Evaluation of Risk Factors (RF)

A risk factor is defined as the effects on the outcomes or project objectives, as well as the likelihood of these outcomes occurring [42]. British Standards Institute provided a Risk Management process. According to BSI-6079-3 [43], there are two broad phases within the risk management process. The first phase concentrates on defining the scope of risks to be managed. This situation can be looked at as a problem-framing activity. The second deals with assessing and managing risk. The flowchart below depicts the step-by-step procedure for evaluating the risk factor (Figure 6).

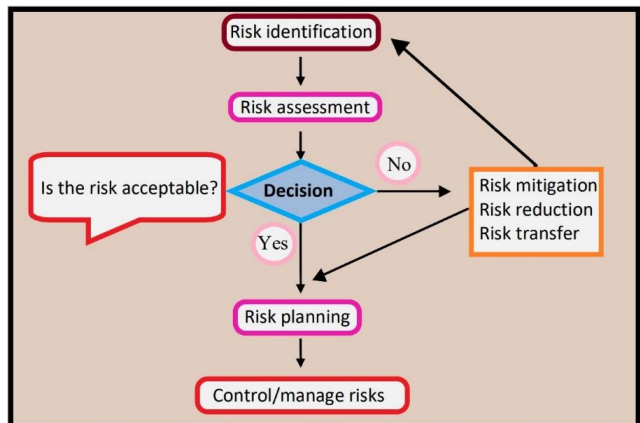


Figure 6. Risk factor evaluation methodology

The risk factor can be calculated by using the following formula [44]:

$$RF = P + C - (P * C) \dots\dots\dots (1)$$

Where; RF = Risk factor.

P = Probability (occurrences) measure on a scale of 0 to 1.
 C = Consequences (impact) measures on a scale of 0 to 1.
 If either the probability P or the consequences C are high, or both, the risk factor will be high. This formula is only valid if P and C scale ranges from 0 to 1. The simple matrix shown in Figure 7 is used to combine the likelihood and consequences ratings in order to generate initial risk priorities. The risk matrix is plotted using two-dimensional scales of impact / consequences and occurrences/probabilities ranging from 0 to 1. A risk matrix provides information about the criticality of a risk. The risk matrix categorizes risks into four categories: low, medium, high, and critical. Group Low indicates that the risk is no longer important, and it may be ignored or dealt with as a last priority. Similarly, group critical means that all risks in this group require the project manager and team's undivided attention [45]. These risks must be addressed as soon as possible. A risk profile can be created by arranging calculated risk factors in descending order. Use an 'uncertainty and risk model' to assess the various risks identified in engineering projects and identify outcome and probability ratings, risk priorities, and inherent risk levels

that will have an impact on project success if they occur [46]. Table 3 depicts the likelihood of the occurrence of various risks and their corresponding effects on the project. Table 4 displays the assessment scores, which range from 1 to 5. The numerical scores of events and impact for risk are converted from a 1 to 5 scale to a 0 to 1 scale using the formula below.

$$\text{Required score} = (\text{responded score} * 2) / 10 \quad (2)$$

Risk factor (RF) or combined risk measure is then calculated for each risk by using Eq.1.

Table 5 shows the score and calculated risk factors for the study, and similar calculations are performed for the remaining case studies. In order to resolve it, risk matrices are plotted using two-dimensional scales 0 to 1 of Impact/Consequences and Occurrences/ Probability, which are also plotted with respect to the decreasing order of calculated risk (Table 6). A risk graph (Figure 8) and risk profile (Figure 9) are plotted for Metro Line, and similar risk matrices and risk profiles are computed for the remaining case studies. Risks profile where elements are arranged in descending order of RF as shown in Figure 10.

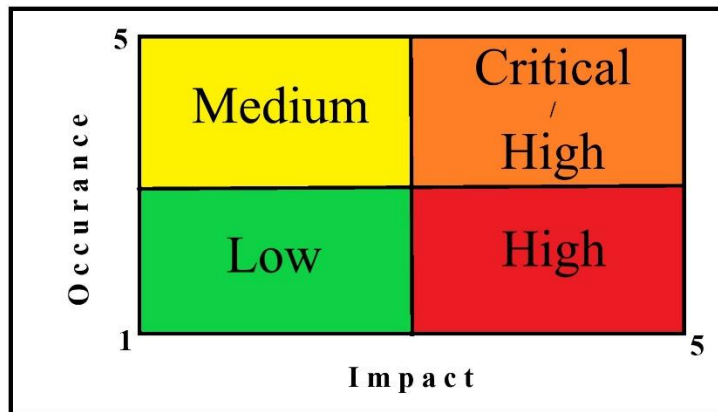


Figure 7. Risk occurrence versus impact matrix

Table 3. Probability and impact scales

Grade	Assessment of likelihood (P)	Assessment of impact
1	Rare	Minor effect
2	Considerable	Low effect
3	Medium	Medium effect
4	Frequent	High effect
5	Always	Extreme high effect

Table 4. Responses to questionnaires

Potential risk number	Risks shortlisted	Responses on scale 1 to 5	
		Occurrence	Impact
1	Geological risks	4	4
2	Geotechnical risks	3	3
3	Hydrogeological risks	3	3

Table 4. (Cont.) Responses to questionnaires

Potential risk number	Risks shortlisted	Responses on scale 1 to 5	
		Occurrence	Impact
4	Route selection risk	4	4
5	Excavation and design risks	1	1
6	Earthquake risk	2	2
7	Environmental related risks	1	2
8	Technology selection risks	2	2
9	Risks due to delay in approval of	1	2
10	detailed project report	1	3
11	Joint venture risks	1	2
12	Political and financial and risks	1	3

Table 5. Calculation of risk factors

Potential risk number	Occurrences		Impact		Risk factor
	Responded score	Scores (P)	Responded score	Scores (C)	
1	4	0.8	4	0.8	0.96
2	3	0.6	3	0.6	0.84
3	3	0.6	3	0.6	0.84
4	4	0.8	4	0.8	0.96
5	1	0.2	1	0.2	0.36
6	2	0.4	1	0.4	0.64
7	1	0.2	2	0.4	0.52
8	2	0.4	2	0.4	0.64
9	1	0.2	2	0.4	0.52
10	1	0.2	3	0.6	0.68
11	1	0.2	2	0.4	0.52
12	1	0.2	3	0.6	0.68

Table 6. Risk prioritization

1 st priority	1 st and 4 th risks
2 nd priority	2 nd and 3 rd risks
3 rd priority	10 th and 12 th risks
4 th priority	6 th and 8 th risks
5 th priority	7 th , 9 th and 11 th risks
6 th priority	5 th risk

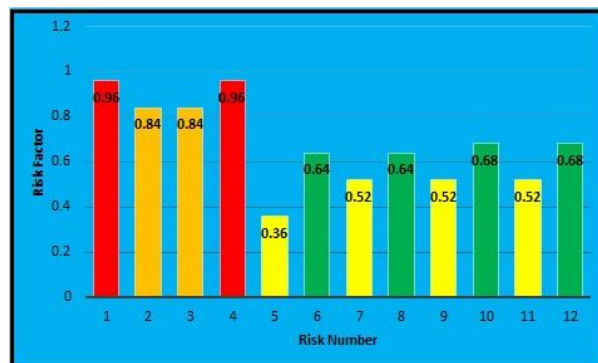


Figure 8. The risk graph for the Metro Line

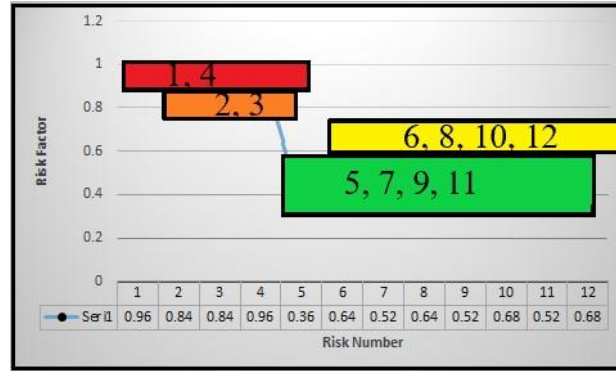


Figure 9. Profile of collective risk

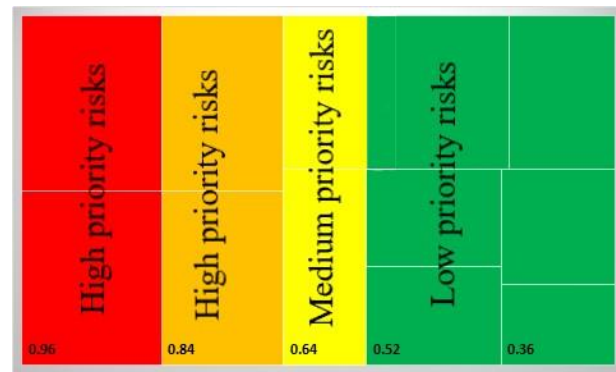


Figure 10. Risks profile with elements organized in descending order of Risk Factor

4. Results and Discussion

The quality of the rock mass through which the tunnel passes, as well as the rock support measures used during tunnel excavation, are critical to the success or failure of any tunneling operation [47]. Accurate assessment, analysis, and evaluation of rock mass quality are critical in this regard. The geological units are often cut with markedly fractured contact zones by andesite dykes. Contact zones are the possible vulnerable areas at more than 23 locations that are likely to face collapse. The most significant risks encountered during tunnel excavation include overburden changes of 10-80 m and old buildings located above tunnel lines. The NATM and EPB-TBMs are used to construct M5 Metro tunnels (Figure 11). EPB-TBMs designed the main metro line tunnels, each having a diameter of 6.57 meters, and the project's two lines. Due to the different cross-sections of these tunnels, the metro station platform tunnels, the switch tunnels and the depot area connection tunnel were constructed by NATM. At the beginning of the metro project, a depot connection tunnel with a cross-section of 74 m² was excavated with NATM. Nevertheless, additional soil boring has shown that soil conditions by the umbrella arch method require at least half the depot link tunnel section. As

a result, this single tunnel was excavated with a cross-section of 2 x 34 m² as twin EPB-TBM tunnels. Constructing the EPB-TBM depot link tunnel as twin tunnels are estimated to be more cost-effective and quicker than constructing a single-wide tunnel. At the end of building the depot connection tunnels with the TBMs, it is found that the depot link tunnels were modified from NATM to EPB-TBM.

A risk factor is defined as the effects on the outcomes or project objectives, as well as the likelihood of these outcomes occurring. Risks and uncertainties must be identified and evaluated in advance for engineering studies to be successful. More effort is required for risk assessment, particularly in metro projects. Tunnel designs are highly complex and are related to a variety of uncertainties owing to geological and geotechnical conditions, exterior loading and construction efficiency. During tunneling, these uncertainties can lead to future hazards for both the employees and the environment around them. In urban regions, surface settlements induced by tunnel excavation may be particularly important, with higher significance in blended soil circumstances.



Figure 11. EPB-TBMs in the M5 Metro Tunnel

5. Conclusions

Uncertainty is one of the most important aspects of tunnel design and underground construction. Professionals and academics are increasingly focused on how to deal with complexity in the risk management and risk control process. Uncertainty is one of the most important aspects of tunnel design and underground construction. Professionals and academics are increasingly focused on how to deal with complexity in the risk management and risk control process. This paper discussed how to cope with uncertainty and how to assess and make decisions under uncertainty. Risk and uncertainty analysis was carried out for the M5 metro project. According to geological studies, it was observed that there are different transition zones at 23 different points along the tunnel line. These are critical zones that can be collapsed in front of the tunnel face during the EPB-TBM excavation. In such cases, reducing the openings in front of the EPB-TBM cutter head can be a partial solution. EPB-TBM applications and reducing the openings prevent the reduction of the collapses in front of the tunnel face, especially when the contact zones are very fractured, especially when the RQD is low. Physical, mechanical tests and petrographic examinations were carried out on the drilling cores of critical zones. As a result of the uncertainty and risk assessment, EPB-TBMs are applied to the most appropriate procedures to be employed for opening the tunnel. The assessments carried out using the EPB-TBM system are the most relevant. The EPB-TBM can operate extremely smoothly and efficiently in these areas because the groundwater on the project route is collected as a lake in some places and the lithology of the path is composed of a wide range of rocks, ranging from relatively un-weathered to weathered rocks. Another important outcome of choosing this machine is that it has a ground pressure control mechanism to prevent collapses on the machine's flooring.

Another reason to use EPB-TBM is that large constructions must be delayed during tunnel opening, as well as the possibility of faults. As a result, it was determined that the EPB-TBM excavation would be better suited for the M5 Metro line tunnel. For the project, four EPB-TBMs with a diameter of 6.57 meters per line and two sides are being hired. As a result, in order for the metro works to be successful, risks and uncertainties must be identified and evaluated in advance. In engineering projects, more work is required for risk assessment. The geological risks and the risk of route selection have been determined to have the highest value as a result of the risk assessments. It was calculated that it should be classified as high because it has a critical value in geotechnical and hydrogeological risks. The risk and uncertainty factors encountered along the M5 Metro line were evaluated in this study.

Acknowledgment

The author would like to thank the Editor and anonymous referees for their very helpful comments and suggestions, which allowed the article to be significantly improved, as well as the Doğuş Construction Group engineers and Istanbul Metropolitan Municipality managers for their assistance.

Conflict of Interests

No conflict of interest was stated by the author.

Declaration of Ethical Standards

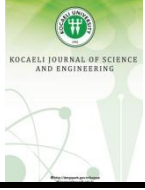
The author of this article declares that the materials and methods used in this study do not require ethical committee permission and legal-special permission.

References

- [1] Lin P., Liu H.Y., Zhou W.Y., 2015. Experimental study of failure behavior of deep tunnels under high in-situ stresses. *Tunnelling and Underground Space Technology*, **46**, pp.28-45.
- [2] Zhong M.H., Zhang X.K., Liu T.M., Wei X., Fan W.C., 2003. Safety evaluation of engineering and construction projects in China. *Journal of Loss Prevention in the Process Industries*, **16**(3), pp.201-207.
- [3] Liu T.M., Zhong M.H., Xing J.J., 2005. Industrial accidents: challenges for China's economic and social development. *Safety Science*, **43**(8), pp.503-522.
- [4] Xia Y., Xiong Z., Dong X., Lu H., 2017. Risk assessment and decision-making under uncertainty in tunnel and underground engineering. *Entropy* **19**, 549. <https://doi.org/10.3390/e19100549>
- [5] Qian Q.H., 2014. Report on the strategy and countermeasure of safety risk management system for civil engineering in China. Consulting Research Project of Chinese Academy of Engineering.
- [6] Ozcelik M., 2020. Examination of uncertainties and risk sources in Dudullu-Bostanci (Istanbul) Metro construction. *Arabian Journal of Geosciences*, **13**, 355. <https://doi.org/10.1007/s12517-020-05400-z>
- [7] Ozcelik M, Aydemir M.C., 2021. Evaluation of uncertainties in travertine rock mass for the Antalya (Turkey) Metro tunnel excavation, *Journal of Taibah University for Science*, **15**(1), pp.295-302, <https://doi.org/10.1080/16583655.2021.1978832>
- [8] Hou W, Yang Q, Chen X, Xiao F, Chen Y., 2021. Uncertainty analysis and visualization of geological subsurface and its application in metro station construction. *Frontiers in Earth Science*, **15**(3), pp.692-704. <https://doi.org/10.1007/s11707-021-0897-6>
- [9] Isaksson T., Stille H., 2005. Model for estimation of time and cost for tunnel projects based on risk evaluation. *Rock Mechanics and Rock Engineering*, **38**, pp.373-398.
- [10] Bahr, N.J., 1997. System safety engineering and risk assessment. A practical approach. Washington: Taylor & Francis. 251 p.
- [11] Benardos A.G., Kaliampakos D.C., 2004. Modelling TBM performance with artificial neural networks. *Tunnelling and Underground Space Technology*, **19**, pp.597-605.
- [12] Shahriar K., Sharifzadeh M., Hamidi J.K., 2008. Geotechnical risk assessment based approach for rock TBM selection in difficult ground conditions. *Tunnelling and Underground Space Technology*, **23**, pp.318-325.
- [13] Hong E.-S., Lee I.-M., Shin H.-S., Nam S.-W., Kong J.-S., 2009. Quantitative risk evaluation based on event tree analysis technique: Application to the design of shield TBM. *Tunnelling and Underground Space Technology*, **24**, pp.269-277.
- [14] Aliahmadi A., Sadjadi S., Jafari-Eskandari M., 2011. Design a new intelligence expert decision making using game theory and fuzzy AHP to risk management in design, construction, and operation of tunnel projects (case studies: Resalat Tunnel). *The International Journal of Advanced Manufacturing Technology*, **53**, pp.789-798.
- [15] Brown E.T., 2012. Risk assessment and management in underground rock engineering-an overview, *Journal of Rock Mechanics and Geotechnical Engineering*, **4**(3), pp.193-204. doi:10.3724/SP.J.1235.2012.00193
- [16] Sousa R.L., Einstein H.H., 2012. Risk analysis during tunnel construction using Bayesian Networks: Porto Metro case study. *Tunnelling and Underground Space Technology*, **27**, pp.86-100.
- [17] Spackova O., Sejnoha J., Straub D., 2013. Probabilistic assessment of tunnel construction performance based on data, *Journal of Tunnelling and Underground Space Technology*, **37**, pp.62-78. <https://doi.org/10.1016/j.tust.2013.02.006>
- [18] Tuysuz L., 2012. Istanbul'da açılacak metro tünellerinde TBM (tünel açma makinesi) performansını tahmin etmek için yeni bir yaklaşım. Istanbul Teknik Üniversitesi, Fen Bilimleri Enstitüsü, Yüksek Lisans Tezi, Istanbul. 101 p.
- [19] Eftekhari A., Taromi M., Saeidi M., 2014. Uncertainties and Complexities of the Geological Model in Slope Stability: A Case Study of Sabzkuh Tunnel. *International Journal of Mining and Geo-Engineering*, **48**(1), pp.69-79.
- [20] Zhang L., Wu X., Zhu H., AbouRizk S.M., 2017. Performing global uncertainty and sensitivity analysis from given data in tunnel construction. *Journal of Computing in Civil Engineering ASCE*, **31**(6), 04017065. ISSN 0887-3801
- [21] Cacuci D.G., Ionescu-Bujor M., 2004. A comparative review of sensitivity and uncertainty analysis of large-scale systems-II: Statistical methods. *Nuclear Science Engineering*, **147**(3), pp.204-217.

- [22] Pennington T.W., Richards D.P., 2011. Understanding uncertainty: Assessment and management of geotechnical risk in tunnel construction. *GeoRisk*, ASCE, **26-28**, pp.552-559. [https://doi.org/10.1061/41183\(418\)54](https://doi.org/10.1061/41183(418)54)
- [23] www.betonsa.com.tr (2020). Üsküdar-Çekmeköy Metro Project Details. <http://www.betonsa.com.tr/en/reference-projects/uskudar-cekmekey-metro/> (Accessed date 27.06.2021)
- [24] www.mapsasart.com (Accessed date 27.06.2021)
- [25] Einstein H.H., Baecher G.B., 1982. Probabilistic and statistical methods in engineering geology - problem statement and introduction to solution. *Rock Mechanics*, Suppl. **XII**, pp.47- 62.
- [26] Hadjigeorgiou J., Harrison J.P., 2011. Uncertainty and sources of error in rock engineering, in Y Zhou (ed.), *ISRM 12th International Congress on Rock Mechanics*, International Society for Rock Mechanics, Lisboa, pp.2063–2067, (accessed date 30 June 2020) <https://www.onepetro.org/conference-paper/ISRM-12CONGRESS-2011-377%5Cnpapers3://publication/uuid/59784E59-7268-4618-B43E-C0819D1CAAD7>
- [27] Contreras L.F., Ruest M., 2016. Unconventional methods to treat geotechnical uncertainty in slope design, in P. Dight (ed.), *Proceedings of the First Asia Pacific Slope Stability in Mining Conference*, Australian Centre for Geomechanics, Perth, pp.1-16.
- [28] Goodman R.E., 1993. *Engineering Geology. Rock in engineering construction*, New York, Wiley.
- [29] Maruvanchery V., Zhe S., Robert T.L.K., 2020. Early construction cost and time risk assessment and evaluation of large-scale underground cavern construction projects in Singapore. *Underground Space*, **5**(1), pp.53-70.
- [30] Zafirovski Z., Gacevski V., Lazarevska M., Ognjenovic S., 2019. Procedures for risk analysis and management in tunneling projects. *ITESE-2019, E3S Web of Conferences* 135, 01001. <https://doi.org/10.1051/e3sconf/201913501001>
- [31] Stille, H. (2017). Geological uncertainties in tunnelling - risk assessment and quality assurance. In *Sir Muir Wood Lecture 2017. The International Tunnelling and Underground Space Association*. Retrieved from <http://urn.kb.se/resolve?urn=urn:nbn:se:kth:diva-211289>
- [32] AYSON Geoteknik ve Deniz İnşaat A.Ş., 2012. Üsküdar-Ümraniye-Çekmeköy-Sancaktepe Metro Projesi, Bağlarbaşı-Altunizade-Kısıklı istasyonları zemin araştırma sondajları ve laboratuvar deneyleri geoteknik veri raporu. 104 pp.
- [33] AYSON Geoteknik ve Deniz İnşaat A.Ş., 2012. Üsküdar-Ümraniye-Çekmeköy-Sancaktepe Metro Projesi, Zemin araştırma sondajları ve laboratuvar deneyleri çarşı istasyonu geoteknik veri raporu. 48 pp.
- [34] AYSON Geoteknik ve Deniz İnşaat A.Ş., 2012. Üsküdar-Ümraniye-Çekmeköy-Sancaktepe Metro Projesi, Depo Hattı Güzergahı zemin araştırma sondajları ve laboratuvar deneyleri geoteknik veri raporu. 126 pp.
- [35] AYSON Geoteknik ve Deniz İnşaat A.Ş., 2012. Üsküdar-Ümraniye-Çekmeköy-Sancaktepe Metro Projesi, Dudullu İstasyonu zemin araştırma sondajları ve laboratuvar deneyleri geoteknik veri raporu. 71 pp.
- [36] AYSON Geoteknik ve Deniz İnşaat A.Ş., 2012. Üsküdar-Ümraniye-Çekmeköy-Sancaktepe Metro Projesi, İnkılâp- Çakmak-Ihlamurkuyu İstasyonları zemin araştırma sondajları ve laboratuvar deneyleri geoteknik veri raporu. 66 pp.
- [37] AYSON Geoteknik ve Deniz İnşaat A.Ş., 2012. Üsküdar-Ümraniye-Çekmeköy-Sancaktepe Metro Projesi, Libadiye İstasyonu zemin araştırma sondajları ve laboratuvar deneyleri geoteknik veri raporu. 47 pp.
- [38] AYSON Geoteknik ve Deniz İnşaat A.Ş., 2012. Üsküdar-Ümraniye-Çekmeköy-Sancaktepe Metro Projesi, Zemin araştırma sondajları ve laboratuvar deneyleri geoteknik veri raporu. 105 pp.
- [39] İBB (İstanbul Büyük Şehir Belediyesi Deprem Risk Yönetimi ve Kentsel İyileştirme Daire Başkanlığı Deprem ve Zemin İnceleme Müdürlüğü), 2009. *İstanbul Mikrobölgeleme Projesi Anadolu Yakası, Cilt II*, 852 S. [http://www.ibb.gov.tr/TR/SubSites/DepremSite/Documents/C_MIKROBÖLGELEME%20ANADOLU%20\(900\)_2.pdf](http://www.ibb.gov.tr/TR/SubSites/DepremSite/Documents/C_MIKROBÖLGELEME%20ANADOLU%20(900)_2.pdf)
- [40] Kulhawy F.H., Mayne, P.W., 1990. *Manual on estimating soil properties for foundation design*. Research Project 1493-6, Cornell University, New York.
- [41] Akkar S., Azak T., Çan T., Çeken U., Demircioğlu M. B., Duman T. Y., Erdik M., Ergintav S., Kadirioglu F.T., Kalafat D., Kale O., Kartal R.F., Kekovalı K., Kılıç T., Özalp S., Poyraz Altuncu S., Şeşetyan K., Tekin S., Yakut A., Yılmaz M. T., Yücemem M. S., Zülfikar Ö., 2019. Evolution of seismic hazard maps in Turkey. *Bulletin of Earthquake Engineering*, **16**, pp.3197-3228. <https://doi.org/10.1007/s10518-018-0349-1>

- [42] Taroun A., Yang J., Lowe D., 2011. Construction Risk Modelling and Assessment: Insights from a Literature Review. *The Built & Human Environment Review*, **4**(1), pp.87-97.
- [43] BSI-6079-3., 2000. Project management Part 3: Guide to the management of business related project risk. London: British Standards Institute.
- [44] <https://slideplayer.com/slide/16554512/>
- [45] Chapman C., 2006. Key points of contention in framing assumptions for risk and uncertainty management. *International Journal of Project Management*, **24**(4), pp.303-313.
- [46] Sarkar D., Dutta, G., 2011. A Framework for Project Risk Management for the Underground Corridor Construction of Metro Rail. *International Journal of Construction Project Management*, **4**(1), pp.21-38.
- [47] Stille H., Palmström A., 2008. Ground behavior and rock mass composition in underground excavations. *Tunnelling and Underground Space Technology*, **23**, pp.46-64.



Energy Efficiency Research In Fans and Experimental Investigation of the Effect of Motor Frequency

Selman ÇAĞMAN^{1,*} , Aşkın YILDIZ² , Alpaslan GÜVEN³ , Ümit ÜNVER⁴ 

¹ Department of Energy Systems Engineering, Kocaeli University, Kocaeli, 41001, Turkey, **ORCID:** 0000-0001-9214-7306

² Department of Energy Systems Engineering, Yalova University, Yalova, 77200, Turkey, **ORCID:** 0000-0002-2409-2136

³ Chamber of Mechanical Engineers Kocaeli Branch, Kocaeli, Turkey, **ORCID:** 0000-0003-1623-1682

⁴ Department of Energy Systems Engineering, Yalova University, Yalova, 77200, Turkey, **ORCID:** 0000-0002-6968-6181

Article Info

Research paper

Received : June 23, 2022

Accepted : September 20, 2022

Keywords

Energy Efficiency
Variable Speed Drive,
Fan Efficiency
Sustainability
Industrial Energy Efficiency

Abstract

Fans are widely used in the industry, and they have a potential in energy efficiency studies. The aim of this paper is to introduce the fan systems and the energy efficiency studies on fan systems. The parameters like flow rate, active power, fluid power and pressure difference were explained and used in the investigations together with the experimental data obtained in the energy audits. The effects of air temperature, velocity, and frequency parameters on fan efficiency were studied. The results showed that the temperature increment negatively affects the fan efficiency, and 1 m/s increase in the air velocity reduces the system efficiency by % 1,088. Finally, according to achievements of this paper, reducing the frequency with Variable Speed Drive means less fan power and Variable Speed Drive provides energy-savings but not energy efficiency.

1. Introduction

Today in developed countries, there is a tendency to reduce greenhouse gas emissions due to global warming and other environmental problems. For this goal, a global energy policy is determined that indicates a preference for renewable energy sources over fossil fuels such as solar, wind and so on [1, 2]. However, renewable energy systems are low efficient and expensive compared to conventional systems [3]. At this point, energy efficiency appears to be a desirable alternative as it is accepted “the cheapest renewable energy source”. In Energy Efficiency Law No: 5627 in Turkey, energy efficiency is defined as efficient use of energy, prevention of waste, reducing the burden of energy costs on the economy, and increasing efficiency to protect the environment while using energy resources [4]. Energy efficiency is extremely important also in reducing dependency on imported energy [5, 6, 7].

The energy efficiency potential of Turkey is stated as 15%, approximately 33 million Tons of Oil Equivalent (TOE), against 222 million TOE primary energy demand for 2020 in a report conducted by the General Directorate of Renewable Energy (YEGM) [8]. The breakdown of energy saving potential of Turkey is 30% in residences [9], 20% in industry, and 15% in transportation [10]. 40% of Turkey’s total industrial electricity consumption is diversified like: 22% fan, 29% pump, 7% compressor and 42% other utilities [11].

Approximately 65-70% of the electrical energy is consumed by electric motors in the industry, where 20% of this energy is consumed by the fans [11]. According to the data provided by the Ministry of Energy and Natural Resources (MENR), there are some ways to avoid this excessive energy consumption by fans. There is an energy saving potential of 2-8% through preventing losses and leakages in fans, 70% by using high-efficiency fans, and 50% in Variable Speed Drive (VSD) application [12].

The ratio of the energy efficiency potential of fan motors in the total energy efficiency potential in the

* Corresponding Author: selmancagman@gmail.com



industry is 2,60%. Although control and drivers have a very important place in high-efficiency fan systems [13], system efficiency does not simply mean a highly efficient motor. The entire system components have impact on the efficiency, such as design, sizing, ducts, and dampers etc [14]. An efficient fan system requires accurate investment, maintenance, and operation. Decision makers often consider initial investment cost but not operating or maintenance costs. They purchase the cheapest fan and the cheapest fan is generally the less efficient one. Nevertheless, the operational cost difference between these two fans systems; the cheapest and the efficient, is much higher than the initial investment cost difference throughout the fan's life span [15].

Improvements in the applications of the control systems affect energy efficiency of the fan systems positively. Wang modeled a proportional damper for a coal power plant and reduced power consumption by 15% [16]. In another study, conventional and novel damper control systems are experimentally compared. The authors claimed that they have achieved 20% reduction in the fan power [17]. The conventional method with Rule-Based Fuzzy Control Method (RBFCM) in air conditioning (AC) systems are investigated in an experimental study, and RBFCM provides 33% energy savings [18]. Sjöström et al. have developed a control strategy considering airflow set values, the differential pressure difference etc for fans operating in the mining industry. The results show a 40% reduction in energy consumption and a 15% reduction in the demand of air inflow to the mine [19].

Correcting installation and maintenance problems within a production facility can also save energy. The fan efficiency can be boosted up to 80% with a proper installation [20]. Doğan says, power consumption decreases 5% with the replacement of the inefficient fan blades with efficient ones and the payback period of this investment is 2 or 3 years [10]. A research carried out in a paint shop of automobile factory states that 5 fans were replaced with new efficient ones, and the payback time of this investment was 1,69 years [21].

When a VSD is used in a 3,72 kW fan motor, if the speed is reduced by 30%, there is a 44% energy saving with an annual cost advantage of \$ 543. They proved that as speed decreases, energy saving and cost advantage increase [22]. As a result of long-term performance analysis in Heating, Ventilation, and Air Conditioning (HVAC) systems, with the application of VSD in a public building in Italy, an annual energy saving of 38,9% was achieved [23]. Instead of adjusting the fan flow rate with throttling inlet vane, a VSD does the same effect with less energy consumption. According to this study, VSD energy saves vs vane throttling (VT) are as following; 37% VSD vs 20% VT, % 51 VSD vs 30% VT, 61% VSD vs 40% VT,

and 61% VSD vs 50% VT [24]. Another study states that energy consumption of 2.679 kWh decreases to 2.226 kWh in a power plant by using a VSD instead of throttling fans with a suction vane/flap [25]. Similarly, in an iron and steel factory, 960 TOE/year is saved by using VSD instead of flap control of 2.500 kW fan and the payback period of VSD investment is 0,5 years [10].

The energy consumptions of a forced draft fan (FDF) and a primary air fan (PAF) runned for 1 year were analyzed. The consumption without VSD was 25.645.627 kWh, and after utilization of VSD the consumption decreased to 17.412.053 kWh with a saving ratio of 32,1% [26]. Nel et al. have conducted an energy efficiency study of high-capacity power fans operating in a mine in South Africa. This study shows that if a VSD is used in fan motors, the return of investment is 9 months, and it causes a 53% reduction in greenhouse gas [27]. The VSD application to the fan coil system in the two library reading rooms has provided annual energy saving of 38,9% compared to the same system at a constant flow rate [28]. The VSD and variable pitch (VP) fan control methods were applied to air handling units with axial fans in a hospital in Seoul, South Korea. They reported that the VSD is suitable for an axial fan driven with low output per year while VP is an energy-efficient control method when high output is frequent. VSD reduces approximately 20–30% overall energy consumption of the ventilation system [29]. VSD also provides energy-saving rather than other conventional control techniques in the parallel fan system [30]. As can be seen from literature, fan usage in the industry with or without VSD is very common. Fans are widely used in AC systems, smoke evacuation fire systems, ventilation systems, the exhaust of drying and painting booths, vacuum systems, cooling towers, and combustion processes so the energy efficiency potential of fans is quite high. The flow control system with VSD is the best among all of the flow control systems (outlet damper control, inlet guide vane control eddy current control, and VSD) used in the industry. One of the most well known control methodology reducing energy consumption is VSD [31].

Fan systems have an important role in reducing the amount of energy consumed, energy cost and carbon emissions. The energy efficiency potential of the fans, the factors affecting this potential efficiency and the importance of the use of VSD are presented within this paper. Besides the effect of VSDs on efficiency, other energy efficiency possibilities in fans have also been investigated. The data obtained from a detailed energy audit completed within a factory that has actively operating 13 fans.

An energy audit targets to find saving opportunities. The data obtained from an ongoing system makes the study

more valuable. In its normal conditions, fans are measured with calibrated measurement devices. There are not enough resources and studies about energy savings by using VSDs or other techniques in fan applications. This paper specifically offers valuable information to engineers in the field.

Accordingly, the paper is structured as follows. The method and the data are described in section 2. The results of the calculations are provided in section 3. Section 4 includes the conclusions and the references.

2. Material and Method

2.1. Fan System Description

13 operating fans were examined within the scope of the study including dust extraction (6 pieces), dust transfer (2 pieces), chimney (2 pieces), cooling (1 piece), drying (1 piece), material transfer (1 piece) in various factories. The power of the measured fans varies between 15 and 326 kW. Examining different kinds of fans with varying capacities and sizes provides opportunity to evaluate and compare the effect of sizes on the characteristic performance. The relationships between flow rate and active/fluid power, differential pressure and fluid power are interpreted with the obtained measurements. In this paper, measurements were also taken into account to examine the effects of frequency, as one of the most important fan characteristic parameters of fan performance.

Since it would not be appropriate to compare the frequencies of different fans, the measurements were repeated and interpreted by operating a single fan at different frequencies. In order to examine the variable frequency situation, the analysed fan details are given in Table 1.

In this study, flow rate, pressure (inlet and outlet), temperature, engine speed and energy consumption values were measured. Air velocity, flow rate and inlet-outlet pressures were measured with a pitot tube anemometer, air inlet and outlet temperatures were measured with a thermometer, engine speed was measured with by tachometer. Furthermore, electric current, voltage, power, and power factor were measured with an energy analyzer. The measurement devices are given in Table 2.

Table 1. Fan-motor system data

Fan information		Electric motor information	
Brand	New York	Brand	Reliance Electric
Type	Plug Fan	Type	OMAN53348
Flow (m ³ /h)	84.950	Current (A)	73,9 A

Table 1. (Cont.) Fan-motor system data

Fan information		Electric motor information	
Flow (kg/s)	28,32	Voltage (V)	380 V
Power (kW)	53,76 HP	Power (kW)	50 HP
Head (Pa)	1,12 kPa	Frequency (Hz)	50
Revolution (rpm)	1.006	Revolution (rpm)	1.475

Table 2. Measurement devices and their characteristics

Pitot tube anemometer		Thermometer	
Brand and type	Fluke 922	Brand and type	Testo 830
Measuring range (m/s)	0,5/80	Measuring range (sec)	1,75
Working temperature (°C)	0-50	Working temperature (°C)	-50/500
Max humidity	%90 RH		
Energy analyzer		Tachometer	
Brand and type	Fluke 435	Brand and type	Testo 470
Measuring range (mm)	1-1000 V rms	Measuring range (RPM)	1/99999
AC current probe Brand	Fluke /I 430 Flex	Measurement method	infrared / contact
Current Probe Measurement Range	3000 A	Measuring precision	±0,2%
Test Conductors	TLS430 1000 V		

The duct dimensions vary according to the place where the fan is used. For more detailed information and evaluation, please refer to [32], [33]. Measurements were made in the process conditions of the factories. The measured values were recorded at a steady state when the values remained constant. The velocity measurements were taken from the center of the duct after a distance of 5 times the duct diameter from the fan outlet. The measurements were repeated for 2 different frequency values, 40,5 Hz and 45,4 Hz, to be able to examine the effect of frequency. A schematic diagram of the measurement procedure of audit is given in Figure 1.

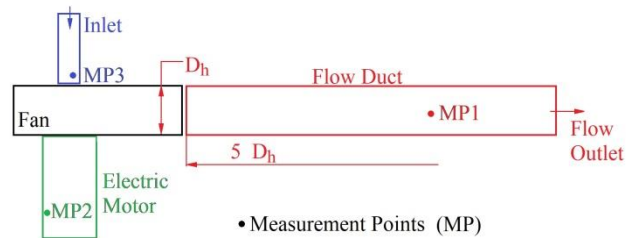


Figure 1. Schematic illustration of metering in energy efficiency audits

The temperature (T), pressure (P) and Velocity (V) parameters were measured from the duct during an energy audit measurement. If the inlet of the system was atmospheric, no measurement was taken. Atmospheric inlet conditions were used in the calculations. But if the air was sucked, then the temperature and pressure are measured. In addition, the speed of the electric motor, electric current (I) and potential (V) and power factor (PF) was measured. In energy efficiency audits, measurements are generally taken about 5 D_h from the entrance of the channels. This depends on the availability of the place of the measurement. It must be noted that, since the $Re \gg 2.300$ in the systems, the fully developed flow could be provided closer to the inlet. The measured parameters at the measurement points were shown in Table 3.

Table 3. Measured parameters at the measurement points

Measuring Point	Parameter	Unit
MP 1	T	C
	P	kPa
	V	m/s
MP 2	I	A
	V'	V
	S	Rpm
	PF	-
MP 3	P	kPa
	T	C

2.2. Fan Equations

Analyses were performed by using equations for fans known as the Fan Affinity Laws. The equations expressed as the Fan Laws are considering volumetric flow rate (Q), fan pressure P (fan total pressure P_{tf} or fan static pressure P_{sf}) and effective (shaft) power N_e . The equations are given as;

$$Q_2 = \left(\frac{n_2}{n_1}\right) \cdot Q_1 \quad (1)$$

$$P_{t_2} = P_{t_1} \left(\frac{n_2}{n_1}\right)^3 \frac{\rho_2}{\rho_1} \quad (2)$$

The Head can be calculated by;

$$H = P_o - P_i \quad (3)$$

Here, H (kPa) is the Head in pressure difference, P_o and P_i (kPa) is the air pressure at the fan outlet and inlet. The theoretical power for the required pressure (kW) is calculated by:

$$P_t = \frac{Q \cdot H}{60} \quad (4)$$

The flow rate is calculated with Equation (5) by using velocity, pressure and temperature measured in the channel.

$$Q = V \cdot A \cdot \frac{101,3 + P_o}{101,3} \cdot \frac{273}{273 + T_o} \quad (5)$$

In this equation V (m/s) is the air velocity flowing through the cross-sectional area A (m^2). T_i and T_o are the air temperature at the fan inlet and outlet in ($^{\circ}C$). Please note that Equation (5) considers the variation of fluid density with respect to temperature. The expression related to P_o and T_o in the last part of the equation is normalization with respect to 1 atm and 0 $^{\circ}C$. After measuring the electric power P (kW), the specific power consumption (kW/Nm^3) value is calculated by:

$$St = \frac{P}{Q} \quad (6)$$

Finally, the ratio of theoretical compression power to measured power that is the system efficiency is calculated by [27], [32], [34].

$$\eta = \frac{P_t}{P} \quad (7)$$

And Reynolds number can be calculated by;

$$Re = \frac{v \cdot D_h}{\nu} \quad (8)$$

Where ν is the kinematic viscosity and D_h is the hydrolic diameter. By utilizing dimensionless Re number, variation in the size of fan systems is considered because Re includes the size of the system, since the equation employs D_h as the size of the system. Similarly, the temperature variations of the fluid are also included in Re since $\nu = \mu/\rho$, where density (ρ) of the fluid depends on the temperature of the fluid. By utilizing a dimensionless number, the analyses become free of system size and operating parameters.

3. Results and Discussion

Fan power is the amount of electric power required to transport a desired air volume. The required power depends on the flow rate, the resistance of the flow area and efficiency of fan system. Energy consumption reduces at lower airflow rates. Moreover, the fan airpower is equivalent to the product of the intake volumetric airflow rate, total pressure difference across the fan and the power frequency [33], [35], [36]. Figure 2 shows the relationship

between flow rate and fluid power and active power. As seen in the figure, flow rate is directly proportional to the fluid power, and active power. As the flow rate increases, both fluid power and active power increase. Figure 2 indicates that active power and fluid power differs according to flow rate. This difference stems from the efficiency of the fan and motor. Since the sizes of each fan system are different, the difference between active power and fluid power is also variable. Fans, turbo compressors and turbo pumps are called volumetric machines. The reason why they are called volumetric is that the volume between the blades that impuls the fluid does not change. Increasing volumetric flow rate means higher fluid power and parallel to this, more active power consumption according to Equation (4).

Figure 2 also proves that Equation (4) provides the same results in practice. Trend lines added to fluid power and active power data, which have different slopes. As it can be seen in the figure, the slope of the active power line is higher. Similar to specific power consumption, both lines illustrates the required energy to impuls the unit volume of the fluid in terms of $\text{kW/m}^3/\text{s} = \text{kJ/m}^3$. In this case, the highness of the slope of the active power line can be interpreted that as more powerful system is used, the fan and motor efficiencies decrease.

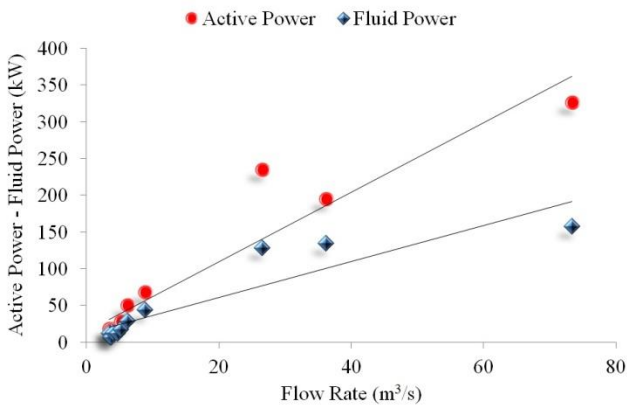


Figure 2. Relationship between Flow - Active Power - Fluid Power

Figure 3 depicts the effect of differential pressure on fluid power. In order to avoid errors because of the size and purposes of the system, identical fans are considered in the analysis. The figure shows the directly proportional relationship between differential pressure and fluid power. The differential pressure specified here is the head calculated in Equation (3). Therefore, the slope in Figure 3 stems from the power expression calculated by Equation (4). The slope of the line given in this graph provides the volumetric flow in (m^3/s) . The fluid power boosts with the increase of the differential pressure in the case of a constant volume flow. It can be evaluated in terms of energy efficiency as, as higher differential

pressure is required, the larger the fan is needed. This cause more friction losses meaning less efficient system. In this case, the most appropriate choice would be utilizing the smallest fan to provide the same flow rate with the lowest energy.

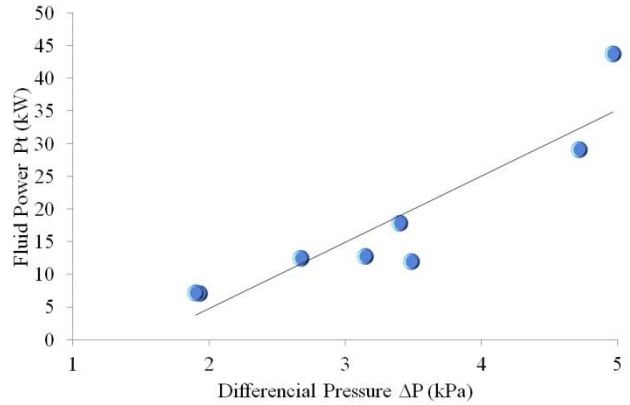


Figure 3. Relationship between Differential Pressure-Fluid Power

In Figure 4, temperature and fan efficiency relationships are provided for the examined fans. Fan efficiency tends to decrease with the increasing temperature. If the temperature of the air entering the blades increases, its density increases. If the density increases, the mass flow rate of the air within the same volume decreases. In this case, the efficiency decreases as less mass flow is directed to the outlet ducts with the same energy. Such applications are frequently encountered in chimney fans. In such cases, placing the fan at the highest point where the flue gases are the coldest is recommended to ensure the highest efficiency.

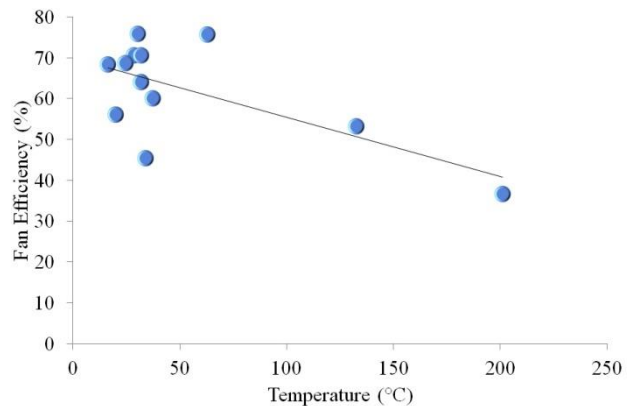


Figure 4. Temperature - Fan Efficiency relationship

The relationship between Re and the fan efficiency is provided in Figure 5. As it is seen from Figure 5, $Re \gg 2.300$, that means very high turbulence exists in the flow area. This is an obviously expected result since the flow field is in downstream of an industrial fan. The figure depicts that the system efficiency decreases as Re increases. Because, friction losses increase with the speed

and fan must compensate the increased losses. Therefore, it is recommended to transfer the air with the least possible velocity through the ducts [37].

In Figure 5, an inverse relationship is seen between Re and fan efficiency. The relationship can be represented by a $V-\eta$ coefficient that is $-1,088$ (%/m/sn). This coefficient can be considered as the effect of fluid velocity to the fan efficiency.

In duct systems, sharp elbows create turbulent areas resulting vortices that prevent the fluid flow. In other words, sharp turns such as 90° miter bends create counter pressure. Utilizing the fan system for suction may be more efficient instead of pressurizing the flow. In such cases, making the air duct larger to reduce the speed may be recommended. However, the larger the channel, the greater the initial investment cost would be. Therefore, size selection should be performed considering the initial investment and operational costs for the system's life span.

The measurements of frequency evaluation are given in Table 4. Power factor is measured 0,82 for both frequency values. It is observed that a 12% reduction in frequency (from 45,4 Hz to 40,5 Hz) results in 11,8% decrease in the speed (rpm). Frequency and speed ratios have decreased approximately at the same rate. Flow rate decreases by 4,58% from 17,72 Nm^3/s to 16,94 Nm^3/s . Power demand decreases 37,7% from 32,9 kW to 23,9 kW. A significant energy saving has been achieved in the required flow rate by reducing the fan operating speed. This example shows the difference in the energy efficiency of operating at suitable speeds in fans. Significant energy savings can be made with frequency/speed adjustment according to operating conditions instead of 50 Hz grid frequency.

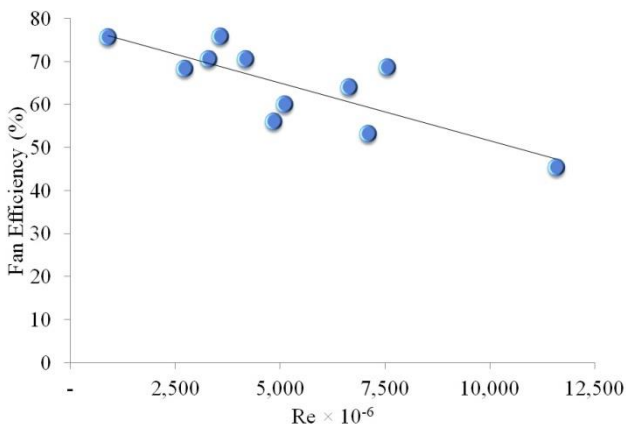


Figure 5. Air Velocity-Fan efficiency relationship

Table 4. Measurement results

Frequency	Revolution	Av. Speed	Power	Input Pressure	Output Pressure	Pressure Difference	Input Temp.	Output Temp.
F		V	P	Pin	Pout	H	Tin	Tout
Hz	rpm	m/s	kW	kPa	kPa	kPa	°C	°C
45,4	1335	10,71	32,9	-0,35	0,28	0,63	23	24,8
40,5	1197	10,18	23,9	-0,284	0,2	0,484	21,8	22,8

Table 5 shows the frequency of specific energy consumption and total efficiency values. As can be seen from Table 5, efficiencies at two frequency values are very close. However, while the specific energy consumption at 45,4 Hz is calculated as 1,86 kPa, 1,41 kPa is obtained at 40,5 Hz. With the 12% decrease in frequency, the specific energy consumption decreases by 24%. This result is proportional to reference [32] and agrees with reference [38].

Table 5. Variation of fan system efficiency depending on the frequency

	Airflow	Theoretical Power	Specific energy consumption	Total Efficiency
f	Q	P _t	P/Q	η
Hz	Nm^3/s	kW	kPa	%
45,4	17,72	12,15	1,86	36,92
40,5	16,94	8,87	1,41	37,11
*40,5	17,3	8,81	1,5	36,85

*First two lines are experimental results, and the third line is based on the theoretical calculation.

In Table 5, flow rate, power, specific energy consumption, and total efficiency values calculated theoretically according to the fan laws are given in the bottom line. The most important side of this table is the effect of frequency on fan efficiency. Reduction of the frequency reduces the consumed power since it decreases the motor revolution speed. At low speeds, the motor consumes less energy. In this case, the power conducted to the air reduces proportionally. Thus, the efficiency, which is the ratio of these two magnitudes, does not change. The resulting remark of this study is contrary to the literature that the frequency does not have any effect on the fan efficiency.

In Table 5, there are differences between the values obtained by analytical calculation. For example, while the flow rate calculated with Eq. (1) is 17,3 Nm^3/s , the measured flow rate is 16,94 Nm^3/s . The experimental value is 5,67% lower than the value calculated according to the

fan laws. The reason for this is that Equation (1) states that there is a linear proportion between revolution and flow rates. If the measured air duct were a straight and short duct, then perhaps the value calculated with the help of Equation (1) could be obtained. However, air ducts usually have sharp turns and elbows that cause counter pressure, depending on the structure of the installation. The counter-pressure decreases if the speed is decreased. Equation (1) does not include the reduction in counter pressure, it only considers the speed of rotation. As a result, the flow rate measured in the operational air duct is theoretically less than the flow calculated for a duct without losses and counter pressures. However, it is not the case for the power calculated by Equation (2). The power calculated by using the velocity measured from the air duct, theoretically represents the required power in an ideal installation without irreversibilities. That means, both are lossless-theoretical power. Therefore, they are calculated with a small difference of 0,67%.

Fans should be designed to meet the required flow rate. Unnecessarily high flow rates should be avoided because higher mass/volumetric flows require more energy. The smallest possible fan should be selected. Discharge temperatures should be chosen as low as possible. If possible, hot gases should be cooled with a heat exchanger before it enters the fan. According to the fan law, efficiency is calculated as the ratio of required power to measured power. Therefore, the calculated efficiencies are very close with a negligible difference. However, the variation of the flow rate is reflected in the specific energy consumption. The specific energy consumption calculated according to the fan laws and the experimental data are achieved 1,5, and 1,41 respectively. The difference is due to the irreversibilities such as pressure losses, friction losses, and the leaks etc. It is understood that a correction factor should be used in calculations to be made according to the fan laws in fan systems.

In the case of a variable flow system, a VSD driven high-capacity fan, can be expensive and/or inefficient. High-capacity fans can enter the unstable state easier at low flow rates. If there is a variable flow rate requirement, the use of multiple fans instead of a VSD driven high-capacity fan may be more appropriate. But this selection requires more space for multiple fans installation. Therefore, fan capacity should be calculated carefully as it affects the initial investment cost.

4. Conclusions

Energy efficiency should be treated as a new renewable energy source to reduce dependency on

imported energy. Fan systems have a huge energy efficiency, reducing the energy consumption, energy cost and carbon emissions potential in the industry. Generally decision makers prefer the cheapest fan and unfortunately the cheapest fans operate with a low efficiency. Sometimes larger fan capacities lead to a less efficient system. In this study, the energy efficiency potentials of the fans are highlighted. One of the most important parameters, utilization of VSD in fan systems, is presented by adding a case study.

There is an energy savings potential between 15% and 40% by enhancing control strategies. In fan systems, particular attention should be paid to productivity in design, assembly, operation, and maintenance with a holistic approach. In this paper, it is concluded that,

I-The air temperature and velocity have a negative effect on the fan efficiency.

II-The improvements made by frequency control do not significantly affect the efficiency.

III-However, one of the most valuable findings of this precise study is that for every 1 Hz reduction in frequency, the revolution of the fan decreases by 28, the power decreases by 1,84 kW, and the specific energy consumption decreases by 91 W (4.9%).

Finally, it should be noted that VSD systems should be used carefully since the reduction of the fan speed may cause over heating in fan motors. Additionally, the results of this study will provide a guidance to the engineers and researchers, who would consider using VSD in their fan systems.

Declaration of Ethical Standards

The authors of this article declare that the materials and methods used in this study do not require ethical committee permission and/or legal-special permission.

Conflict of Interest

The authors declare that they have no known competing financial interests or personal relationships that could have appeared to influence the work reported in this paper.

References

- [1] Kılıç G. A., Al K., Dağtekin E., and Unver U., 2020. Technical, Economic and Environmental Investigation of Grid-Independent Hybrid Energy Systems Applicability: A Case Study, Energy Sources, Part A: Recovery, Utilization, and Environmental Effects, pp. 1-16.

- [2] Selimli S. , Shtewi F. A. , Fahed A. K. A. , Yaman Koymatçık Ç. & Özkaymak P. D. M., 2021. Investigation Of Wind Energy Potential Of Four Different Sites Of Libya By Using Weibull Distribution, Konya Mühendislik Bilimleri Dergisi, **9** (3), 766-786. DOI: 10.36306/konjes.915428
- [3] Ünver Ü., Bilgin H., Güven A., 2015. Pompaj Depolamalı Hidroelektrik Sistemler, Mühendis ve Makine, **56**, pp. 57-64.
- [4] Enerji ve Tabii Kaynaklar Bakanlığı, Enerji Verimliliği Kanunu, 2007, <https://www.resmigazete.gov.tr/eskiler/2007/05/20070502-2.htm>
- [5] Demir H., Çıracı G., Kaya R., Ünver Ü., 2020. Aydınlatmada Enerji Verimliliği: Yalova Üniversitesi Mühendislik Fakültesi Durum Değerlendirmesi. Uludağ University Journal of the Faculty of Eng., **25** (3), pp.1637-1652.
- [6] Turan H.H., Ünver U., Kara O., Beşirli I., 2014. HORUS: A Decision Support Tool For Energy Efficiency Management". Energy Technologies Conference. Proceedings Book. pp. 419-428, ISBN:978-605-5120-98-6. 22-24 December 2014 İstanbul
- [7] Ünver U., Kara O., 2019. Energy Efficiency by Determining the Production Process with the Lowest Energy Consumption in a Steel Forging Facility, Journal of Cleaner Production, **215**, pp: 1362-1370. Doi: 10.1016/j.jclepro.2019.01.168
- [8] Energy Efficiency in World and in Turkey (In Turkish) Dünya’da ve Türkiye’de Enerji Verimliliği Oda Raporu, 2012. TMMOB
- [9] Ünver Ü., Adıgüzel E., Adıgüzel E., Çivi S., Roshanaei K., 2020. Application of Thermal Insulation in Buildings by Climate Zones in Turkey (In Turkish) “Türkiye’deki İklim Bölgelerine Göre Binalarda Isı Yalıtım Uygulamaları”, İleri Mühendislik Çalışmaları ve Teknolojileri Dergisi, **1**, pp. 171-187.
- [10] Doğan H., 2015. Türkiye’nin Enerji Verimliliği Potansiyeli ve Projeksiyonu, Gazi Üniversitesi Fen Bilimleri Dergisi Part:C, Tasarım Ve Teknoloji, **3**, pp. 375 – 384.
- [11] Türkiye Enerji ve Enerji Verimliliği Çalışmaları Raporu, 2010. ENVER Enerji Verimliliği Derneği, https://www.tskb.com.tr/i/content/486_1_turkiye-enerji-ve-enerji-verimliliği-calismalari-raporu-Temmuz-2010.pdf
- [12] Sanayi’de Enerji Verimli Projeler, T.C Enerji ve Tabii Kaynaklar Bakanlığı web sayfası yayınlar bölümü, Bilgi merkezi, Enerji Verimliliği,
- [13] İşler T., 2009. Dünyada ve Türkiye’de Enerji Verimliliği. Ege Bölgesi Enerji Forumu, 12-13
- [14] Aynsley R., 2002. Fan size and energy efficiency. International Journal of Ventilation, **1**, pp. 33-38
- [15] Improving fan system performance, a sourcebook for industry, 1989. AMCA (Air movement and control association int), The United States Department of Energy Air Movement and Control Association International, Inc. Washington, DC, USA
- [16] Wang Y., 2016. A power-saving control strategy for reducing the total pressure applied by the primary air fan of a coal-fired power plant, Applied Energy, **175**, pp. 380-388.
- [17] Rahnema S., 2017. Experimental study of the pressure reset control strategy for energy-efficient fan operation: Part 1: Variable air volume ventilation system with dampers, Energy and Buildings, **139**, pp. 72-77
- [18] Li X., Zhao T., Fan P., Zhang J., 2019. Rule-based fuzzy control method for static pressure reset using improved Mamdani model in VAV systems, Journal of Building Engineering, **22**, pp. 192-199
- [19] Sjöström S., Klintonäs E., Johansson P., Nyqvist J., 2020. Optimized model-based control of main mine ventilation airflows with minimized energy consumption, International Journal of Mining Science and Technology, **30**, pp. 533-539
- [20] De Souza E., 2015. Improving the energy efficiency of mine fan assemblages, Applied Thermal Engineering, **90**, pp. 1092-1097
- [21] Akbaş B., Kaya D., Eyidoğan M., 2018. Bir Otomobil Montaj Fabrikasının Enerji Tüketim Analizi ve Enerji Tasarrufu Potansiyelinin Değerlendirilmesi, Mühendis ve Makina, **59**, pp. 85-100.
- [22] Saidur R., Mekhilef S., Ali M.B., Safari A., Mohammed H.A., 2012. Applications of variable speed drive (VSD) in electrical motors energy savings, Renewable and Sustainable Energy Reviews, **16**, pp. 543-550
- [23] Schibuola L., Scarpa M., Tambani C., 2018. Variable speed drive (VSD) technology applied to HVAC systems for energy saving: an experimental investigation. 73rd Conference of the Italian Thermal Machines Engineering Association (ATI 2018), Pisa, Italy, 12–14 September 2018.

- [24] Kalpar M., 2015. Fanlarda Akış Kontrolünün Emiş Klapesi Yerine Değişken Hız Sürücüsü ile Gerçekleştirilmesinin Enerji Verimliliği Bakış Açısıyla İncelenmesi, Siemens Sanayi ve Ticaret A.Ş., EMO Yayınları, https://www.emo.org.tr/ekler/9462515dcc24e9a_ek.pdf
- [25] Kalpar M., 2017. Enerji Santrallerinde İç Tüketimi Azaltıcı Tedbirlerden Taze Hava, Sekonder Hava Ve ID Fanlarda Enerji Verimliliğinin Artırılması, Siemens Sanayi ve Ticaret A.Ş., IV. Enerji Verimliliği Kongresi, 14 Ekim 2017.
- [26] Wibowo P., M., Haddin M., Marwanto A., 2021. Energy saving analysis of air fan motor in power plant boiler controlled by variable frequency drive, *International Journal of Power Electronics and Drive Systems*; Yogyakarta **12**, pp.2059-2069. DOI:10.11591/ijpeds.v12.i4.pp2059-2069
- [27] Nel A., Arndt D., Vosloo J., Mathews M., 2019. Achieving energy efficiency with medium voltage variable speed drives for ventilation-on-demand in South African mines, *Journal of Cleaner Production*, **232**, pp. 379-390.
- [28] Schibuolaa L., Scarpaa M., Tambania C., 2018. Variable speed drive (VSD) technology applied to HVAC systems for energy saving: an experimental investigation, *Energy Procedia*, **148**, pp. 806–813
- [29] Song I. H., Lhee J., H., and Jeong J. W., 2021. Energy efficiency and economic analysis of variable frequency drive and variable pitch system: A case study of axial fan in hospital, *Journal of Building Engineering*, **43**, 103213. doi:10.1016/j.jobe.2021.103213
- [30] Prince and Hati A. S., 2021. A comprehensive review of energy-efficiency of ventilation system using Artificial Intelligence. *Renewable and Sustainable Energy Reviews*, **146**, 111153. doi:10.1016/j.rser.2021.111153
- [31] Jena M.C., Mishra S.K., Moharana H.S., 2020. Experimental investigation on power consumption of an industrial fan with different flow control methods. *Environ Prog Sustainable Energy*. 2020; 39:e13237. <https://doi.org/10.1002/ep.13237>
- [32] Mahendra Singh M., Jradi M., Shaker H. R., 2020. Monitoring and evaluation of building ventilation system fans operation using performance curves, *Energy and Built Environment* **1**, pp. 307–318
- [33] Güven A., 2016. Sirkülasyon Fanı Performans Değerlendirmesi, TMMOB Makine Mühendisleri Odası Kocaeli Şubesi
- [34] Wang Z., Han Z., Ding L. & Wang G., 2021. Development of an efficiency model for electronically commutated motor fan systems in air handling units, *Science and Technology for the Built Environment*, **27**(3), pp. 329-340
- [35] Pöyhönen S., Ahola J., Niemelä M., Hammo S., Punnonen P., 2021. Variable-speed-drive-based method for the cost optimization of air filter replacement timing, *Energy & Buildings*, **240**, 110904
- [36] De Villiers D. J., Mathews M.J., Maré P., Kleingeld M., Arndt D., 2019. Evaluating the impact of auxiliary fan practices on localised subsurface ventilation, *International Journal of Mining Science and Technology*, **29**, pp. 933–941
- [37] Canbazoglu F., 2020. Fan Mühendisliği, AIRONN Teknik Yayınları, ISBN: 978-975-6263-41-9
- [38] Teitel M., Levi A., Zhao Y., Barak M., Barlev E., Shmuel D., 2007. Energy saving in agricultural buildings through fan motor control by variable frequency drives, *Energy and Buildings*, **40**, pp. 953–960



A Low-Dimensional Feature Vector Representation for Gait-based Parkinson's Disease Detection

Emin ÖLMEZ^{1,*} , Orhan AKBULUT² , Ahmet SERTBAŞ³ 

¹ Department of Computer Engineering, Kocaeli University, Kocaeli, 41001, Turkey, **ORCID:** 0000-0002-7544-770X

² Department of Computer Engineering, Kocaeli University, Kocaeli, 41001, Turkey, **ORCID:** 0000-0003-0096-0688

³ Department of Computer Engineering, Istanbul University- Cerrahpaşa, Istanbul, 34320, Turkey, **ORCID:** 0000-0001-8166-1211

Abstract

Thanks to the developing technology, Parkinson's disease can be detected by using datasets which are obtained from different sources. Gait activity analysis is one of the methods used to detect Parkinson's disease. The gait activity of Parkinson's disease differs from the gait of a normal person. In this study, a support vector machine-based classification method using low-dimensional feature vector representation is proposed to detect Parkinson's disease. Pressure sensors placed under the foot are divided into 3 categories, placed on the heel of the foot, the center of the foot, and the toe. Average stance duration, average stride duration, and average distance are extracted from the heel of the foot and toe. The frequency value obtained from the center of the foot during the walking period is used. Only 4 feature values having $O(n)$ time complexity are used for the classification process. Experimental results point out that the proposed method can compete with similar studies proposed in the literature, even under these few features. According to the experimental results, high classification performance, up to 85%, is obtained under the whole dataset. Moreover, superior classification performance, up to 91%, is obtained when the datasets are evaluated individually.

Article Info

Research paper

Received : June 4, 2022

Accepted : October 4, 2022

Keywords

Classification

Gait Analysis

Parkinson's Disease

Support Vector Machine

1. Introduction

Diseases are defined as deteriorations or changes in the intra-corporeal or extra-corporeal [1]. In the literature, various research is carried out to understand the causes of these deteriorations or changes and to find appropriate solutions, accordingly. In this regard, high-performance approaches are proposed for the detection of different disease types.

Diseases are classified based on the systems of the body. For example, Parkinson's disease (PD), Epilepsy [2, 3], and Huntington's disease [4] originate from the body's nervous system. On the other hand, Hepatitis, Celiac, and Diabetes diseases may occur in the digestive system.

Parkinson's Disease (PD) is a nervous system disease that occurs as a result of the deterioration of the "black matter" region in the nervous system, which produces very intense amounts of dopamine [5]. In this disease, the body

is not only unable to produce dopamine at the desired level but also it can produce dopamine in a defective way. As a result of dopamine deficiency or defective dopamine, symptoms such as tremors, posture disorders, muscle stiffness, tendency to write small, loss of smell, sleep problems, movement and gait problems, voice disorders, and expressionless face occur in Parkinson's patients [6].

Symptoms of PD such as tremors, muscle stiffness, inconsistent and unbalanced gait, and posture disorder are examined by doctors [6]. However, these symptoms may not be noticed in the early stages of the disease. Therefore, the disease cannot be detected at an early stage. A delay in diagnosis of the patient negatively affects the life quality of the patient and causes a delay in the treatment.

Gait pattern, which is among the symptoms of PD, naturally causes gait differences between healthy individuals and Parkinson's patients. Considering the literature studies, advanced approaches such as neural networks, deep learning, and machine learning approaches are adopted for the detection of gait-based PD. In [7], a Q-backpropagated time delay-based neural network is

* Corresponding Author: emin.olmez@kocaeli.edu.tr



proposed to detect PD. In [8], the principal component approach (PCA) is used to reduce the number of features obtained in the gait analysis.

It is possible to extract comprehensive features by considering the additive and differential relationships between sensor data obtained from the gait patterns of Parkinson's disease and healthy individuals [9, 10].

In [11], statistical features are obtained using PD gait sensor data, then the best distinguishing features are selected among these features using Tabu and particle swarm optimization algorithms.

Parkinson's disease has different symptoms. For example, in addition to the fact that the gait pattern of the PD is different from that of healthy individuals, finger tremors appear more than in healthy individuals. In this context, in [12,13], different datasets are utilized to diagnose PD.

In [14], a support vector machine (SVM) based classification process is performed by evaluating the PD datasets separately. In the classification of Parkinson's patients, kinetic and kinematic features of gait data are used.

In [15], the pre-processing stage is applied to PD and healthy individuals. Then, the histogram is obtained by using one-dimensional local binary patterns. Statistical features are obtained by using these histograms. In the classification phase, different approaches such as Logistic Regression, Random Forest, and K-Nearest Neighbor

(KNN) are utilized to detect the PD.

In [16], a perceptron network is used for the detection of PD. In [17], 2-dimensional images were created by utilizing 1-dimensional sensor data. Then, a convolutional neural network (CNN) is applied to these images to detect Parkinson's disease. In [18], the spectrogram 2D images are generated utilizing 1D sensor data. Then, these images are fed into the neural network. In that method, the voice dataset is also used to detect Parkinson's disease. An Artificial Neural Network (ANN) based deep learning model is integrated for the voice dataset. In Table 1, a concise comparison among the related works is provided. The features, the domain information, and the contents of the methods are elaborated in Table 1.

The main contribution of the proposed method (PM) is to use a very small number of features in the detection of Parkinson's disease. By exploring only 1st order statistics of the gait sensor data, a low dimensional feature vector representation is obtained. Using these feature vectors, a simple machine learning-based classification system is proposed to classify Parkinson's patients and healthy individuals.

In Section 2, general information about the Parkinson dataset is given. The proposed method is introduced in Section 3. The experimental results are given and discussed in Section 4. Finally, the conclusion of the paper is given in Section 5.

Table 1. A concise comparison of the related works in terms of domains, features, and methods.

References	Domains	Features	Methods
[7]	Time	Raw Sensor Data	Q-backpropagated Time-Delay <u>Neural Network</u>
[8]	Time	Stance Phase and Swing Phase	PCA
[9]	Frequency	Statistical Features	Neural Network with Resilient Backpropagation Algorithm
[10]	Frequency	Statistical Features	Neural Network with Weighted Fuzzy Membership Functions
[11]	Time	Statistical Features	Best First Tree, Backpropagation Artificial Neural Network, SVM and KNN
[12]	Time-Frequency	Phases of Gait Cycle	Linear Discriminant Analysis
[13]	Time-Frequency	Phases of Gait Cycle	SVM
[14]	Time	Phases of Gait Cycle	SVM
[15]	Time	Statistical Features	KNN, Random Forest.
[16]	Time	Statistical Features	MLP
[17]	Time	Raw Sensor Data	CNN
[18]	Time	Raw Sensor Data	CNN and ANN

Table 2. PhysioNet Dataset.

Dataset	Status	Number of Participants	Average Age	Gender (Male)	Average Height (m)	Average Weight (kg)
GA	Healthy Individuals	18	72	%56	1,67	72
	PD Patients	29	71	%69	1,70	74
JU	Healthy Individuals	25	65	%48	1,69	71
	PD Patients	29	67	%55	1,66	70
SI	Healthy Individuals	29	58	%65	1,68	74
	PD Patients	35	62	%63	1,67	73
ALL	Healthy Individuals	72	66	%56	1,68	72
	PD Patients	93	64	%63	1,68	73

2. Parkinson Dataset

In this study, the PhysioNet dataset [19], which depends on pressure sensor data placed under the foot, is used. The dataset consists of three different sub-datasets, namely GA, JU, and SI [20-23]. Detailed information about the dataset is given in Table 2.

During the walking activity, 8 sensors, $S_i \in R^{n \times 1}$, are placed on the right and left soles, respectively, as shown in Figure 1. n corresponds to the length of the sensor data. Vertical ground reaction force (VGRF) data is gathered from these sensors. 100 samples are taken per second as a result of the sampling process. Necessary data is obtained from a 2-minute walking period. Walking activities are applied to Parkinson's patients and healthy individuals under the same conditions.

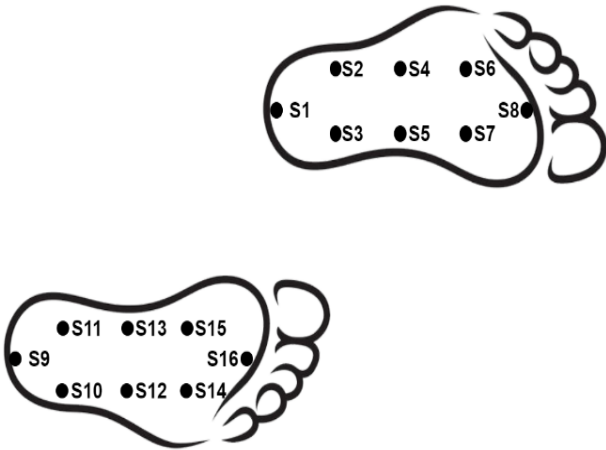


Figure 1. Locations of the sensors placed on the sole of the foot.

3. Proposed Method (PM)

In this section, some important notions about gait are provided before introducing the PM. Gait is defined as moving from one place to another as a result of the

coordinated movement of muscle and bone structures [24]. The gait consists of two phases, the stance phase and the swing phase. The stance phase begins with the heel of the foot in contact with the ground. It continues until the contact of the toe with the ground is cut off. It is sufficient to evaluate the stance phase for only one foot. The time elapsed during the stance phase is called the stance duration. The swing phase starts from the moment the toes stop contacting the ground. It ends when the heel of the foot comes into contact with the ground. It is sufficient to evaluate the swing phase for only one foot. The time elapsed during the swing phase is called the swing duration. During the gait, the stance and swing phases continue in cycles. Evaluation of both together corresponds to the stride. The stride begins as soon as the heel of the foot touches the ground. It continues until the next heel contact of the same foot. The time elapsed during the stride is called stride duration. The distance traveled in one step corresponds to the stride distance.

In this study, stride durations, stride distances, and stance durations are considered feature vectors for the detection of Parkinson's disease. PM also leverages the frequency information of the sensors to show how dominant each sensor is during gait activity. Using the introduced feature vectors, a machine learning-based classification method is proposed. The flowchart of the classification stage of the PM is shown in Figure-2. Each step of the classification method is discussed in the subsections given below.

3.1. Pre-Processing

Sensor data is an inherently noisy form. In this regard, the PhysioNet dataset used in this study is also noisy. To remove noise from data, a 5-points median filtering is used. After the filtering process, the data are normalized according to the body mass index of the individual.

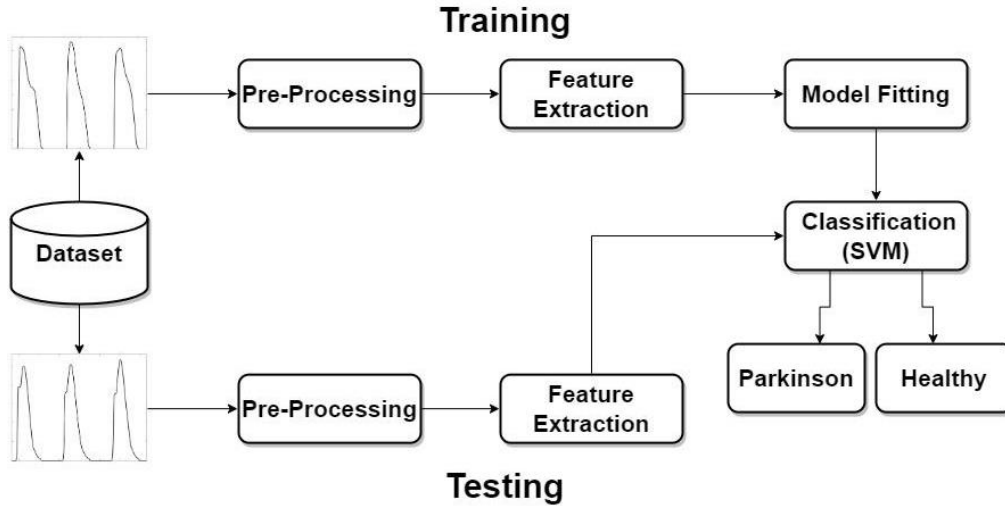


Figure 2. Classification stage of the PM

Moreover, to ignore the initial effect of the gait, the first 20 seconds of the gait are not taken into consideration.

3.2. Feature Extraction

To distinguish individuals with PD from healthy individuals, distinctive features are necessary to be used as a medium. At this stage, features are obtained by using 8 sensors ($S_i, i = 1, 2, \dots, 8$) data placed on the sole of the left foot. The methods used to obtain the feature matrix are given in Figure 3. Each feature extraction stage is explained in the following sections.

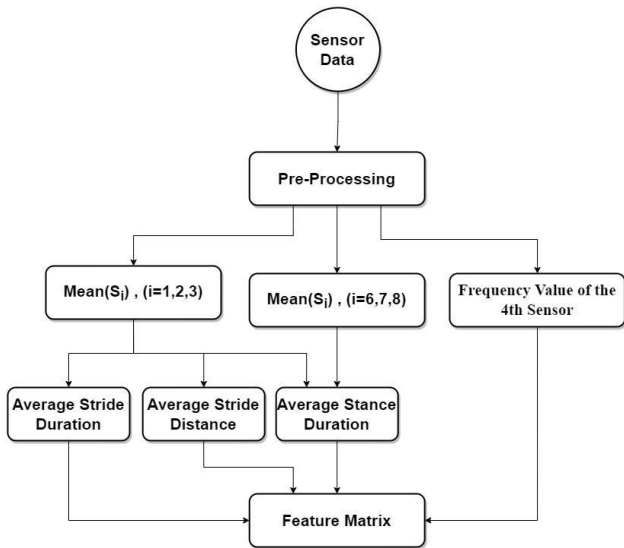


Figure 3. Feature extraction stage of the PM.

3.2.1. Frequency Value of the Sensors

At the feature extraction stage, first of all, the maximum pressure values of the sensor data of the GA, JU, and SI datasets are considered. The distribution of the maximum pressure values for each observation value of

the sensors is examined. In this context, histograms are created using the frequency values of the dominant sensors. Sensor-based histogram graphs of GA, JU, and SI datasets are given in Figure 4, Figure 5, and Figure 6, respectively. Histograms are obtained separately for healthy individuals and people with Parkinson's disease. According to the histogram graphs, the differences in the frequency values of the 4th sensor between Parkinson's patients and healthy individuals can be seen. While the difference is clear in the JU and SI datasets, the difference is less so in the GA dataset. In all datasets, the frequency value of the related sensor is found to be lower for healthy individuals than for Parkinson's patients. Exploiting the frequency differences, the frequency value of the 4th sensor for Parkinson's patients and healthy individuals is determined as a feature.

3.2.2. Average Stride Duration and Average Stride Distance

When Figure 4, Figure 5, and Figure 6 are examined, it can be seen that the frequency values of the $S_1, S_2,$ and S_3 sensors are distinctive between healthy individuals and individuals with PD. These sensors are located at the heel of the left foot, as shown in Figure 1. To alleviate computational complexity, $S_1, S_2,$ and S_3 sensors are combined, and the combined sensor is used for the feature extraction process. In this context, the sensor to represent the sole of the foot was calculated by the average of the $S_1, S_2,$ and S_3 sensors. The averaging process is given in Equation (1).

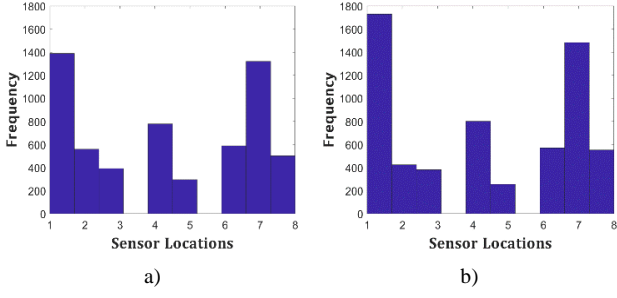


Figure 4. Frequency values of the sensors for the GA dataset. a) Healthy individuals. b) Parkinson's patients.

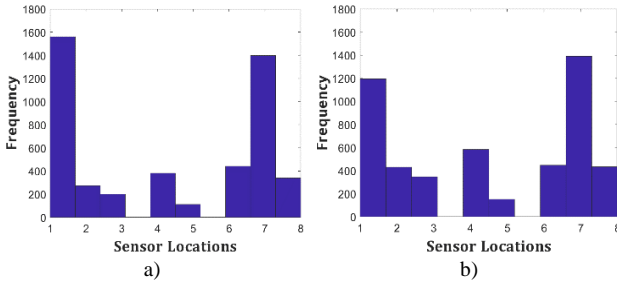


Figure 5. Frequency values of the sensors for the JU dataset. a) Healthy individuals. b) Parkinson's patients.

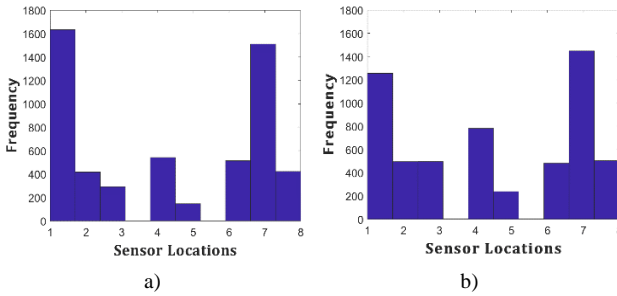


Figure 6. Frequency values of the sensors for the SI dataset. a) Healthy individuals. b) Parkinson's patients.

$$\underline{S}_{(1,2,3)} = \frac{1}{3} \sum_{i=1}^3 S_i \quad (1)$$

Stride duration and stride distance are calculated using $\underline{S}_{(1,2,3)}$. Then, the average of the stride duration and stride distance is calculated. Similarly, the average stride distance is obtained by taking the average of the stride distance.

3.2.3. Average Stance Duration

When Figure 4, Figure 5, and Figure 6 are examined, it can be seen that the frequency values of the S_6 , S_7 , and S_8 sensors are distinctive between healthy individuals and Parkinson's patients. As shown in Figure 1, the S_6 , S_7 , and S_8 sensors are located at the tip of the left foot. The same procedure applied for the heel of the foot is performed for the sensors at the tip of the foot. The sensor to represent

the tip of the foot is calculated by averaging the S_6 , S_7 , and S_8 sensors. The averaging process is given in Equation (2).

$$\bar{S}_{(6,7,8)} = \frac{1}{3} \sum_{i=6}^8 S_i \quad (2)$$

Stance duration is calculated using $\underline{S}_{(1,2,3)}$ and $\bar{S}_{(6,7,8)}$. The average of the stance duration is then calculated.

The features to be used in the classification stage are determined as average stride duration, average stride distance, average stance duration, and the frequency value of the 4th sensor.

3.3. Classification Stage

In this study, an SVM-based binary classification algorithm is preferred. The classification performance of the PM is evaluated under Linear, Gaussian, Polynomial, and RBF kernel functions, separately.

In the classification phase, a 5-fold cross-validation method is applied. Since the number of observations in the dataset is not high, 10-fold cross-validation, which is frequently used in the literature, is not preferred.

4. Results and Discussion

In classification performance evaluation, datasets are considered separately and as a whole. The accuracy, sensitivity, and specificity values are used as performance criteria. To calculate the accuracy, the number of correctly classified predictions is divided by all predictions, as shown in Equation (3).

$$Accuracy = \frac{TP + TN}{TP + TN + FP + FN} \quad (3)$$

The TP value represents the number of positive predictions assigned to the correct class. The TN value indicates the number of negative predictions assigned to the correct class. The FP value corresponds to the number of positive predictions assigned to the wrong class. The FN value corresponds to the number of negative predictions assigned to the wrong class. In the classification process, the TP corresponds to Parkinson's patients, while the TN corresponds to healthy individuals. In this paper, sensitivity, specificity, and Matthew's correlation coefficient (MCC) criteria are also considered for performance comparison. MCC score takes a value between -1 and 1 where +1 corresponds to the perfect prediction and -1 means the worst prediction.

Sensitivity, which is known as the true positive rate,

is calculated in the following Equation (4).

$$Sensitivity = \frac{TP}{TP + FN} \quad (4)$$

Specificity, namely true negative rate, is calculated in Equation (5).

$$Specificity = \frac{TN}{TN + FP} \quad (5)$$

MCC is calculated as follows,

$$MCC = \frac{(TP \times TN - FP \times FN)}{\sqrt{(TP + FP)(TP + FN)(TN + FP)(TN + FN)}} \quad (6)$$

The classification results of the proposed method under different kernel functions are given in Table 3 and Table 4. The experimental results in Table 3 are obtained under maximum classification performance while the experimental results in Table 4 are achieved under average classification performance.

According to the results given in Table 3 and Table 4, it is seen that gaussian and linear kernel classification performs better classification performance, in general. It is important to note that, in the GA, SI, and JU datasets, the numbers of Parkinson's patients and healthy individuals are few. Therefore, incorrect classification of an observation value can cause serious deviations in accuracy values.

Table 3. Maximum classification results according to cross-validation.

Kernel \ Dataset	5- Fold Cross Validation			
	GA	SI	JU	All
Linear	88.9	84.0	90.9	84.8
Gaussian	88.9	84.6	90.9	84.8
Polynomial	88.9	84.6	90.0	81.8
RBF	88.9	84.6	81.8	78.8

Table 4. Average classification results according to cross-validation.

Kernel \ Dataset	5- Fold Cross Validation			
	GA	SI	JU	All
Linear	81.1	73.2	85.1	76.9
Gaussian	78.9	78.1	79.6	75.7
Polynomial	78.9	74.8	83.4	74.5
RBF	78.9	75.1	76.0	75.7

Figure 7 shows the receiver operating characteristic

(ROC) curve of the proposed classification model. The ROC curve is obtained by calculating Sensitivity and (1-Specificity) values at different threshold values. Considering the area under the curve (AUC), the PM achieves robust classifier performance under different thresholds.

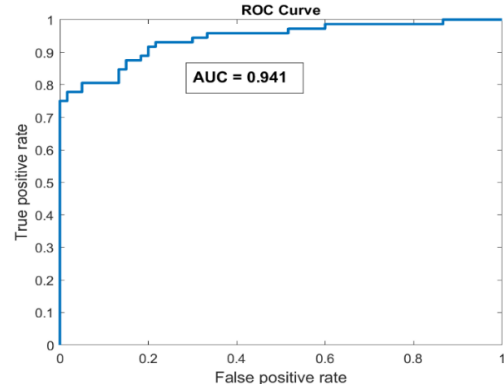


Figure 7. ROC Curve of the Classification Model

Performance comparison between PM and other methods in terms of accuracy is provided in Table 5. Similarly, a performance comparison between PM and other methods in terms of sensitivity, specificity, and MCC criteria is given in Table 6. The results of the PM in both Tables are obtained under the Gaussian kernel. Comparison is carried out according to each dataset and to the whole dataset, separately. Considering the classification accuracies denoted in Table 5, it has been seen that the classification results obtained with the PM can compete with the other methods in terms of accuracy. Considering the classification results given in Table 6, the PM has satisfactory performance with regard to the compared methods in terms of sensitivity and specificity. As seen in Table 6, the PM has balanced accordance between the predicted classes and the real classes in terms of MCC score.

Table 5. Performance comparison between PM and other methods in terms of accuracy.

Related works \ Dataset	Accuracy			
	GA	SI	JU	ALL
[7]	91.49	92.19	90.91	-
[8]	-	-	-	81.0
[9]	-	-	-	86.7
[10]	-	-	-	77.3
[12]	92.25	90.0	92.5	86.9
[14]	88.88	100	100	-
[15]	92.92	90.70	76.56	92.9
[16]	-	-	-	88.9
[17]	-	-	-	88.7
[18]	-	-	-	88.1
PM	88.9	84.6	90.9	84.8

Table 6. Performance comparison between PM and other methods in terms of sensitivity, specificity, and MCC.

Dataset Related works	Sensitivity				Specificity				MCC			
	GA	SI	JU	ALL	GA	SI	JU	ALL	GA	SI	JU	ALL
[7]	0.77	0.94	0.74	-	0.55	0.90	0.83	-	-	-	-	-
[8]	-	-	-	0.86	-	-	-	0.76	-	-	-	-
[9]	-	-	-	-	-	-	-	-	-	-	-	-
[10]	-	-	-	0.81	-	-	-	0.65	-	-	-	-
[12]	-	-	-	0.72	-	-	-	0.81	-	-	-	-
[14]	-	-	-	-	-	-	-	-	-	-	-	-
[15]	-	-	-	0.88	-	-	-	0.88	-	-	-	-
[16]	-	-	-	0.89	-	-	-	0.82	-	-	-	-
[17]	-	-	-	-	-	-	-	-	-	-	-	-
[18]	-	-	-	-	-	-	-	-	-	-	-	-
PM	0.86	1	1	0.92	1	0.60	0.80	0.80	0.76	0.70	0.83	0.71

Table 7. Comparison of feature dimension between PM and other methods.

Related works	[7]	[8]	[9]	[10]	[12]	[14]	[15]	[16]	[17]	[18]	PM
Number of Features	60	100	156	40	10	12	30	108	2328	1472	4

4.1. Time Complexity Analysis in Feature Extraction

In a typical classification task, the feature extraction stage can be crucial for the performance of classification. An increase in the number of features can lead to a curse of dimensionality as well as increase the classification performance. As the number of features increases, the feature space also grows. In this regard, the execution time generally increases with the number of features. So, a huge amount of computation can be needed for the classification task. This paper proposes a low-dimensional feature vector representation for the PD classification task.

Table 7 shows the number of features used in PM and in other methods. It can be seen that the number of features used in PM is significantly less than the compared methods. The methods in [17,18] apply to deep learning approaches to obtain features while the method in [8] uses the PCA approach to reduce the dimension of the feature space. On the other hand, the methods in [12, 14] make use of the time-frequency domain, while the methods in [11, 13] use only the frequency domain. Thanks to PM, only 4 features are considered in the time domain.

Besides the number of features, time complexity also needs to be taken into account. Table 8 shows the time complexity of the feature extraction methods used in PM. As seen in the Table, the features can be extracted with $O(n)$ complexity at the worst case.

Table 8. Time Complexity in Feature Extraction

Features	Time Complexity
Frequency Value of the Sensors	$O(n)$
Average Stance Duration	$O(n) + O(\log n)$
Average Stride Duration	$O(n)$
Average Stride Distance	$O(n)$
Total	$4O(n) + O(\log n)$

5. Conclusions

In this study, a low-dimensional feature vector representation is proposed to detect Parkinson's disease. Thanks to the proposed method, a small number of features with low time complexity can be used without compromising the classification performance.

In the literature, a large number of features are usually utilized at the classification stage. In addition, extracting the features from different domains such as time and frequency can increase the computational cost. By implementing the proposed method, satisfactory classification results are achieved using a small number of features obtained from only the time domain.

According to the classification results obtained with the accuracy criterion, high classification performance, up to 85%, is obtained under the whole dataset. On the other hand, superior classification performance, up to 91%, is obtained when the datasets are evaluated individually. Moreover, according to the sensitivity criterion, the proposed method exhibits the best performance among the compared methods.

Declaration of Ethical Standards

The materials and methods used in this study do not require ethical committee permission and/or legal-special permission.

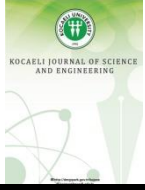
Conflict of Interest

The authors declare that they have no known competing financial interests or personal relationships that could have appeared to influence the work reported in this paper.

References

- [1] Channa A., Baqai A., Ceylan R., 2019. Design and Application of a Smart Diagnostic System for Parkinson's Patients using Machine Learning. (IJACSA) International Journal of Advanced Computer Science and Applications, **10**(6).
- [2] Li D., Xie Q., Jin Q., Hirasawa K., 2016. A Sequential Method using Multiplicative Extreme Learning Machine for Epileptic Seizure Detection. Neurocomputing, **214**, pp. 692-707.
- [3] Yıldırım M. and Yıldız A. 2017. Farklı zaman ölçekli EEG işaretlerinden epilepsi nöbetinin otomatik tespiti. Dicle University Journal of Engineering, **8**(4), pp. 745-757.
- [4] Banaie M., Pooyan M., Mikaili M., 2011. Introduction and application of an automatic gait recognition method to diagnose movement disorders that arose of similar causes. Expert Systems with Applications, **38**(6), pp. 7359-7363.
- [5] Fahn S. 2003. Description of Parkinson's disease as a clinical syndrome. Annals of the New York Academy of Sciences, **991**(1), pp. 1-14.
- [6] Sveinbjornsdottir S. 2016. The clinical symptoms of Parkinson's disease. Journal of neurochemistry, **139**, pp. 318-324.
- [7] Jane Y. N., Nehemiah H. K., Arputharaj K. 2016. A Q-backpropagated time delay neural network for diagnosing severity of gait disturbances in Parkinson's disease. Journal of biomedical informatics, **60**, pp. 169-176.
- [8] Medeiros L., Almeida H., Dias L., Perkusich M., Fischer R. 2016. A gait analysis approach to track Parkinson's disease evolution using principal component analysis. In 2016 IEEE 29th International Symposium on Computer-Based Medical Systems (CBMS), pp. 48-53. June.
- [9] Baby M. S., Saji A. J., Kumar C. S. 2017. Parkinsons disease classification using wavelet transform-based feature extraction of gait data. In 2017 International Conference on Circuit, Power and Computing Technologies (ICCPCT), pp. 1-6, April.
- [10] Lee S. H., Lim J. S. 2012. Parkinson's disease classification using gait characteristics and wavelet-based feature extraction. Expert Systems with Applications, **39**(8), pp. 7338-7344.
- [11] Lim C. M., Ng H., Yap T. T. V., Ho C. C. 2015. Gait analysis and classification on subjects with Parkinson's disease. Jurnal Teknologi, **77**(18).
- [12] Perumal S. V., Sankar R. 2016. Gait and tremor assessment for patients with Parkinson's disease using wearable sensors. Ict Express, **2**(4), pp. 168-174.
- [13] Abdulhay E., Arunkumar N., Narasimhan K., Vellaiappan E., Venkatraman V. 2018. Gait and tremor investigation using machine learning techniques for the diagnosis of Parkinson disease. Future Generation Computer Systems, **83**, pp. 366-373.
- [14] Andrei A. G., Tăuțan A. M., Ionescu B. 2019. Parkinson's disease detection from gait patterns. In 2019 E-Health and Bioengineering Conference (EHB), pp. 1-4, November.
- [15] Özel E., Tekin R., Kaya Y., 2021. Implementation of Artifact Removal Algorithms in Gait Signals for Diagnosis of Parkinson Disease. Traitement du Signal, **38**(3).
- [16] Ertuğrul Ö. F., Kaya Y., Tekin, R., Almalı M. N., 2016. Detection of Parkinson's disease by shifted one dimensional local binary patterns from gait. Expert Systems with Applications, **56**, pp. 156-163.
- [17] Hoang N. S., Cai Y., Lee C. W., Yang Y. O., Chui C. K., Chua M. C. H., 2019. Gait classification for Parkinson's Disease using Stacked 2D and 1D Convolutional Neural Network. In 2019 International Conference on Advanced Technologies for Communications (ATC), pp. 44-49, October.
- [18] Johri A., Tripathi A., 2019. Parkinson disease detection using deep neural networks. In 2019 Twelfth International Conference on Contemporary Computing (IC3), pp. 1-4, August.
- [19] Goldberger A., Amaral L., Glass L., Hausdorff J., Ivanov P. C., Mark R., Stanley H. E. 2000. PhysioBank, PhysioToolkit, and PhysioNet: Components of a new research resource for complex physiologic signals. Circulation [Online], **101** (23), pp. e215-e220.

- [20] Frenkel-Toledo S., Giladi N., Peretz C., Herman T., Gruendlinger L., Hausdorff J. M., 2005. Effect of gait speed on gait rhythmicity in Parkinson's disease: variability of stride time and swing time respond differently. *Journal of neuroengineering and rehabilitation*, **2**(1), pp. 1-7.
- [21] Frenkel-Toledo S., Giladi N., Peretz C., Herman T., Gruendlinger L., Hausdorff J. M., 2005. Treadmill walking as an external pacemaker to improve gait rhythm and stability in Parkinson's disease. *Movement disorders: official journal of the Movement Disorder Society*, **20**(9), pp. 1109-1114.
- [22] Hausdorff J. M., Lowenthal J., Herman T., Gruendlinger L., Peretz C., Giladi N., 2007. Rhythmic auditory stimulation modulates gait variability in Parkinson's disease. *European Journal of Neuroscience*, **26**(8), pp. 2369-2375.
- [23] Yogev G., Giladi N., Peretz C., Springer S., Simon E. S., Hausdorff J. M., 2005. Dual tasking, gait rhythmicity, and Parkinson's disease: which aspects of gait are attention demanding? *European journal of neuroscience*, **22**(5), pp. 1248-1256.
- [24] Gümüşçü A., 2019. Giyilebilir Yürüyüş Analiz Sensörü ile Kişi Sınıflandırmasının Öznitelik Seçme Algoritmaları ile İyileştirilmesi. *Fırat Üniversitesi Mühendislik Bilimleri Dergisi*, **31**(2), pp. 463-471.



Undetermined Coefficients Method for Sequential Fractional Differential Equations

Sertaç ERMAN^{1,*} ¹ Department of Engineering Fundamental Sciences, Sakarya University of Applied Sciences, Sakarya, Turkey, **ORCID:** 0000-0002-3156-5173

Article Info

Research paper

Received : July 19, 2022

Accepted : December 14, 2022

Keywords

*Fractional Differential Equation
Undetermined Coefficients
Caputo Derivative
Particular Solution*

Abstract

The undetermined coefficients method is presented for nonhomogeneous sequential fractional differential equations involving Caputo fractional derivative of order $n\alpha$ where $n - 1 < n\alpha \leq n$ and $n \in \mathbb{N}$. By employing the proposed method, a particular solution of the considered equation is obtained. Some details about estimating the particular solution required to apply this method are explained. This method is shown to be particularly effective for nonhomogeneous fractional differential equations when the fractional differential equations involve some specific right-hand side functions.

1. Introduction

Fractional calculus has attracted the attention of researchers in recent decades, as modeling using fractional differential equations is convenient for estimating the evolutionary tendency of the systems affected by past memories.

This paper deals with the following nonhomogeneous sequential fractional differential equation

$$\sum_{i=0}^n b_i D^{i\alpha} u(t) = f(t), \quad (1)$$

where $n - 1 < n\alpha \leq n$, $b_i \in \mathbb{R}$, $n \in \mathbb{N}$, and $f(t) \in C^\infty(0, t)$. $D^{n\alpha}$ is called sequential fractional derivative operator and it is defined as follows

$$D^{n\alpha} u(t) = D^{(n-1)\alpha} ({}^c D^\alpha u(t)),$$

where ${}^c D^\alpha$ is the Caputo derivatives.

The sequential fractional derivative equation is first investigated in the monograph [1]. Its generalized version

is then studied in [2]. Recently, many studies have been considered on the solutions of sequential fractional differential equations. These studies include different types of fractional derivatives, initial values, and boundary values. The uniqueness and existence of the solution of the periodic boundary value and the initial value problem for Riemann-Liouville (R-L) sequential fractional differential equations are considered in [3,4]. Similarly, solutions of impulsive R-L sequential fractional differential equations are studied in [5] and some specific solutions of sequential fractional differential equations with R-L derivatives are investigated in [6]. In [7] and [8], the uniqueness and existence of the solution are proved for sequential fractional differential equations involving the Hadamard derivative and Caputo-Hadamard derivative, respectively. Some existing results are obtained for Caputo-type sequential fractional differential equations with three-point, semi-periodic non-local, and mixed-type boundary conditions [9-11]. The uniqueness and Ulam-stability of solutions for specific sequential fractional differential equations involving Caputo derivative are studied in [12]. Additionally, in [13], the solution of Equation (1) is considered for $n = 2$ and $f(t) = 0$. We refer the reader to the papers [14-20] for some recent work on this subject.

* Corresponding Author: sertacerman@subu.edu.tr



The purpose of this article is to examine the method of uncertain coefficients to obtain particular solutions to Equation (1) with some specific functions $f(t)$. The method is a generalization of the well-known method of nonhomogeneous linear ordinary differential equations for sequential fractional differential equations with Caputo derivative. A similar method has been used for nonhomogeneous differential equations involving conformable fractional derivatives in [21], whereas there is no study in the literature for the Caputo derivative.

The layout of this article is as follows. In Section 2, some definitions and applications of fractional calculus are presented. The method for the solution to the related problem is proposed in Section 3, and an illustrative example is given to present the application of the method in Section 4. Finally, some conclusions are described in the last section.

2. Preliminaries

Definition 1: The Caputo fractional derivative of order α is defined as [22]:

$${}^c D^\alpha u(t) = \begin{cases} \frac{1}{\Gamma(n-\alpha)} \int_0^t (t-s)^{n-\alpha-1} \left(\frac{d^n u(s)}{ds^n} \right) ds, & n-1 < \alpha < n, \\ \frac{d^n u(s)}{ds^n}, & \alpha = n. \end{cases}$$

For $0 < \alpha < 1$, the Caputo fractional derivative is formed as:

$${}^c D^\alpha u(t) = \begin{cases} \frac{1}{\Gamma(1-\alpha)} \int_0^t \frac{u'(s)}{(t-s)^\alpha} ds, & 0 < \alpha < 1, \\ u'(t), & \alpha = 1. \end{cases}$$

Definition 2: The sequential Caputo fractional derivative operator of order $n-1 < \alpha \leq n$ is defined as [13]:

$$D^{n\alpha} u(t) = D^{(n-1)\alpha} ({}^c D^\alpha u(t)).$$

Definition 3: The Mittag-Leffler function is defined as:

$$E_\alpha(z) = \sum_{k=0}^{\infty} \frac{z^k}{\Gamma(\alpha k + 1)},$$

where $Re(\alpha) > 0$ [23].

Definition 4: The Mittag-Leffler function with 2-parameters is defined as:

$$E_{\alpha,\beta}(z) = \sum_{k=0}^{\infty} \frac{z^k}{\Gamma(\alpha k + \beta)},$$

where $\alpha, \beta \in \mathbb{C}$ and $Re(\alpha) > 0$ [23].

Definition 5: The Mittag-Leffler function with 3-parameters is defined as:

$$E_{\alpha,\beta}^\gamma(z) = \frac{1}{\Gamma(\gamma)} \sum_{k=0}^{\infty} \frac{\Gamma(\gamma+k)z^k}{k! \Gamma(\alpha k + \beta)},$$

where α, β and $\gamma \in \mathbb{C}$ and $Re(\alpha) > 0$ [23].

Since $(\gamma)_k := \frac{\Gamma(\gamma+k)}{\Gamma(\gamma)} = \gamma(\gamma+1) \cdots (\gamma+k-1)$ for $\gamma \in \mathbb{N}$, Mittag-Leffler with 3-parameters is rewritten as

$$E_{\alpha,\beta}^\gamma(z) = \sum_{k=0}^{\infty} \frac{(\gamma)_k z^k}{k! \Gamma(\alpha k + \beta)},$$

and holds the following property

$$E_{\alpha,\beta}^\gamma(z) = \frac{1}{\alpha\gamma} \left(E_{\alpha,\beta-1}^{\gamma-1}(z) + (1-\beta+\alpha\gamma) E_{\alpha,\beta}^{\gamma-1}(z) \right),$$

which yields to reduce in the third parameter [24]. By repeatedly applying the property, the third parameter can be reduced to one. That is, a relation can be established between the Mittag-Leffler function with 3-parameters and the Mittag-Leffler function with 2-parameters when $\gamma \in \mathbb{N}$. We refer the reader to the paper [25] for more detail on the Mittag-Leffler function with 3-parameters.

Definition 6: The parametrized form of $f(t) \in C^\infty(0, t)$ is defined as follows:

$$f_\alpha(t) = \sum_{k=0}^{\infty} \frac{d^k f(t)}{dt^k} \Big|_{t=0} \frac{t^k}{\Gamma(\alpha k + 1)}, \tag{2}$$

where $\alpha > 0$.

Definition 7: The 2-parametrized form of $f(t) \in C^\infty(0, t)$ is defined as follows:

$$f_{\alpha,\beta}(t) = \sum_{k=0}^{\infty} \frac{d^k f(t)}{dt^k} \Big|_{t=0} \frac{t^k}{\Gamma(\alpha k + \beta)}, \tag{3}$$

where $\alpha, \beta > 0$.

Remark 1: Parametrized and 2-parametrized forms of function $f(t) = e^t$ are Mittag-Leffler function $E_\alpha(t)$ and Mittag-Leffler function with two parameters $E_{\alpha,\beta}(t)$, respectively. Moreover, the following notations are used for parametrized and 2-parametrized forms of

functions $f(t) = \sin(t)$ and $f(t) = \cos(t)$

$$\begin{aligned} \sin_{\alpha}(t) &= \sum_{k=0}^{\infty} (-1)^k \frac{t^{2k+1}}{\Gamma((2k+1)\alpha+1)}, \\ \sin_{\alpha,\beta}(t) &= \sum_{k=0}^{\infty} (-1)^k \frac{t^{2k+1}}{\Gamma((2k+1)\alpha+\beta)}, \\ \cos_{\alpha}(t) &= \sum_{k=0}^{\infty} (-1)^k \frac{t^{2k}}{\Gamma(2k\alpha+1)}, \\ \cos_{\alpha,\beta}(t) &= \sum_{k=0}^{\infty} (-1)^k \frac{t^{2k}}{\Gamma(2k\alpha+\beta)}. \end{aligned}$$

Theorem 1: Let $f(t) \in C^{\infty}(0, x)$, $\frac{\alpha}{\rho} = m \in \mathbb{N}$ and $r \in \mathbb{C}$. If $\left. \frac{d^k}{dt^k} f(t) \right|_{t=0} = \left. \frac{d^{mk}}{dt^{mk}} f(t) \right|_{t=0}$ for all $k \in \mathbb{N}$, then

$$f_{\alpha,\beta}(rt^{\alpha}) = \frac{1}{m} \sum_{i=1}^m f_{\rho,\beta}(s_i t^{\rho}),$$

where s_i are roots of $s^m = r$.

Proof. By definition of the 2-parametrized form of $f(t)$, we have

$$\sum_{i=1}^m f_{\rho,\beta}(s_i t^{\rho}) = \sum_{k=0}^{\infty} \sum_{i=1}^m c_k \frac{s_i^{k\rho k}}{\Gamma(\rho k + \beta)}, \quad (4)$$

where $c_k = \left. \frac{d^k f(t)}{dt^k} \right|_{t=0}$. On the other hand, the roots s_i of the equation $s^m = r$ satisfy following sum:

$$\begin{cases} \sum_{i=1}^m (s_i)^j = mr^k & \text{if there exist } k \in \mathbb{N} \text{ such that } j = km, \\ 0 & \text{otherwise.} \end{cases} \quad (5)$$

By plugging equation (5) into equation (4), we have

$$\sum_{k=0}^{\infty} \sum_{i=1}^m c_k \frac{s_i^{k\rho k}}{\Gamma(\rho k + \beta)} = \sum_{k=0}^{\infty} c_k \frac{mr^k t^{\alpha k}}{\Gamma(\rho k + \beta)} = m f_{\alpha,\beta}(rt^{\alpha})$$

Theorem 1 shows that the first parameter of a 2-parametrized form of $f(t)$ can be changed under appropriate conditions. Moreover, the following equations are the direct result of theorem 1 for some specific functions $f(t)$.

$$E_{\alpha,\beta}(rt^{\alpha}) = \frac{1}{m} \sum_{i=1}^m E_{\rho,\beta}(s_i t^{\rho}), \quad (6)$$

$$\begin{cases} \sin_{\alpha,\beta}(rt^{\alpha}) = \frac{1}{m} \sum_{i=1}^m \sin_{\rho,\beta}(s_i t^{\rho}) & \text{if } m = 4k + 1, k \in \mathbb{N}, \\ -\frac{1}{m} \sum_{i=1}^m \sin_{\rho,\beta}(s_i t^{\rho}) & \text{if } m = 4k + 3, k \in \mathbb{N}, \end{cases} \quad (7)$$

$$\sin_{\alpha,\beta}(rt^{\alpha}) =$$

$$\frac{1}{m} \sum_{i=1}^m \cos_{\rho,\beta}(s_i t^{\rho}) \quad \text{if } m = 2k + 1, k \in \mathbb{N}, \quad (8)$$

where $\frac{\alpha}{\rho} = m \in \mathbb{N}$.

3. Undetermined Coefficient Method

In this section, we introduce undetermined coefficient method to find a particular solution to the following nonhomogeneous sequential fractional differential equation for specific classes of right-hand side function

$$\sum_{i=0}^n b_i D^{i\alpha} u(t) = f(t), \quad (9)$$

where $n - 1 < n\alpha \leq n$, $b_i \in \mathbb{R}$, and $f(t) \in C^{\infty}(0, t)$.

For $f(t) = 0$, the solutions of homogeneous equation (9) are in the form of $E_{\alpha}(rt^{\alpha})$ where r is the root of the corresponding characteristic equation

$$P(r) = \sum_{i=0}^n b_i r^i. \quad (10)$$

If the characteristic equation (10) has k distinct roots r_i , a solution of equation (9) with $f(t) = 0$ is as follows:

$$u_{h_1} = \sum_{i=1}^k c_i E_{\alpha}(r_i t^{\alpha}),$$

where $c_i \in \mathbb{R}$. Moreover, in [26], the following solutions of the equation (9) with $f(t) = 0$ are obtained if the characteristic equation (10) has k coincident roots r_0

$$u_{h_2} = c_0 E_{\alpha}(r_0 t^{\alpha}) + \sum_{i=1}^{k-1} c_i \frac{t^{i\alpha}}{i\alpha} E_{\alpha,i\alpha}^i(r_0 t^{\alpha}).$$

Theorem 2: Let $f(t) = \sum_{i=0}^m c_i \frac{t^{i\alpha}}{\Gamma(i\alpha+1)}$ in equation (9) where $c_i \in \mathbb{R}$. If the corresponding characteristic equation has no root at $r = 0$, then there are real constants a_0, a_1, \dots, a_m such that

$$u_p = \sum_{i=0}^m a_i \frac{t^{i\alpha}}{\Gamma(i\alpha+1)}, \quad (11)$$

is a particular solution of equation (9).

Proof. By plugging equation (11) into equation (9), we have the following linear algebraic system

$$\begin{bmatrix} b_0 & b_1 & b_2 & \dots & b_m \\ 0 & b_0 & b_1 & \dots & b_{m-1} \\ 0 & 0 & b_0 & \dots & b_{m-2} \\ \vdots & \vdots & \vdots & \ddots & \vdots \\ 0 & 0 & 0 & \dots & b_0 \end{bmatrix} \begin{bmatrix} a_0 \\ a_1 \\ a_2 \\ \vdots \\ a_m \end{bmatrix} = \begin{bmatrix} c_0 \\ c_1 \\ c_2 \\ \vdots \\ c_m \end{bmatrix}. \quad (12)$$

Here $b_0 \neq 0$ since the characteristic equation has no

root at $r = 0$. Thus, the linear algebraic system has a unique solution.

Remark 2: If the characteristic equation has k coincident root at $r = 0$, the particular solution (11) is formed as follows

$$u_p = \sum_{i=k}^{m+k} a_i \frac{t^{i\alpha}}{\Gamma(i\alpha+1)},$$

and the linear algebraic system (12) is reobtained as follows

$$\begin{bmatrix} b_k & b_{k+1} & b_{k+2} & \dots & b_m & 0 & 0 & \dots & 0 \\ 0 & b_k & b_{k+1} & \dots & b_{m-1} & b_m & 0 & \dots & 0 \\ \vdots & \ddots & \ddots & \ddots & \vdots & \vdots & \ddots & \ddots & \vdots \\ 0 & \dots & 0 & b_k & b_{k+1} & b_{k+2} & \dots & b_m & 0 \\ 0 & \dots & 0 & 0 & b_k & b_{k+1} & \dots & b_{m-1} & b_m \\ 0 & \dots & 0 & 0 & 0 & b_k & \dots & b_{m-2} & b_{m-1} \\ \vdots & \ddots & \vdots & \vdots & \vdots & \vdots & \ddots & \vdots & \vdots \\ 0 & 0 & 0 & 0 & 0 & 0 & \dots & b_k & b_{k+1} \\ 0 & 0 & 0 & 0 & 0 & 0 & \dots & 0 & b_k \end{bmatrix} \begin{bmatrix} a_k \\ a_{k+1} \\ a_{k+2} \\ \vdots \\ a_{m+k} \end{bmatrix} = \begin{bmatrix} c_0 \\ c_1 \\ c_2 \\ \vdots \\ c_m \end{bmatrix}.$$

Remark 3: Let $q_0 < q_1 < \dots < q_m$ be positive real numbers and $GCD(\alpha, q_0, q_1, \dots, q_m) = \beta$. In Theorem 2, the right-hand side function is taken as $f(t) = P(t^\alpha)$, where $P(t)$ is a polynomial. However, more generally, if the right-hand side function is of the form $f(x) = \sum_{i=0}^m c_i t^{q_i}$, the particular solution of the equation is considered as follows

$$u_p = \sum_{i=0}^k a_i \frac{t^{i\beta}}{\Gamma(i\beta+1)},$$

where $q_m = k\beta$, $k \in \mathbb{N}$. In this case, the characteristic equation is established by using $E_\beta(rt^\beta)$

Theorem 3: Let $f(t) = E_q(ct^q)$ in equation (9) and $GCD(\alpha, q) = \beta$. If the characteristic equation formed using $E_\beta(rt^\beta)$ has no root at $r = s_i$ where s_i are roots of $s^m = c$ for $\frac{q}{\beta} = m \in \mathbb{N}$, then there are real constants a_0, a_1, \dots, a_m such that

$$u_p = \sum_{i=1}^m a_i E_\beta(s_i t^\beta), \tag{13}$$

is a particular solution of equation (9).

Proof. From equation (6), we have

$$f(t) = E_q(ct^q) = \frac{1}{m} \sum_{i=1}^m E_\beta(s_i t^\beta).$$

On the other hand, by plugging equation (13) into equation (9), we obtain the following equality for $i = 1, 2, \dots, m$,

$$a_i (\sum_{k=0}^n b_k (s_i)^k) \sum_{i=1}^m E_\beta(s_i t^\beta) = \frac{1}{m} \sum_{i=1}^m E_\beta(s_i t^\beta),$$

which gives

$$a_i = \frac{1}{m \sum_{k=0}^n b_k (s_i)^k}.$$

Since the characteristic equation has no root at $r = s_i$, $\sum_{k=0}^n b_k (s_i)^k \neq 0$.

Remark 4 Let s be a root of $s^m = c$ in Theorem 3. If the characteristic equation has k coincident root at $r = s$, a particular solution (13) is formed as follows:

$$u_p = \frac{t^{k\beta}}{k\beta} E_{\beta, k\beta}^k(st^\beta).$$

Theorem 4 Let $f(t) = \sin_q(ct^q) + \cos_q(ct^q)$ in equation (9), $GCD(\alpha, q) = \beta$ and $\frac{q}{\beta} = m$ be odd number. If the corresponding characteristic equation has no root at $r = s_i$ where s_i are roots of $s^m = c$, then there are real constants a_0, a_1, \dots, a_m and d_0, d_1, \dots, d_m such that

$$u_p = \sum_{i=1}^m a_i \sin_\beta(ct^\beta) + d_i \cos_\beta(ct^\beta), \tag{14}$$

is a particular solution of equation (9).

By the principle of superposition, if the right-hand side function $f(t)$ is a linear combination of the functions in Theorem 1-4, a particular solution of equation (9) is a linear combination of the particular solutions defined in the related theorems. Additionally, the general solution is $u_g = u_h + u_p$ where u_h is the solution of homogeneous equation (9) with $f(t) = 0$, and u_p is the particular solution of equation (9).

4. Illustrative Example

Example: Let us consider the general solution of the following equation

$$D^{\frac{6}{4}}u(t) + D^{\frac{3}{4}}u(t) - 2u(t) = e^t + t. \tag{15}$$

The characteristic equation $r^2 + r - 2 = 0$ of equation (15) is formed using $E_{\frac{3}{4}}(rt^{\frac{3}{4}})$, so $r = 1$ and $r = -2$ are 1-fold roots. Hence, the homogeneous solution is obtained as follows

$$u_h = c_1 E_{\frac{3}{4}}(t^{\frac{3}{4}}) + c_2 E_{\frac{3}{4}}(-2t^{\frac{3}{4}}), \tag{16}$$

where $c_1, c_2 \in \mathbb{R}$.

Since $GCD(\frac{3}{4}, 1) = \frac{1}{4}$, the characteristic equation is formed using $E_{\frac{1}{4}}(\lambda t^{\frac{1}{4}})$ as follows

$$\lambda^6 + \lambda^3 - 2 = 0, \tag{17}$$

and the roots of the equation are

$$\lambda_1 = 1, \lambda_{2,3} = -\frac{1}{2} \pm i\frac{\sqrt{3}}{2}, \lambda_4 = -\sqrt[3]{2}, \lambda_{5,6} = 2^{-\frac{2}{3}}(1 \pm i\sqrt{3})$$

In order to determine the form of the particular solution, we use the following equality from equation (6)

$$\begin{aligned} e^t &= \frac{1}{4} \left[E_{\frac{1}{4}}(t^{\frac{1}{4}}) + E_{\frac{1}{4}}(-t^{\frac{1}{4}}) + E_{\frac{1}{4}}(it^{\frac{1}{4}}) + E_{\frac{1}{4}}(-it^{\frac{1}{4}}) \right] \\ &= \frac{1}{4} \left[E_{\frac{1}{4}}(t^{\frac{1}{4}}) + E_{\frac{1}{4}}(-t^{\frac{1}{4}}) + 2\cos_{\frac{1}{4}}(t^{\frac{1}{4}}) \right]. \end{aligned}$$

Therefore, the particular solution is considered as follows

$$\begin{aligned} u_p &= a_0 + a_1 \frac{t^{\frac{1}{4}}}{\Gamma(\frac{5}{4})} + a_2 \frac{t^{\frac{2}{4}}}{\Gamma(\frac{3}{2})} + a_3 \frac{t^{\frac{3}{4}}}{\Gamma(\frac{7}{4})} + a_4 t \\ &\quad + a_5 \frac{t^{\frac{1}{4}}}{\frac{1}{4}} E_{\frac{1}{4}}(t^{\frac{1}{4}}) + a_6 E_{\frac{1}{4}}(-t^{\frac{1}{4}}) \\ &\quad + a_7 \cos_{\frac{1}{4}}(t^{\frac{1}{4}}) + a_8 \sin_{\frac{1}{4}}(t^{\frac{1}{4}}). \end{aligned}$$

The particular solution contains the term $\frac{t^{\frac{1}{4}}}{\frac{1}{4}} E_{\frac{1}{4}}(t^{\frac{1}{4}})$ because the characteristic equation has a 1-fold root of $\lambda = 1$. Substituting u_p in equation (15), we have

$$a_0 = a_2 = a_3 = 0, a_1 = \frac{1}{4}, a_4 = -\frac{1}{2}, a_5 = \frac{1}{36}, a_6 = -\frac{1}{8}, a_7 = -\frac{3}{5}, a_8 = -\frac{1}{5}.$$

Hence, the general solution of the equation (15) is obtained as follows

$$\begin{aligned} u_g &= c_1 E_{\frac{3}{4}}(t^{\frac{3}{4}}) + c_2 E_{\frac{3}{4}}(-2t^{\frac{3}{4}}) + \frac{t^{\frac{1}{4}}}{4\Gamma(\frac{5}{4})} - \frac{t}{2} + \frac{t^{\frac{1}{4}}}{9} E_{\frac{1}{4}}(t^{\frac{1}{4}}) \\ &\quad - \frac{1}{8} E_{\frac{1}{4}}(-t^{\frac{1}{4}}) \\ &\quad - \frac{1}{5} \left[3\cos_{\frac{1}{4}}(t^{\frac{1}{4}}) + \sin_{\frac{1}{4}}(t^{\frac{1}{4}}) \right]. \end{aligned}$$

It is clear from equation (6) that the homogeneous

solution (16) is equal to the homogeneous solution obtained from the roots of the characteristic equation (17).

5. Conclusions

The particular solution to Equation (1) is constructed when Equation (1) involves the right-hand side functions $f(t) = \sum_{k=0}^m c_k \frac{t^k}{k!}$, $f(t) = e^t$, $f(t) = \sin(t)$, and $f(t) = \cos(t)$ or their parametrized forms or linear combinations of them. To obtain the particular solution, the method of uncertain coefficients is presented for Caputo sequential fractional derivative equation of order $n\alpha$ where $n - 1 < n\alpha \leq n$ and $n \in \mathbb{N}$. This method is based on the appropriate particular solution estimation. The necessary details for proper estimation have been obtained. It is shown that Equation (1) is transformed into a linear algebraic equation with the benefit of proper solution estimation. Therefore, the method discussed is particularly effective for nonhomogeneous fractional differential equations.

Declaration of Ethical Standards

The author of this article declares that the materials and methods used in this study do not require ethical committee permission and/or legal-special permission.

Conflict of Interest

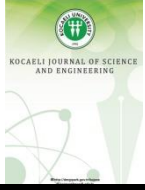
The authors declare that they have no known competing financial interests or personal relationships that could have appeared to influence the work reported in this paper.

References

- [1] Miller K. S., Ross B., 1993. An introduction to the fractional calculus and fractional differential equations. Wiley.
- [2] Podlubny I., 1999. Fractional differential equations an introduction to fractional derivatives, fractional differential equations, to methods of their solution and some of their applications. Academic Press.
- [3] Wei Z., Dong W., 2011. Periodic boundary value problems for Riemann-Liouville sequential fractional differential equations. Electronic Journal of Qualitative Theory of Differential Equations, **87**, pp.1-13. <https://doi.org/10.14232/ejqtde.2011.1.87>
- [4] Wei Z., Li Q., Che J., 2010. Initial value problems for fractional differential equations involving Riemann-Liouville sequential fractional derivative. Journal of

- Mathematical Analysis and Applications, **367**(1), pp.260-272.
<https://doi.org/10.1016/j.jmaa.2010.01.023>
- [5] Bai C., 2011. Impulsive periodic boundary value problems for fractional differential equation involving Riemann–Liouville sequential fractional derivative. *Journal of Mathematical Analysis and Applications*, **384**(2), pp.211-231.
<https://doi.org/10.1016/j.jmaa.2011.05.082>
- [6] Băleanu D., Mustafa O. G., Agarwal R. P., 2011. On L_p -solutions for a class of sequential fractional differential equations. *Applied Mathematics and Computation*, **218**(5), pp.2074-2081.
<https://doi.org/10.1016/j.amc.2011.07.024>
- [7] Klimek M., 2011. Sequential fractional differential equations with Hadamard derivative. *Communications in Nonlinear Science and Numerical Simulation*, **16**(12), pp. 4689-4697.
<https://doi.org/10.1016/j.cnsns.2011.01.018>
- [8] Awadalla M., Abuasbeh K., 2022. On system of nonlinear sequential hybrid fractional differential equations. *Mathematical Problems in Engineering*, 2022, pp.1-8. <https://doi.org/10.1155/2022/8556578>
- [9] Ahmad B., Nieto J. J., 2012. Sequential fractional differential equations with three-point boundary conditions. *Computers & Mathematics with Applications*, **64**(10), pp.3046-3052.
<https://doi.org/10.1016/j.camwa.2012.02.036>
- [10] Ahmad B., Ntouyas S. K., Alsaedi A., 2019. Sequential fractional differential equations and inclusions with semi-periodic and nonlocal integro-multipoint boundary conditions. *Journal of King Saud University - Science*, **31**(2), pp.184-193.
<https://doi.org/10.1016/j.jksus.2017.09.020>
- [11] Zhang H., Li Y., Yang J., 2020. New sequential fractional differential equations with mixed-type boundary conditions. *Journal of Function Spaces*, 2020, pp.1-9. <https://doi.org/10.1155/2020/6821637>
- [12] Mohamed H., 2022. Sequential fractional pantograph differential equations with nonlocal boundary conditions: Uniqueness and Ulam-Hyers-Rassias stability. *Results in Nonlinear Analysis*.
<https://doi.org/10.53006/rna.928654>
- [13] Sambandham B., Vatsala A., 2015. Basic results for sequential caputo fractional differential equations. *Mathematics*, **3**(1), pp.76-91.
<https://doi.org/10.3390/math3010076>
- [14] Hao Z., Chen B., 2022. The unique solution for sequential fractional differential equations with integral multi-point and anti-periodic type boundary conditions. *Symmetry*, **14**(4), 761.
<https://doi.org/10.3390/sym14040761>
- [15] Awadalla M., 2022. Some existence results for a system of nonlinear sequential fractional differential equations with coupled nonseparated boundary conditions. *Complexity*, 2022, pp.1-17.
<https://doi.org/10.1155/2022/8992894>
- [16] Benmehidi H., Dahmani Z., 2022. On a sequential fractional differential problem with Riemann-Liouville integral conditions. *Journal of Interdisciplinary Mathematics*, **25**(4), pp.893-915.
<https://doi.org/10.1080/09720502.2020.1861789>
- [17] Almalahi M. A., Panchal S. K., Abdo M. S., Jarad F., 2022. On atangana–baleanu-type nonlocal boundary fractional differential equations. *Journal of Function Spaces*, 2022, pp.1-17.
<https://doi.org/10.1155/2022/1812445>
- [18] Baitiche Z., Guerbaty K., Benchohra M., Zhou Y., 2019. Boundary value problems for hybrid caputo fractional differential equations. *Mathematics*, **7**(3), 282. <https://doi.org/10.3390/math7030282>
- [19] Aydogan S. M., Sakar F. M., Fatehi M., Rezapour S., Masiha H. P., 2021. Two hybrid and non-hybrid k -dimensional inclusion systems via sequential fractional derivatives. *Advances in Difference Equations*, **2021**(1), 449.
<https://doi.org/10.1186/s13662-021-03606-3>
- [20] Mohammadi H., Rezapour S., Etemad S., Baleanu D., 2020. Two sequential fractional hybrid differential inclusions. *Advances in Difference Equations*, **2020**(1), 385. <https://doi.org/10.1186/s13662-020-02850-3>
- [21] Khalil R., Al Horani M., Anderson D., 2016. Undetermined coefficients for local fractional differential equations. *Journal of Mathematics and Computer Science*, **16**(02), pp.140-146.
<https://doi.org/10.22436/jmcs.016.02.02>
- [22] Diethelm K., 2010. *The analysis of fractional differential equations: An application-oriented exposition using differential operators of Caputo type*. Springer-Verlag.
- [23] Gorenflo R., Kilbas A. A., Mainardi F., Rogosin S. V., 2014. *Mittag-leffler functions, related topics and applications* (1st ed. 2014). Springer Berlin Heidelberg : Imprint: Springer.
- [24] Prabhakar T. R., 1971. A singular integral equation with a generalized mittag leffler function in the kernel. *Yokohama Mathematical Journal*, **19**, pp.7-15.

- [25] Garra R., Garrappa R., 2018. The Prabhakar or three parameter Mittag–Leffler function: Theory and application. *Communications in Nonlinear Science and Numerical Simulation*, **56**, pp.314-329. <https://doi.org/10.1016/j.cnsns.2017.08.018>
- [26] Erman S., 2020. Solutions of linear fractional differential equations of order $n-1 < nq < n$. *Journal of Scientific Reports-A*, **0**(45), pp.81-89.



Chemical Characterization of Ultra High Molecular Weight Polyethylene Based Tibial Inserts After Ethylene Oxide Sterilization

Ogün BOZKAYA^{1,*} 

¹ Science and Engineering Laboratories, Scientific and Technological Researches Application and Research Center, Kırıkkale University, Kırıkkale, 71450, Turkey, **ORCID:** 0000-0001-8381-8649

Article Info

Research paper

Received : September 27, 2022

Accepted : December 20, 2022

Keywords

Chemical Characterization
Ethylene Oxide
ISO 10993-18
Tibial insert
UHMWPE

Abstract

Ultra-high molecular weight polyethylene (UHMWPE) has become the gold standard for total joint replacements such as tibial inserts because of its chemical inertness, superior mechanical properties, and biocompatibility. Ethylene oxide sterilization is one of the most common and effective methods used, especially for the sterilization of polyethylene-based polymeric implants. However, variable sterilization conditions can cause a change in the chemical structure of the polymeric material, which affects its mechanical properties and lifetime. The aim of this study is to investigate whether the chemical structure of UHMWPE tibial inserts sterilized with ethylene oxide undergoing certain conditions remains the same. Chemical characterization studies were performed with Fourier transform infrared spectroscopy, Raman spectroscopy, X-ray diffractometer, differential scanning calorimetry, thermogravimetric analysis, mass spectrometry and elemental analysis techniques recommended for polymeric materials in ISO 10993-8:2020 standard. According to the FTIR results, the spectra of the non-sterile and sterile tibial inserts were compared, and it was determined that the similarity between them was 99.97%. XRD results revealed that after ethylene oxide sterilization, there was no significant shift in the Bragg (1 0 0) peak. The percentages of crystallinity calculated from the fusion enthalpies determined by DSC of sterile and non-sterile samples are 54.3% and 53.3%, respectively. Characterization results revealed that there was no significant change in molecular structure, crystallinity, elemental composition of UHMWPE materials after ethylene oxide sterilization. These results can provide assurance that tibial inserts keep their physical, chemical, and mechanical properties after sterilization.

1. Introduction

Every year, millions of patients are implanted with medical devices to improve their quality of life and/or replace all or part of the biological structure or act as a part of it. Implantable medical devices continue to be one of the important research and development areas due to their potential applications in healthcare. Nowadays, bioimplants are being used in different parts of the body for diverse applications such as orthopedics (hips or knees), dentary, cardiovascular stents, neural prosthetics, pacemakers, defibrillators and drug delivery systems [1]. Implantable devices are biocompatible materials covering various material classes such as metallic, ceramic, and polymeric materials [2-4].

Polymeric biomaterials are used as a substitute or

adjunct to metal alloys in trauma and orthopedic implant devices due to their mechanical, chemical, thermal and biostable properties as well as their biocompatible nature [4].

For this reason, many absorbable and non-absorbable polymeric implants approved by the Food and Drug Administration (FDA) have been used in clinical practice for decades [5]. Polyglycolic acid, polylactic acid, polydioxanone, polyvinyl alcohol, polyglycolide-L-lactide, polyethylene oxide, polyethylene glycol and polycaprolactone are the most widely used absorbable synthetic polymers [6, 7]. This type of polymer is used in various fields of orthopedics and trauma surgery, especially as absorbable sutures, and screw pins [6]. Polyethylene terephthalate, polypropylene, poly(ether-ether-ketone), polyamide, polyvinyl chloride, polystyrene, polycarbonate,

* Corresponding Author: ogunbozkaya@kku.edu.tr



polyurethane, acrylonitrile butadiene styrene and polyethylene are non-absorbable polymers used in the manufacture of many medical devices such as surgical sutures, vascular grafts, spinal cages, stents, hernia mesh, artificial knee and hip joints [8-12].

Polymer biomaterials are chosen for biomedical applications based on various criteria including molecular weight, chemical structure, surface and mechanical properties, while their properties such as thermal (melting point, glass-transition temperature, etc.), solubility and degradation behaviors are primary considerations affecting the selection of scaffold production technique [13].

Synthetic polymers such as polylactic acid, polycaprolactone, poly(ether-ether-ketone) and polyethylene have become highly suitable biomaterials to meet bone tissue requirements due to their biocompatibility, robust mechanical properties and adaptability [14]. Among these polymers, polyethylene is a favorite material due to its low price, easy fabrication and forming process, availability, versatility, and widespread clinical success.

Polyethylene materials are light, flexible, biologically stable, chemically inert and resistant to many organic solvents at room temperature [15]. Because of its variable molecular weight, density and chain structure (branching), it has been categorized into five different types by the American Society for Testing and Materials (ASTM), each with different thermal, mechanical, chemical, electrical and optical properties: low-density polyethylene, linear low-density polyethylene, medium density polyethylene, cross-linked polyethylene, high-density polyethylene and ultra-high molecular weight polyethylene (UHMWPE) [16].

UHMWPE is an FDA-approved polymer that has been used as a medical device for decades. UHMWPE is widely used in orthopedic implants due to its excellent biocompatibility, extremely resistance to abrasion and corrosive chemicals, low wear volume, high tensile strength, low friction coefficient and high crystallinity [17, 18]. UHMWPE was first used in 1962 as joint replacement in total hip arthroplasty combined with a metal femoral head [16]. Today, it is widely used in hips, knees, shoulders, ankles, elbows, wrist joints as well as spinal discs [19]. All these joint replacements comprise at least two fragments articulating with one another. For example, a knee replacement has a metal femoral part, shaped to simulate the articular surface of a femur, and a tibial insert comprising mainly of UHMWPE with a metal backing socket (Figure 1) [20]. In this type of prosthesis, UHMWPE has a critical task, which is usually placed between metal components, both facilitating the movement of metals and preventing the direct transfer of load from metal to metal [7].

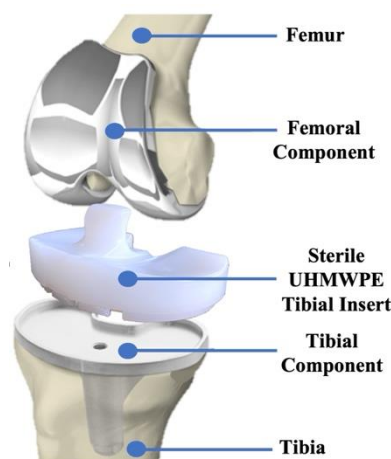


Figure 1. The components of a total knee replacement.

Medical devices can be classified as critical, semi-critical and non-critical according to the degree of infection risk in their use. Implants such as tibial inserts placed on the sterile part of the patient's body are critical devices with a high risk of infection [21]. Therefore, it is extremely important to sterilize the implant in a way that destroys all infecting microorganisms such as bacteria, viruses, fungi, yeasts and molds before the surgical operation [22]. There are many techniques used for sterilizing medical devices. Sterilization with autoclaving, dry heat, ozone gas, hydrogen peroxide vapor, low-temperature gas plasma, glutaraldehyde solution, peracetic acid, formaldehyde, microwave, gamma rays, ultraviolet light and ethylene oxide are some of them [21, 23]. Among these techniques, the most widely used sterilization technique for polymeric materials is ethylene oxide.

Ethylene oxide is an exceptional agent that is frequently used in the sterilization of medical devices due to its effective bactericidal, sporicidal and virucidal activity [24]. The antimicrobial effect of ethylene oxide is because of its inhibition of normal cellular metabolism and replication by causing cell wall, protein, DNA and RNA damage in the microorganism through chemical interactions [25]. The effectiveness of sterilization depends on the ethylene oxide concentration, temperature, humidity, exposure time to the gas and packaging material [26]. Moreover, these conditions can change the physico-chemical and mechanical properties of the polymeric implant, which negatively affects its performance in the body [27, 28]. For example, it has been reported that the strength of the polymer decreases according to the decrease in the molecular weight of the polymer under unsuitable sterilization conditions [29]. Changing the molecular weight impairs the mobility of the polymer chains, which causes the life, absorption, and mechanical properties of the polymer to change [25, 30]. Also, it has been reported in the literature that after sterilization, changes in the molecular properties

of bioabsorbable polymers considerably influence the biodegradation kinetics and the performance time [31, 32]. Hence, it is highly vital to detect the suitable sterilization methods and conditions for polymeric implants with various physical, chemical, and biological analyses. Medical device certification bodies also require medical device manufacturers to chemically compare the raw form of an FDA-approved material with the final product that has undergone shaping and sterilization processes.

In this study, comparative chemical characterization of the non-sterile and sterile versions of the tibial insert made of UHMWPE material was performed according to ISO 10993-18 (Biological evaluation of medical devices-Part 18: Chemical characterization of medical device materials within a risk management process). The aim of this study is to clarify whether there is a change in the chemical structure of medical devices produced from UHMWPE after being sterilized with ethylene oxide under the same conditions.

2. Materials and Methods

2.1 Materials

A commercial product, Total knee prosthesis tibial inserts (P/S, 70/15 mm, Hyperflex, UHMWPE) was obtained from a local medical device company (Ankara, Turkey).

2.2. Ethylene oxide sterilization procedure

The ethylene oxide sterilization process was carried out in a sterilization center according to ISO 11135 requirements. Briefly, the UHMWPE tibial inserts were preconditioned for 4 h at 50 ± 5 °C in 70–90% of relative humidity in a separate chamber. And then, the samples were in the ethylene oxide sterilization chamber. Throughout the sterilization (18 cycles), inside the sterilization chamber, preconditioning was through for 80 min at 50 ± 5 °C. Thenceforth, the samples were exposed to a gas mixture of 20% ethylene oxide and 80% carbon dioxide for 8 h. After sterilization, drying was done at 40 °C under a vacuum (1 torr) for 50 min (vacuum: 40 mins and nitrogen charging: 10 mins). Non-sterile and sterile UHMWPE tibial inserts are shown in Figure 2.

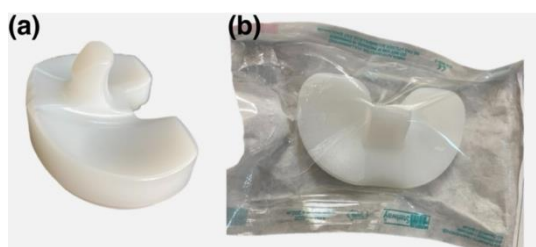


Figure 2. Non-sterile (a) and ethylene oxide sterilized (b) UHMWPE tibial inserts.

2.3. Chemical Characterization

2.3.1. Fourier transform infrared spectroscopy

Functional group analysis of the non-sterile and sterile tibial inserts was performed according to ASTM E1252 by FTIR spectroscopy (Bruker Vertex 70 V, USA). The percentage of similarity between the FTIR spectra of the materials was determined by the FTIR/OPUS software (4.2 Version, Copyright© Bruker Optics GmHb, USA).

2.3.2. Raman spectroscopy

Another functional group analysis was performed using a Bruker Senterra Raman instrument (laser wavelength: 532 nm, laser energy: 20 mW, duration: 60 sec, frequency: 50-4500 cm^{-1}).

2.3.3. X-ray diffraction

The phases structure of the sterile and non-sterile samples was analyzed using a X-ray diffraction (XRD, Empyrean, Malvern Panalytical) with 40 kV $\text{CuK}\alpha$ radiation ($\lambda = 1.54056$ Å). Samples were analyzed under the same scanning conditions ($2\theta = 10\text{--}80^\circ$, step size = 0.013° , scan rate = $2.0^\circ \text{min}^{-1}$). The d-spacing values of the samples were determined by Profex XRD software (Version 4.3.6), and the crystallite size values were determined by the Scherrer Equation [33].

2.3.4. Differential scanning calorimetry

Thermal properties of polymeric tibial inserts were analyzed by differential scanning calorimeter (DSC, Q 2000, TA Instruments, USA) with a heating rate of 10 °C min^{-1} , in a nitrogen gas atmosphere up to 400 °C, using an aluminum T-zero hermetic pan. Also, with DSC, the overall crystallinity (X_c , %) of polymers was calculated by the following equation:

$$X_c (\%) = \frac{\Delta H_f}{\Delta H_{100}} \times 100 \quad (1)$$

where ΔH_f is the heat of fusion and ΔH_{100} is the melting enthalpy of the 100% crystalline polymer.

2.3.5. Thermogravimetric analysis

The thermal degradation steps of the materials were analyzed with a thermogravimetric analyzer (TGA, Q 500, TA Instruments, USA) under certain conditions (nitrogen gas atmosphere, 10 °C min^{-1} heating rate, ceramic pan).

2.3.6. Mass spectrometer analysis

Mass spectrometer (MS) analyses of tibial inserts were performed on a Shimadzu QP 2010 GC-MS system using DI (direct injection) method over MS. The MS scan parameters included a mass scan range of 20–1090 m/z , an event time of 0.5 s, and a scan speed of 2500 $\mu m s^{-1}$. The ion source temperature was set to 350 °C with a heating rate of 10 °C min^{-1} .

2.3.7. Elemental analysis

Carbon (C), nitrogen (N), hydrogen (H) and sulfur (S) contents of the materials were determined with a CHNS elemental analyzer (vario MICRO cube, Elementar, Germany).

3. Results and Discussion

3.1. Functional group analysis

Depending on the ambient conditions (such as temperature, humidity, and exposure time) during the sterilization process, a chemical reaction may occur between the ethylene oxide gas and the polymeric material. This causes the physical and mechanical properties of the polymeric material to change. FTIR provides important information to determine the chemical bond changes of polymeric materials. Therefore, whether or not the chemical bond structure of the UHMWPE tibial inserts changed after sterilization was analyzed by FTIR (Figure 3). Since UHMWPE is a polyolefin type, the sharp absorption peaks at 2915 cm^{-1} and 2848 cm^{-1} are characteristic asymmetric and symmetric stretching vibration bands of CH_2 groups, respectively [15, 33]. Other clear peaks occurring at 1471 cm^{-1} and 722 cm^{-1} can be attributed to C-H vibration deformation and C-C rocking vibrations in the CH_2-CH_2 groups, respectively [34]. Meanwhile, UHMWPE sterilized with ethylene oxide is likely to be oxidized. Oxidation can be determined by looking at changes in 1720 cm^{-1} (carbonyl groups) [35, 36]. The absence of any absorption band at 1720 cm^{-1} is strong evidence that the material is not oxidized after ethylene oxide sterilization (Figure 3b). The spectra of

non-sterile and sterile tibial inserts were compared and the similarity between them was found to be 99.97%. According to the results of the FTIR, there was no change in the chemical bond structure of UHMWPE, which was sterilized with ethylene oxide under certain conditions.

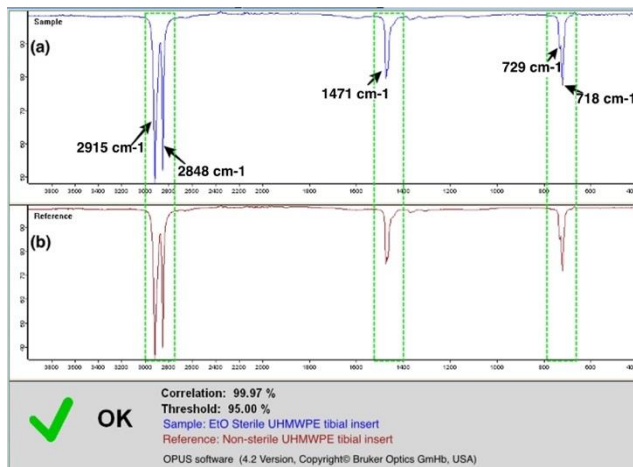


Figure 3. Comparison of the FTIR spectra of UHMWPE tibial inserts: (a) sterile, (b) non-sterile (scan speed: 32 cm^{-1} , resolution: 4 cm^{-1}).

3.2. Molecular structure analysis

Raman spectroscopy sensitively analyzes changes in the molecular structure level of polyethylene, such as the degree of crystallinity, which is a key factor in determining polyethylene density [37]. The change in the molecular structure and crystallinity of UHMWPE tibial inserts after sterilization was investigated by Raman (Figure 4). The peaks occurring in the region between 1150 cm^{-1} and 1500 cm^{-1} are attributed to the CH_2 groups in the crystalline and amorphous phases, respectively. The peaks between 1000 cm^{-1} and 1150 cm^{-1} are attributed to the symmetric and asymmetric C-C stretching vibrations [38, 39]. In addition, the sharp peaks seen at 2825 cm^{-1} and 2970 cm^{-1} belong to the stretching vibrations of the CH_2 groups [37]. When the Raman spectra of sterile and non-sterile tibial inserts are compared, it is seen that they are in harmony and there is no detectable difference.

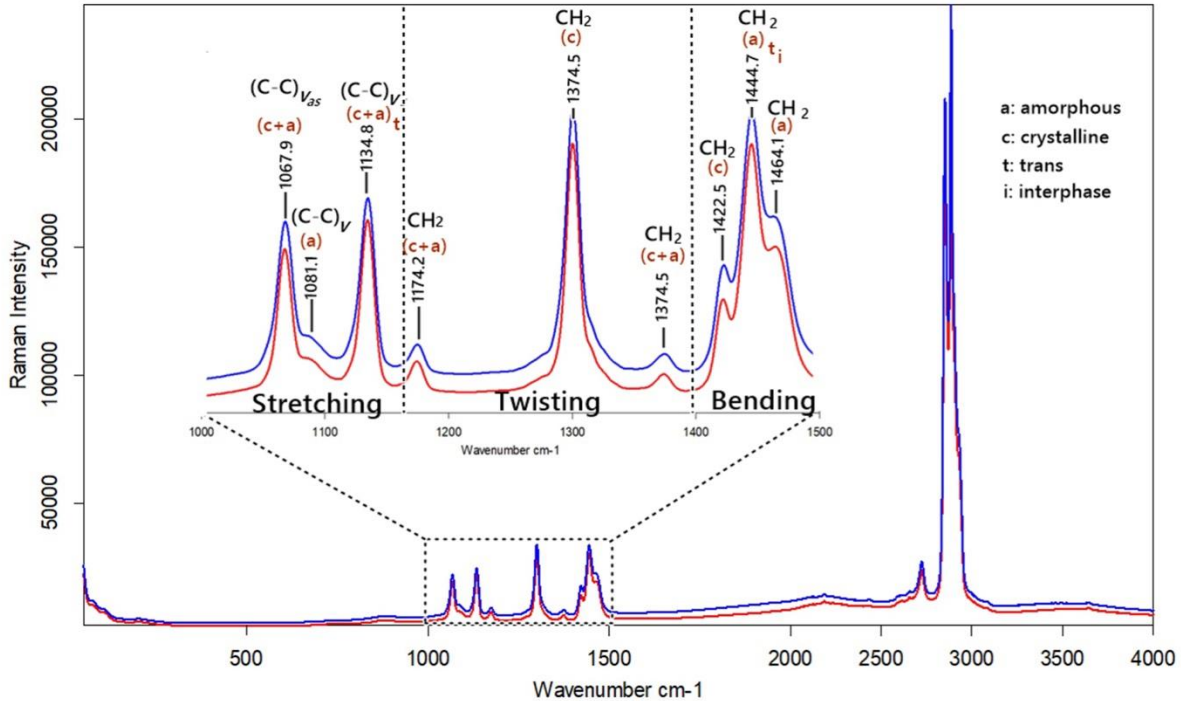


Figure 4. Raman spectra of sterile (blue) and non-sterile (red) UHMWPE tibial inserts.

3.3. Crystallinity and phase analysis

UHMWPE is a linear homopolymer whose chain curves show the local order in the form of crystalline lamella among amorphous matrixes [35]. Sterilization methods such as gamma-ray, ion beam, ultraviolet and ethylene oxide may change the crystallinity of the polymer by causing oxidative degradation, depending on the sterilization conditions [15, 35, 40]. It has been reported that the degree of crystallinity affects the mechanical properties of polymers such as Young's modulus, strength, fatigue, yield stress and shrinkage [41-43]. XRD was used to observe the variation in phase structure or crystallinity of sterile and non-sterile materials, and the diffractograms are shown in Figure 5. The peaks at angles 2θ of 21.49° , 23.91° and 29.71° match the (1 1 0), (2 0 0) and (0 2 0) orthorhombic lattice planes of the semi-crystalline UHMWPE, respectively [33, 43, 44]. The 2θ , d-spacing and crystallite size values corresponding to the (1 1 0) and (2 0 0) planes of sterile and non-sterile materials were shown in Table 1. The d-spacing and crystallite size values of UHMWPE tibial inserts are almost the same after sterilization. In addition, there was no remarkable shift in the Bragg (110) peak, which demonstrates that there is no change in the inter-planar spacing [35].

Table 1. 2θ , d-spacing and crystallite size values of non-sterile and sterile UHMWPE tibial inserts.

Sample	2θ [°]	d-spacing [Å]	Crystallite Size [nm]
Non-sterile	21.49	4.133	36.70
	23.91	3.716	33.91
Sterile	21.42	4.144	37.70
	23.87	3.725	33.90

3.4. Comparison of thermal properties

Besides the thermal properties of polymers such as glass transition (T_g) temperature, melting temperature (T_m), oxidation temperature and crystallization temperature (T_c), DSC was used to analyze whether decomposition is endothermic or exothermic. Moreover, the crystallinity degree (%) of thermoplastic polymers can be calculated by the enthalpy (heat) of fusion related to the melting transition of the polymer. Crystallinity is ascertained by normalizing the observed heat of fusion to that of a 100% crystalline sample of the same polymer. In the DSC thermograms shown in Figure 6, the melting temperatures of sterile and nonsterile UHMWPE tibial inserts were determined as 142.05°C and 142.30°C , and the heats of fusion were 159.1 J g^{-1} and 156.3 J g^{-1} , respectively.

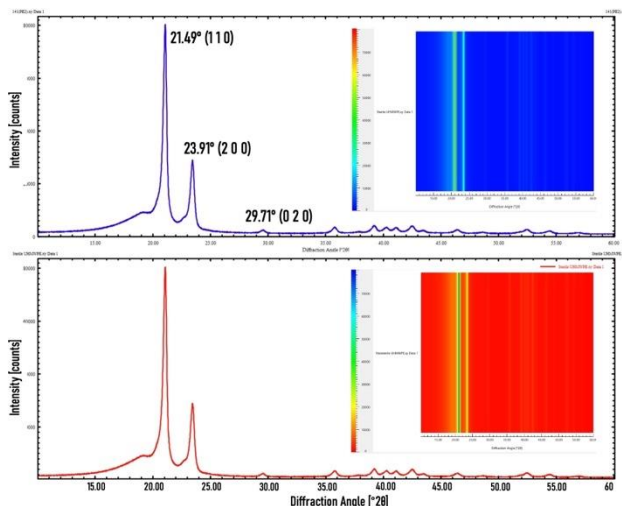


Figure 5. X-ray diffraction patterns of the sterile (blue) and non-sterile (red) UHMWPE tibial inserts.

The enthalpy of fusion for 100% crystalline polyethylene is 293 J g^{-1} [43, 45]. The percentages of crystallinity of sterile and nonsterile samples were calculated as 54.3% and 53.3%, respectively. There was no considerable change in the melting point and crystalline degree of the UHMWPE tibial insert after the ethylene oxide sterilization. Therefore, it can be said that the ethylene oxide sterilization temperature ($50 \text{ }^\circ\text{C}$) and the exposure time (8 h) at this temperature do not cause any chemical and physical changes in the chain structure of UHMWPE. We could not find a comparison study after ethylene oxide sterilization in the literature; however, there are studies examining the effect of gamma-ray sterilization conditions on the melting temperatures and crystalline degrees of UHMWPE with DSC [46, 47].

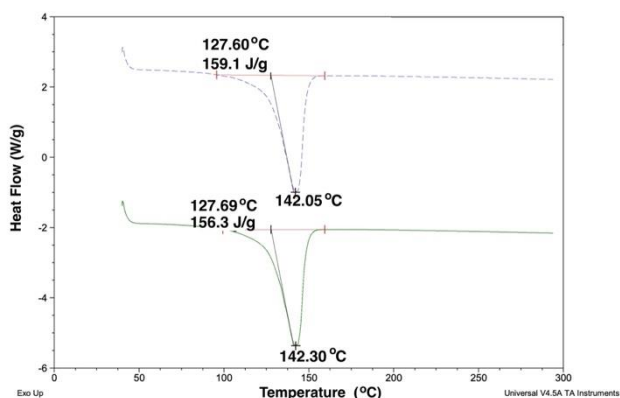


Figure 6. DSC thermograms of sterile (green) and nonsterile (blue) UHMWPE tibial inserts.

3.5. Comparison of thermal stabilities

During the ethylene oxide sterilization process, the polymeric material is exposed to temperature, humidity, pressure, and chemical gas. For this reason, some physical and chemical changes may occur in the structure of the polymer, which also affects its thermal stability. TGA is a thermal analysis method that determines mass changes as a function of time and temperature [43, 44]. The thermal stability of sterile and non-sterile UHMWPE tibial inserts was investigated by TGA (Figure 7). Nonsterile UHMWPE is thermally stable up to $450 \text{ }^\circ\text{C}$ and exhibited a single-step decomposition at subsequent temperatures with a maximum decomposition temperature of $523.6 \text{ }^\circ\text{C}$. The results agree with the literature [43, 48, 49]. After ethylene oxide sterilization, no mass loss of any evaporating or volatile components was observed up to $450 \text{ }^\circ\text{C}$. In addition, there is no significant change in the maximum decomposition temperature ($524.16 \text{ }^\circ\text{C}$). The residual masses of sterile and non-sterile tibial inserts at the end of $600 \text{ }^\circ\text{C}$ were determined as 0.35% and 0.36%, respectively. As a result, no physical and chemical changes were detected, that would affect the thermal stability of the materials after the sterilization process.

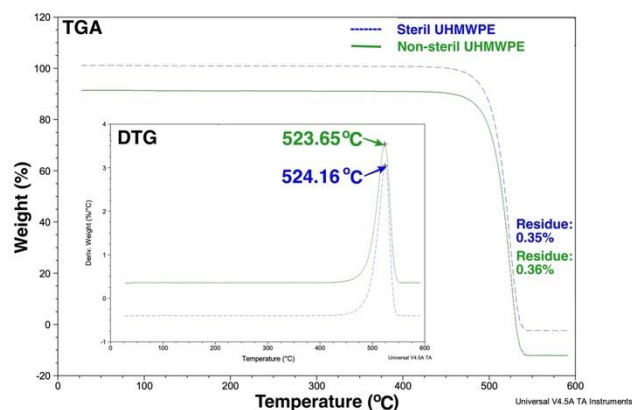


Figure 7. TGA and D-TGA curves of sterile and nonsterile UHMWPE tibial inserts.

3.6. Mass spectrometer results

MS is an important technique used to identify and characterize the degradation products of polymeric materials [50]. MS was also used to determine if the chemical structure of the UHMWPE tibial inserts changed after the ethylene oxide sterilization. Polyethylene is a very high molecular weight hydrocarbon, and its degradation products are normal hydrocarbons such as oligomers. Among these hydrocarbons, there may be alkadienes, alkenes and alkane groups such as long-chain dodecadiene, dodecene and dodecane [51]. With the change of the

molecular structure of the polymer after the sterilization process, the ionized decomposition products also partially change. The mass spectrum of the degradation products was compared according to the mass/charge (m/z) ratio of polyethylene, and it was determined that the degradation products of the tibial inserts were almost the same (Figure 8). Therefore, this high similarity can be attributed to both

the preservation of the chemical structure and the absence of ethylene oxide residue after sterilization. Meanwhile, the ethylene oxide residue is analyzed according to the methods and conditions specified in ISO 10993-7 (Biological evaluation of medical devices — Part 7: Ethylene oxide sterilization residuals) [25, 52].

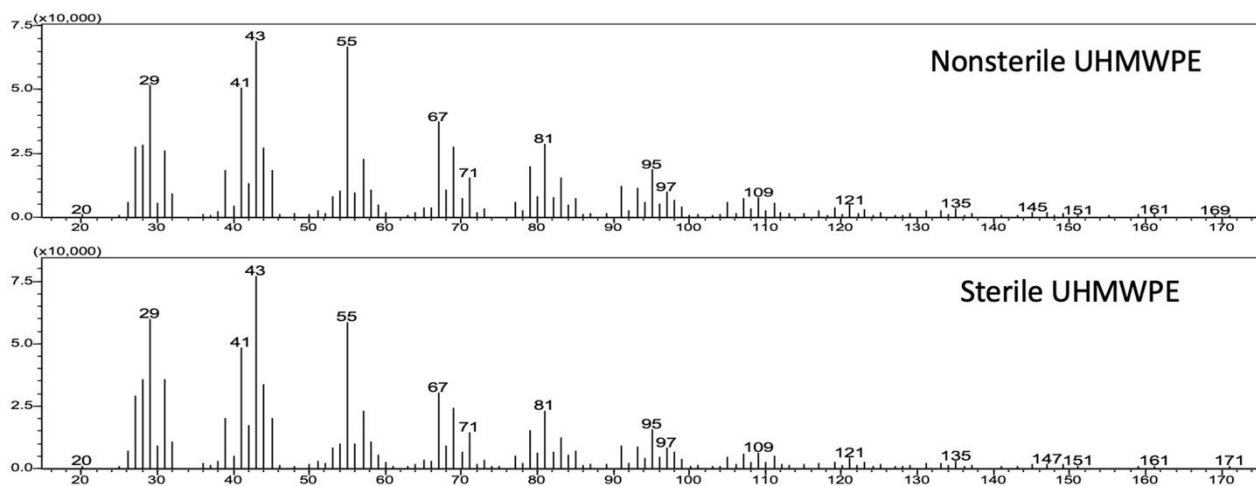


Figure 8. Mass spectra of sterile and nonsterile UHMWPE tibial inserts.

3.7. CHNS elemental analyses results

Elemental analysis is an extensively used technique to measure the amount of carbon (C), hydrogen (H), nitrogen (N), sulfur (S), and oxygen (O) in the structure of many materials [53]. The theoretical C and H content of polyethylene, whose repeating unit has the chemical formula $-(C_2H_4)_n-$ (n : degree of polymerization) is 85.63% and 14.26%, respectively [54]. During the ethylene oxide sterilization, the carbon, hydrogen, nitrogen, sulfur, and oxygen contents of the polymeric material may change when exposed to temperature, ethylene oxide, carbon dioxide, nitrogen gases, humidity (H_2O) and air. Therefore, C, H, N and S contents of sterile and nonsterile tibial inserts were determined by CHNS/O elemental analysis (Table 2). The average carbon and hydrogen content of the nonsterile material were determined as $85.61\% \pm 0.3\%$ and $13.95\% \pm 0.007\%$, respectively. The carbon and hydrogen contents of the sterile tibial insert were determined as $85.61\% \pm 0.3\%$ and $14.062\% \pm 0.064\%$, respectively. Although there does not seem to be a significant difference in the carbon and hydrogen contents after sterilization, these minor changes may be due to a residue. The residue may be caused by ethylene oxide or other contaminants, but it is very important to analyze ethylene oxide residue after sterilization, especially since ethylene oxide gas is very toxic and carcinogenic [25].

Table 2. Carbon, Hydrogen, Nitrogen and Sulfur contents of non-sterile and sterile UHMWPE tibial inserts.

Sample	C [%]	H [%]	N [%]	S [%]
Non-sterile	85.58	13.978	0.00	0.00
Non-sterile	85.63	13.991	0.00	0.00
Non-sterile	85.63	13.986	0.00	0.00
Mean Value	85.61	13.985	0.00	0.00
Deviation	0.03	0.007	0.00	0.00
Sterile	85.71	13.989	0.00	0.00
Sterile	85.65	14.101	0.00	0.00
Sterile	85.67	14.097	0.00	0.00
Mean Value	85.68	14.062	0.00	0.00
Deviation	0.03	0.064	0.00	0.00

4. Conclusions

In the last decade, there has been a tremendous increase in the number of implantable medical devices based on UHMWPE, especially as part of joint prostheses. There is no single standard method recommended by the FDA for the sterilization of polymeric implants. Manufacturers must optimize the sterilization conditions according to the type of polymer used, molecular weight (such as LDPE, HDPE, UHMWPE), and shape and size of the device. Ethylene oxide is one of the most widely used and safe methods for the sterilization of UHMWPE

materials. However, depending on the sterilization conditions, the physical, chemical, and mechanical properties of the polymer material may be affected, which is of vital importance, especially for polymeric implants used in knee prostheses. In the present study, it was investigated by various instrumental techniques if there was a change in the chemical structure of UHMWPE tibial inserts after sterilization. The agreement between the FT-IR spectra of the non-sterile and sterile samples was 99.97%. The high agreement between both FT-IR and RAMAN spectra revealed that there was no significant change in the chemical bond structure of the materials after sterilization. The percentages of crystallinity of sterile and non-sterile samples were calculated by DSC as 54.3% and 53.3%, respectively. The agreement between the XRD results also supports the DSC results. These results support that the polymer chains have not undergone a change that would affect the mechanical properties of the material. Therefore, in this study, it has been proven that there is no significant change in the chemical structure of tibial inserts after ethylene oxide sterilization.

Ethylene oxide is thus a viable method for sterilization of UHMWPE tibial inserts. However, the chemical structure and mechanical integrity of UHMWPE materials may deteriorate when exposed to very high doses.

Declaration of Ethical Standards

The author of this article declares that the materials and methods used in this study do not require ethical committee permission and/or legal-special permission.

Conflict of Interest

The author declares that he has no competing financial interests or personal relationships that could have appeared to influence the work reported in this paper.

Acknowledgements

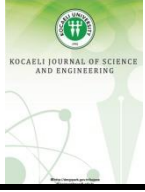
The author would like to thank Kırıkkale University Scientific and Technological Researches Application and Research Center (KUBTUAM).

References

- [1] Park G. E., Webster T. J., 2005. A review of nanotechnology for the development of better orthopedic implants. *Journal of Biomedical Nanotechnology*, **1**, 18-29.
- [2] Prakasam M., Locs J., Salma-Ancane K., Loca D., Largeteau A., Berzina-Cimdina L., 2017. Biodegradable materials and metallic implants—a review. *Journal of functional biomaterials*, **8**, 44.
- [3] Kulkarni S. V., Nemade A. C., Sonawwanay P. D., *Recent Advances in Manufacturing Processes and Systems*, Springer Singapore, **2022**.
- [4] Yin J., Luan S., 2016. Opportunities and challenges for the development of polymer-based biomaterials and medical devices. *Regenerative biomaterials*, **3**, 129-135.
- [5] Kohn J., Welsh W. J., Knight D., 2007. A new approach to the rationale discovery of polymeric biomaterials. *Biomaterials*, **28**, 4171-4177.
- [6] Youssef A., Hollister S. J., Dalton P. D., 2017. Additive manufacturing of polymer melts for implantable medical devices and scaffolds. *Biofabrication*, **9**, 012002.
- [7] Ulery B. D., Nair L. S., Laurencin C. T., 2011. Biomedical applications of biodegradable polymers. *Journal of Polymer Science Part B: Polymer Physics*, **49**, 832-864.
- [8] Abruzzo A., Fiorica C., Palumbo V. D., Altomare R., Damiano G., Gioviale M. C., Tomasello G., Licciardi M., Palumbo F. S., Giammona G., 2014. Using polymeric scaffolds for vascular tissue engineering. *International Journal of Polymer Science*, **2014**.
- [9] Ravi S., Chaikof E. L., 2010. Biomaterials for vascular tissue engineering. *Regenerative Medicine*, **5**, 107-120.
- [10] Kurtz S. M., Devine J. N., 2007. PEEK biomaterials in trauma, orthopedic, and spinal implants. *Biomaterials*, **28**, 4845-4869.
- [11] Muratoglu O. K., O'Connor D. O., Bragdon C. R., Delaney J., Jasty M., Harris W. H., Merrill E., Venugopalan P., 2002. Gradient crosslinking of UHMWPE using irradiation in molten state for total joint arthroplasty. *Biomaterials*, **23**, 717-724.
- [12] Joseph B., James J., Kalarikkal N., Thomas S., 2021. Recycling of medical plastics. *Advanced Industrial and Engineering Polymer Research*, **4**, 199-208.
- [13] Dhandayuthapani B., Yoshida Y., Maekawa T., Kumar D. S., 2011. Polymeric scaffolds in tissue engineering application: a review. *International Journal of Polymer Science*, **2011**.
- [14] Puppi D., Chiellini F., Piras A. M., Chiellini E., 2010. Polymeric materials for bone and cartilage repair. *Progress in Polymer Science*, **35**, 403-440.

- [15] Doğan M., 2021. Ultraviolet light accelerates the degradation of polyethylene plastics. *Microscopy Research and Technique*, **84**, 2774-2783.
- [16] Paxton N. C., Allenby M. C., Lewis P. M., Woodruff M. A., 2019. Biomedical applications of polyethylene. *European Polymer Journal*, **118**, 412-428.
- [17] Bombać D., Brojan M., Fajfar P., Kosel F., Turk R., 2007. Review of materials in medical applications Pregled materialov v medicinskih aplikacijah. *RMZ–Materials and Geoenvironment*, **54**, 471-499.
- [18] McKeen L. W. in *Plastics used in medical devices, Vol.*, Elsevier, **2014**, pp.21-53.
- [19] Patil N. A., Njuguna J., Kandasubramanian B., 2020. UHMWPE for biomedical applications: Performance and functionalization. *European Polymer Journal*, **125**, 109529.
- [20] Cobelli N., Scharf B., Crisi G. M., Hardin J., Santambrogio L., 2011. Mediators of the inflammatory response to joint replacement devices. *Nature Reviews Rheumatology*, **7**, 600-608.
- [21] Govindaraj S., Muthuraman M. S., 2015. Systematic review on sterilization methods of implants and medical devices. *Int J ChemTech Res*, **8**, 897-911.
- [22] Rutala W., Weber D., 1999. Infection control: the role of disinfection and sterilization. *Journal of Hospital Infection*, **43**, S43-S55.
- [23] Tipnis N. P., Burgess D. J., 2018. Sterilization of implantable polymer-based medical devices: A review. *International Journal of Pharmaceutics*, **544**, 455-460.
- [24] Ries M. D., Weaver K., Beals N., 1996. Safety and Efficacy of Ethylene Oxide Sterilized Polyethylene in Total Knee Arthroplasty. *Clinical Orthopaedics and Related Research*, **331**, 159-163.
- [25] Mendes G. C. C., Brandão T. R. S., Silva C. L. M., 2007. Ethylene oxide sterilization of medical devices: A review. *American Journal of Infection Control*, **35**, 574-581.
- [26] Mosley G. A., Gillis J. R., Whitbourne J. E., 2002. Calculating equivalent time for use in determining the lethality of EtO sterilization processes. *Medical Device and Diagnostic Industry*, **24**, 54-63.
- [27] Heider D., Gomann J., Junghann B., Kaiser U., 2002. Kill kinetics study of *Bacillus subtilis* spores in ethylene oxide sterilisation processes. *Zentr Steril*, **10**, 158-167.
- [28] Düzyer S., Hockenberger A., Agah U., Elif E., Kahveci Z. Etilen oksit, otoklav ve ultra viyole sterilizasyonlarının PET elektroçekim liflerin yüzey topografisi üzerine etkisi. *Uludağ University Journal of The Faculty of Engineering*, **21**, 201-218.
- [29] Farrar D., Gillson R., 2002. Hydrolytic degradation of polyglyconate B: the relationship between degradation time, strength and molecular weight. *Biomaterials*, **23**, 3905-3912.
- [30] Saeidlou S., Huneault M. A., Li, H., Park, C. B., 2012. Poly (lactic acid) crystallization. *Progress in Polymer Science*, **37**, 1657-1677.
- [31] Valente T., Silva D., Gomes P., Fernandes M., Santos J., Sencadas V., 2016. Effect of sterilization methods on electrospun poly (lactic acid)(PLA) fiber alignment for biomedical applications. *ACS applied materials & interfaces*, **8**, 3241-3249.
- [32] Pietrzak W. S., 2010. Effects of ethylene oxide sterilization on 82: 18 PLLA/PGA copolymer craniofacial fixation plates. *Journal of Craniofacial Surgery*, **21**, 177-181.
- [33] Mindivan F., Çolak A., 2021. Tribo-material based on a UHMWPE/RGOC biocomposite for using in artificial joints. *Journal of Applied Polymer Science*, **138**, 50768.
- [34] Naresh Kumar N., Yap S. L., Bt Samsudin F. N. D., Khan M. Z., Pattela Srinivasa R. S., 2016. Effect of Argon Plasma Treatment on Tribological Properties of UHMWPE/MWCNT Nanocomposites. *Polymers*, **8**, 295.
- [35] Stojilovic N., Dordevic S. V., Stojadinovic S., 2017. Effects of clinical X-ray irradiation on UHMWPE films. *Nuclear Instruments and Methods in Physics Research Section B: Beam Interactions with Materials and Atoms*, **410**, 139-143.
- [36] Wang H., Xu L., Hu J., Wang M., Wu G., 2015. Radiation-induced oxidation of ultra-high molecular weight polyethylene (UHMWPE) powder by gamma rays and electron beams: A clear dependence of dose rate. *Radiation Physics and Chemistry*, **115**, 88-96.
- [37] Ibrahim M., He H., 2017. Classification of polyethylene by Raman spectroscopy. *Application Note AN52301*, Thermo Fisher Scientific.
- [38] Fischer J., Wallner G. M., Pieber A., 2008. Spectroscopical investigation of ski base materials, **265**, 28-36.
- [39] Sato H., Shimoyama M., Kamiya T., Amari T., Šaić S., Ninomiya T., Siesler H. W., Ozaki Y., 2002. Raman spectra of high-density, low-density, and linear low-density polyethylene pellets and prediction of their

- physical properties by multivariate data analysis. *Journal of Applied Polymer Science*, **86**, 443-448.
- [40] Toth S., Füle M., Veres M., Pocsik I., Koos M., Tóth A., Ujvari T., Bertóti I., 2006. Photoluminescence of ultra-high molecular weight polyethylene modified by fast atom bombardment. *Thin Solid Films*, **497**, 279-283.
- [41] Bourell D. L., Watt T. J., Leigh D. K., Fulcher B., 2014. Performance limitations in polymer laser sintering. *Physics Procedia*, **56**, 147-156.
- [42] Hopkinson N., Majewski C., Zarringhalam H., 2009. Quantifying the degree of particle melt in Selective Laser Sintering®. *CIRP annals*, **58**, 197-200.
- [43] Khalil Y., Hopkinson N., Kowalski A., Fairclough, J. P. A., 2019. Characterisation of UHMWPE polymer powder for laser sintering. *Materials*, **12**, 3496.
- [44] Bozkaya O., Arat E., Gök Z. G., Yiğitoğlu M., Vargel İ., 2022. Production and characterization of hybrid nanofiber wound dressing containing *Centella asiatica* coated silver nanoparticles by mutual electrospinning method. *European Polymer Journal*, **166**, 111023.
- [45] Turell M. B., Bellare A., 2004. A study of the nanostructure and tensile properties of ultra-high molecular weight polyethylene. *Biomaterials*, **25**, 3389-3398.
- [46] Stephens C. P., Benson R. S., Esther Martinez-Pardo M., Barker E. D., Walker J. B., Stephens T. P., 2005. The effect of dose rate on the crystalline lamellar thickness distribution in gamma-radiation of UHMWPE. *Nuclear Instruments and Methods in Physics Research Section B: Beam Interactions with Materials and Atoms*, **236**, 540-545.
- [47] Slouf M., Synkova H., Baldrian J., Marek A., Kovarova J., Schmidt P., Dorschner H., Stephan M., Gohs U., 2008. Structural changes of UHMWPE after e-beam irradiation and thermal treatment. *Journal of Biomedical Materials Research Part B: Applied Biomaterials*, **85B**, 240-251.
- [48] Souri H., Bhattacharyya D., 2018. Electrical conductivity of the graphene nanoplatelets coated natural and synthetic fibres using electrophoretic deposition technique. *International Journal of Smart and Nano Materials*, **9**, 167-183.
- [49] Santos C. M. d., Silva B. C. d., Backes E. H., Montagna L. S., Pessan L. A., Passador F. R., 2018. Effect of LLDPE on aging resistance and thermal, mechanical, morphological properties of UHMWPE/LLDPE blends. *Materials Research*, **21**.
- [50] Rial-Otero R., Galesio M., Capelo J.-L., Simal-Gándara J., 2009. A Review of Synthetic Polymer Characterization by Pyrolysis-GC-MS. *Chromatographia*, **70**, 339-348.
- [51] Wang F. C.-Y., 2004. The microstructure exploration of thermoplastic copolymers by pyrolysis-gas chromatography. *Journal of Analytical and Applied Pyrolysis*, **71**, 83-106.
- [52] Gimeno P., Auguste M.-L., Handlos V., Nielsen A. M., Schmidt S., Lassu N., Vogel M., Fischer A., Brenier C., Duperray F., 2018. Identification and quantification of ethylene oxide in sterilized medical devices using multiple headspace GC/MS measurement. *Journal of Pharmaceutical and Biomedical Analysis*, **158**, 119-127.
- [53] Nizamuddin S., Jamal M., Gravina R., Giustozzi F., 2020. Recycled plastic as bitumen modifier: The role of recycled linear low-density polyethylene in the modification of physical, chemical and rheological properties of bitumen. *Journal of Cleaner Production*, **266**, 121988.
- [54] Sherazi T. A. in *Ultrahigh Molecular Weight Polyethylene, Vol.* (Eds.: E. Drioli, L. Giorno), Springer Berlin Heidelberg, Berlin, Heidelberg, **2015**, pp.1-2.



Investigation of The Effect of Knitting Row on Vibration Structure for A Wide Chimney Made With Brick Bar

Mustafa Murat YAVUZ¹ , Nurbanu ERDAL^{2,*} 

¹ Department of Mechanical Engineering, İzmir Democracy University, İzmir, Turkey, **ORCID:** 0000-0002-5892-0075

² Department of Mechanical Engineering, İzmir Democracy University, İzmir, Turkey, **ORCID:** 0000-0003-0655-4314

Article Info

Research paper

Received : April 26, 2022

Accepted : July 23, 2022

Keywords

Brick
Chimney
Vibration
Stress

Abstract

Building systems have unique structural behaviour. In addition to the obvious material properties used in the formation of this behaviour, the geometric shape is also of great importance. In this study, the mechanical effects on the chimney-shaped structure built with bar bricks for product storage were investigated under compression and vibration conditions. Finite element analysis was used as a research method. Solid bar bricks and cement with standard specifications were used as the intermediate filling material for the construction system, which was formed in a wide circular array and short knitting height. Considering the ideal behaviour of the materials, a fully elastic solution was made. As a result of the examination, the effect of the knitting order on the natural frequency was found to be low, as the reason for this, it was seen that the geometric structure exhibited a very tough behaviour against deformation. The stress concentration was observed at the fillings between the bricks laid in the same layer. The dimensionless deformation at natural frequencies was 1.4 times the diameter of the chimney. The knitting order affected stress values and symmetrical distribution formed in the brick. The results were discussed over the findings.

1. Introduction

Bricks, briquettes, and stone blocks occur at the base of the building system used to create a closed zone. By combining these building elements at the desired level, a single large structure is created. The mechanical behaviour of the created structure is unique to itself and mostly depends on the material, the geometry and applied boundary conditions. In these structures, which have been used for a long time, different types of materials, joining arrangements, and spacer-filling materials have been used over time, and development studies are continuing. The behaviour of chimney brick structures has been studied in the literature for various loading conditions. Harvest warehouses (one of the chimney brick structures) [1], where agricultural products are stored, especially in farm regions, are made of metallic or brick structures and have a service life of 30 to 40 years. The warehouses [1-2] with a height-width ratio of around 3 can be shorter or longer. Most of the warehouses [3] are open-topped structures. For

the self-protection of the structure, mechanical loading conditions and mechanical characteristics are examined and some cases are emphasized. Pande et al. [4] investigated the behaviour of brick and cement mortar under axial loading at different elastic modulus for knitted walls and expressed the results according to the equivalent material approach. The cement mortar used exhibited homogeneous orthorhombic elastic material behaviour. Magenes and Calvi [5] investigated the strength, deformation, and strain energy behaviour of a knitting wall under seismic conditions and developed simplified strength formulas obtained from some experimental and numerical results. They stated that the shear formations have dominated the collapse of the knitting walls in dynamic loading, and as a result, they defined a new equation for the slip that caused a fracture. Kaushik et al. [6] investigated the stress-strain behaviour by conducting axial compression tests for a wall built with solid clay bricks and mortar. They gained a non-linear stress-strain diagram, and six important control points were marked in that chart. Anthoine et al. [7] investigated the seismic behaviour for knitting walls experimentally and numerically and

* Corresponding Author: nurbanu.erdal@idu.edu.tr



determined that the height/width ratio and vertical stress affect the seismic behaviour. Valluzzi et al. [8] defined three different problems in the masonry wall where they use fiber reinforcements: crushing the wall, separating the fibers and breaking the mortar by the slide along the joint. They have seen that the bond between the fiber plates and the wall was effective in strength and the used fiber reinforcement increased the strength and ductility. Priestley and Bridgeman [9] used reinforcement panels to prevent the collapse of knitting walls in seismic conditions and found that properly positioned horizontal steels suppressed all shear loads and increased the strength. Alforno et al. [10] observed different structural stiffness and reaction forces according to different brick patterns in the numerical analyses of masonry vaults. Srinithya et al. [11] conducted a wall-strengthening study focused on static and free vibration analysis. They investigated the effect of parametric properties with the finite element

method and found that the toughness value increased by %43 and the deformation value decreased by %30.

Due to the limited number of studies in the literature and the lack of a detailed description of the physical properties of the chimney mesh structure, static and vibration analyzes were carried out for the brick masonry formed in the chimney structure.

2. Numerical Model

A basic model was created to examine the chimney structure formed by brickwork. The geometric structure was shown in Fig. 1. Using the chimney geometry in Fig. 1, the finite element model was created and examined. The brick chimney layers were stacked ten floors on top of each other. The angle of placement in the overlapping of chimney brick layers was expressed as (α°). The chimney structures prepared for different α values were shown in Fig. 2.

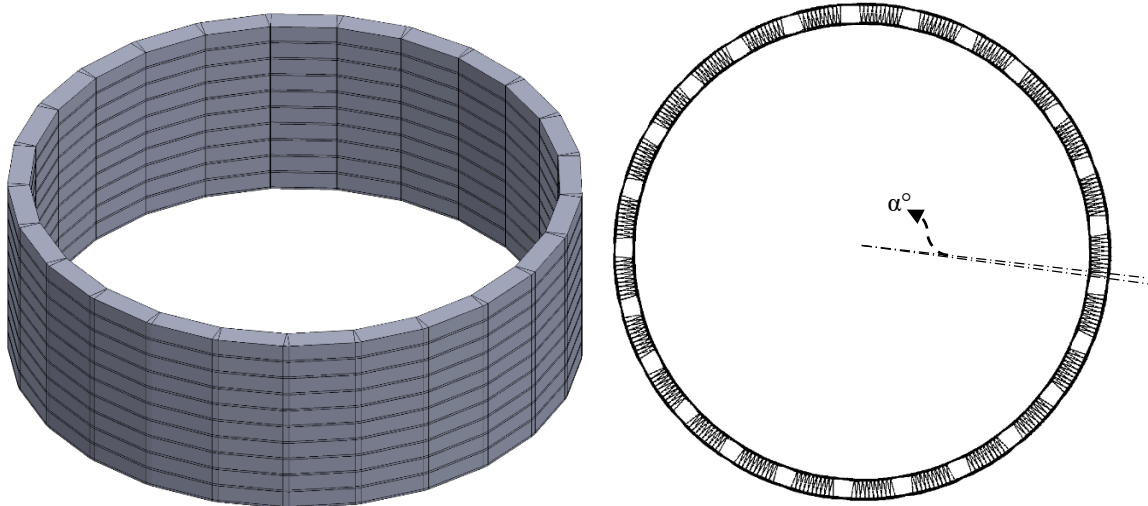


Figure 1. Isometric view of a flat knit brick chimney and a top view showing the different knitting order (α°).

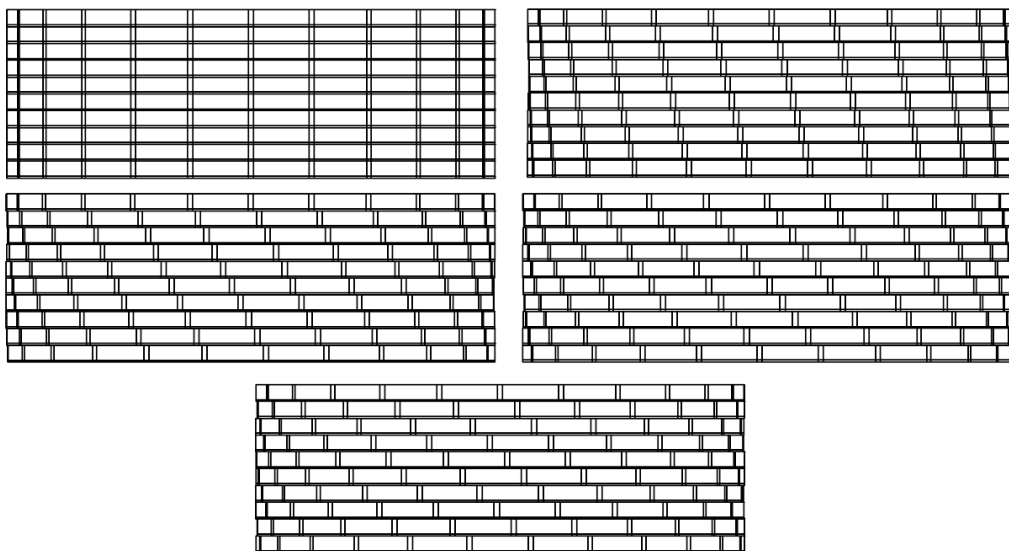


Figure 2. Different knitting rows of brick chimney layers.

Each brick has a length of 150 mm, a width of 50 mm, and a height of 40 mm. A chimney layer was formed using 25 bricks on a circular path having a radius of 625 mm. In the formation of the brick chimney, cement mortar was added between the bricks in the chimney layer and between the layers. Cement mortar of 5 mm thickness was used between layers and all mortar structures were bonded in contact definition. Brick material has a density of 1730 kg/m³, Young's Modulus of 3.865 GPa, and Poisson's ratio of 0.094. Cement mortar has a density of 2300 kg/m³, Young's Modulus of 30 GPa, and Poisson's ratio of 0.18. The gravity effect was neglected because the structure included a low aspect ratio. For the investigations, fixed boundary conditions were applied at the bottom surface of all chimney models. The first six modes were analysed for the modal analysis. The static stress analyses were applied with applying 1 MPa compression pressure to the upper surface of the chimney models. Linear elastic material behavior [12] was used in the analyses as similar to concrete silo analyses in the literature. According to defined linear elastic isotropic material properties, the stresses were given as Von-Mises stresses. The used Von-Mises stress was expressed in Eq. 1. The stresses on the right-hand side of the equation were the principal stresses. In Eq. 2, the general equation of motion was expressed.

$$\sigma_{VM} = \sqrt{\frac{(\sigma_1 - \sigma_2)^2 + (\sigma_2 - \sigma_3)^2 + (\sigma_3 - \sigma_1)^2}{2}} \quad (1)$$

$$[M]\{\ddot{u}\} + [C]\{\dot{u}\} + [K]\{u\} = \{f(t)\} \quad (2)$$

It is expressed as $[M]$ =mass, $[C]$ =damping, $[K]$ =stiffness, $\{\ddot{u}\}$ =acceleration, $\{\dot{u}\}$ =velocity, $\{u\}$ =displacement, $f(t)$ =load in the equation. Loading was not given in the modal analysis and therefore $f(t)=0$. The common properties of concrete [13] include low energy loss factor and damping coefficient in harmonic motion. Since it is [14] not reinforced with any damping effect enhancing mortar, its damping effect has been neglected; $[C]=0$. Thus, the vibration energy in the system returns from boundary conditions without any loss (heat or etc.). As a result the above equation for modal analysis;

$$[M]\{\ddot{u}\} + [K]\{u\} = 0 \quad (3)$$

It was assumed that each finite element made harmonic motion in the solution of the equation.

3. Result and Discussion

For the finite element model to be used, first of all, the effect of the number of finite elements on the results

was investigated. Although absolute deformation definition and results were not important in modal analysis, it was used to show the effect of the number of elements and the results are shown in Fig. 3. As the number of elements reached a certain number, a stable deformation value was observed in the results. Approximately 35,000 finite elements were used in the study. In the stable results given by the finite elements created, the aspect ratio of the finite elements approached one. The average aspect ratio of the elements was 1.25.

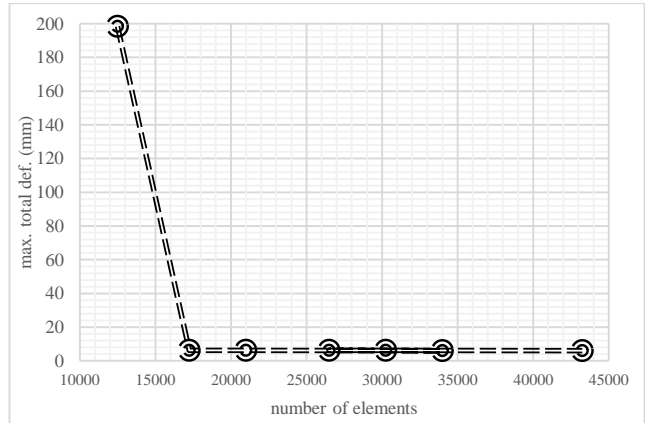


Figure 3. According to the number of elements used variation of the maximum total deformation resulting from mode 1 for $\alpha=0^\circ$

The natural frequencies of the chimney models of different knitting orders were given in Table 1. Due to the geometric structure of the system and the materials used, it was observed that the frequency difference between the modes was low.

Table 1. Natural frequencies (Hz) occurring at different α values

	$\alpha=0^\circ$	$\alpha=1^\circ$	$\alpha=2^\circ$	$\alpha=3^\circ$	$\alpha=4^\circ$
mod I	250.8	250.9	248.7	259.6	247.3
mod II	252.1	251.0	249.0	259.9	247.6
mod III	280.8	280.5	278.7	282.1	277.3
mod IV	281.3	280.5	278.9	282.6	277.4
mod V	291.3	292.5	290.8	302.3	290.0
mod VI	293.1	292.6	291.3	318.0	290.6

Natural frequencies and deformed shape of the brick chimney for different modes were shown in Fig. 4. As the geometry of the object has a short length and a large base size, bending and accordingly tension-compression situations have occurred rather than torsion. Modes were formed in ordered pairs. The mod I and II have the same modal deformation response. This condition was observed between mod III and IV, and also mod V and VI.

Frequencies were higher in chimney geometry rather than in similar samples in literature analyses. For example, a natural frequency of around 80 Hz was obtained on a flat wall built around a port [15]. In Fig. 5, the frequency response of the upper surface of the chimney was shown as dimensionless deformation in order to show this situation in more detail. The deformation amplitude in the modes

was obtained as 1.4 times the circular pattern of the chimney. The fact that the dimensionless deformations of different knitting rows were the same, was due to the fact that the material used and the circular chimney size were the same. The same deformation location was not observed in some modes having the same frequency.

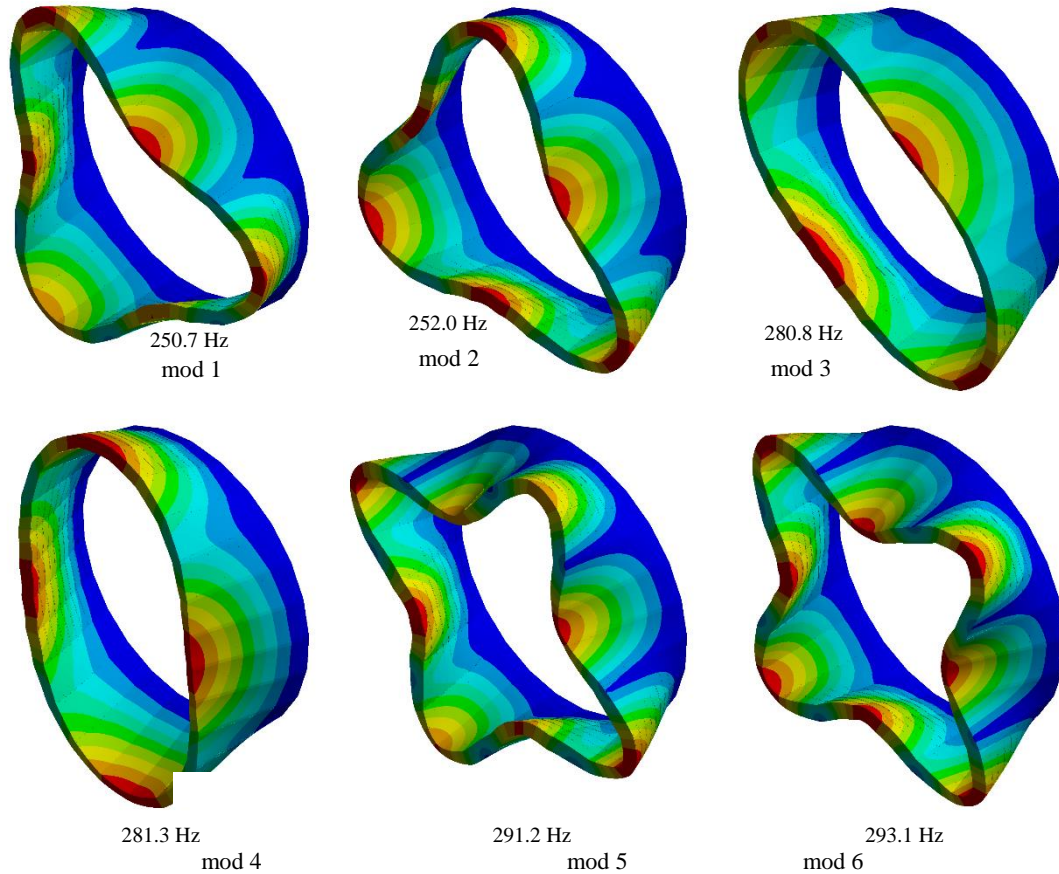


Figure 4. Frequency (Hz) and deformation structures resulting from the first 6 modes for $\alpha=0^\circ$

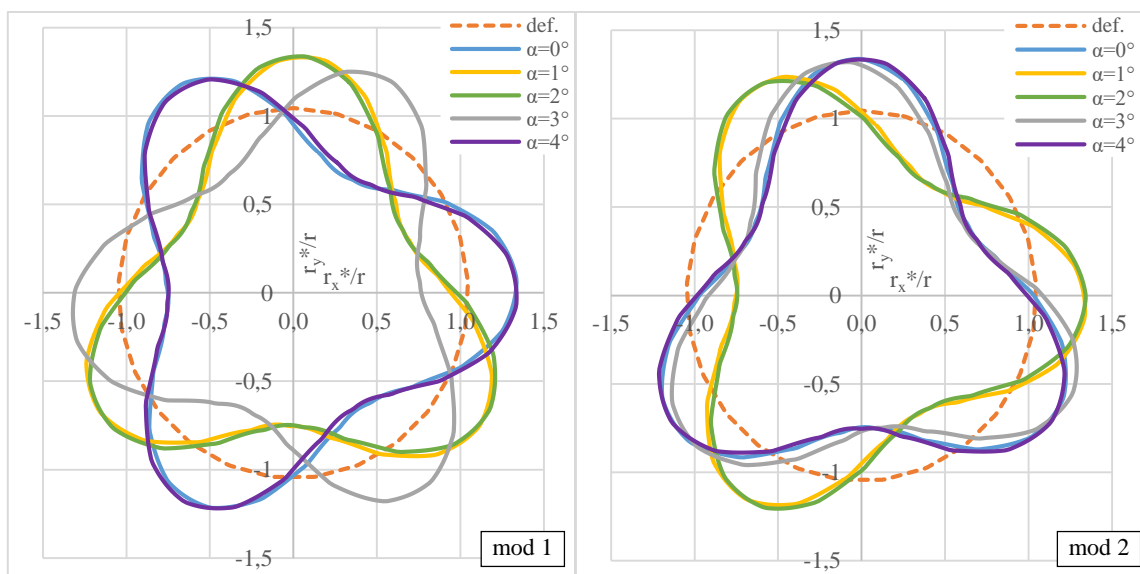


Figure 5. The deformation structure formed by different modes in the circle line on the upper chimney surface

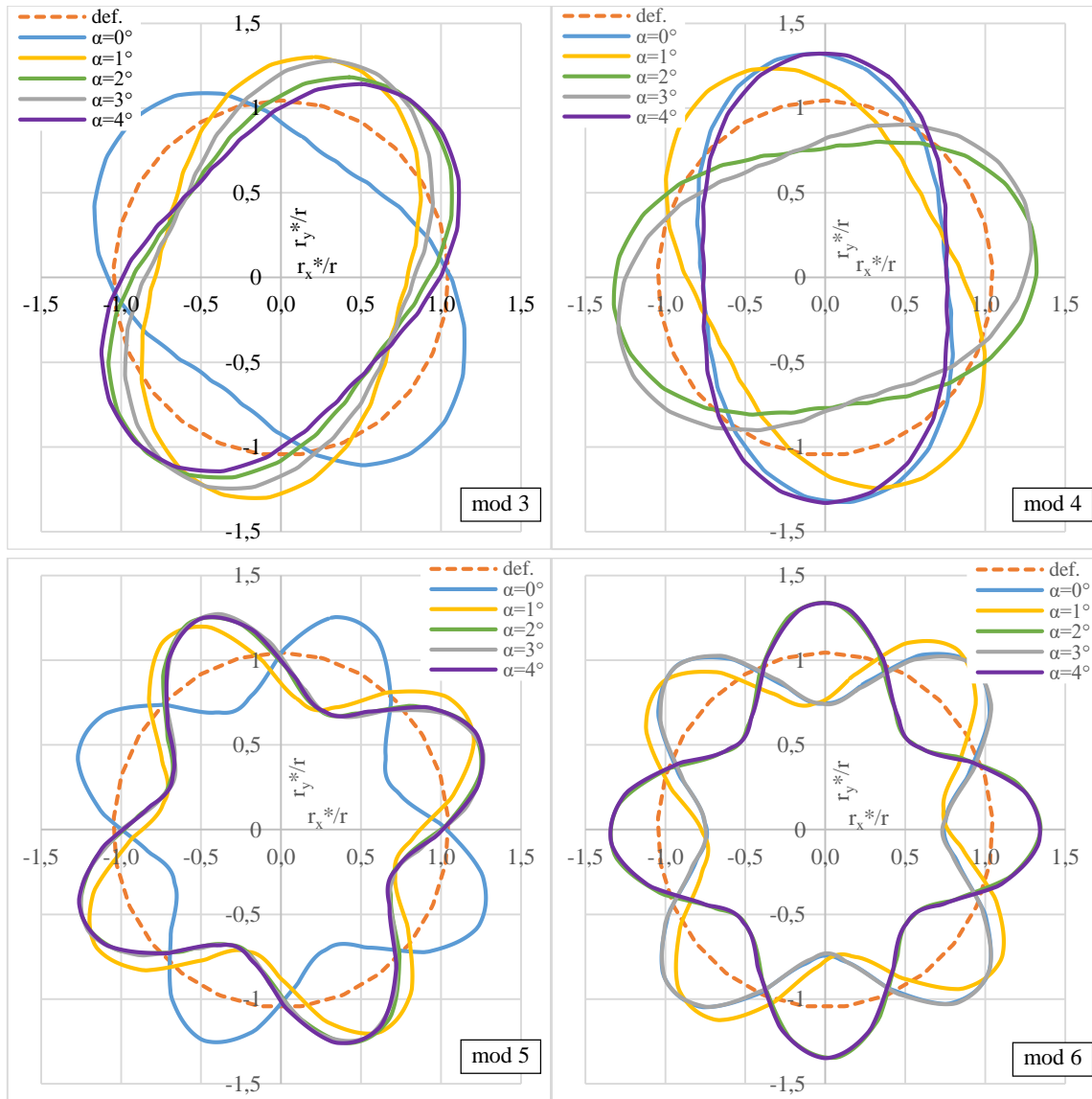


Figure 5. (Cont.) The deformation structure formed by different modes in the circle line on the upper chimney surface

In Fig. 6, the stresses in the chimney for different knitting rows as a result of the static compression were shown. Stress concentration locations were observed in the fillings between the bricks in the same layer. When the knitting order was changed, the stresses increased. In the case of the $\alpha=1^\circ$ condition, the stresses in the fillings in the same layer were high and occurred in the form of a ladder row. However, stress concentrations on the brick were dispersed and of low value. Low stress near brick edges and high stress in fills showed irregularity in $\alpha=2^\circ$ and $\alpha=3^\circ$ results. As a result of $\alpha=4^\circ$, there were high local

stresses occurred. In particular, it was observed that the filling between the bricks in the same layer had high stresses. The stresses of the brick were shown in the middle layer of the chimney profile in Fig. 7. The stresses in the bricks were lower than the stresses on the chimney. During different chimney knitting, the stresses and the symmetrical formation locations in the stress distribution have changed. The stress intensities formed at the brick corners shifted towards the brick edges in the cases of $\alpha=3^\circ$ and $\alpha=4^\circ$.

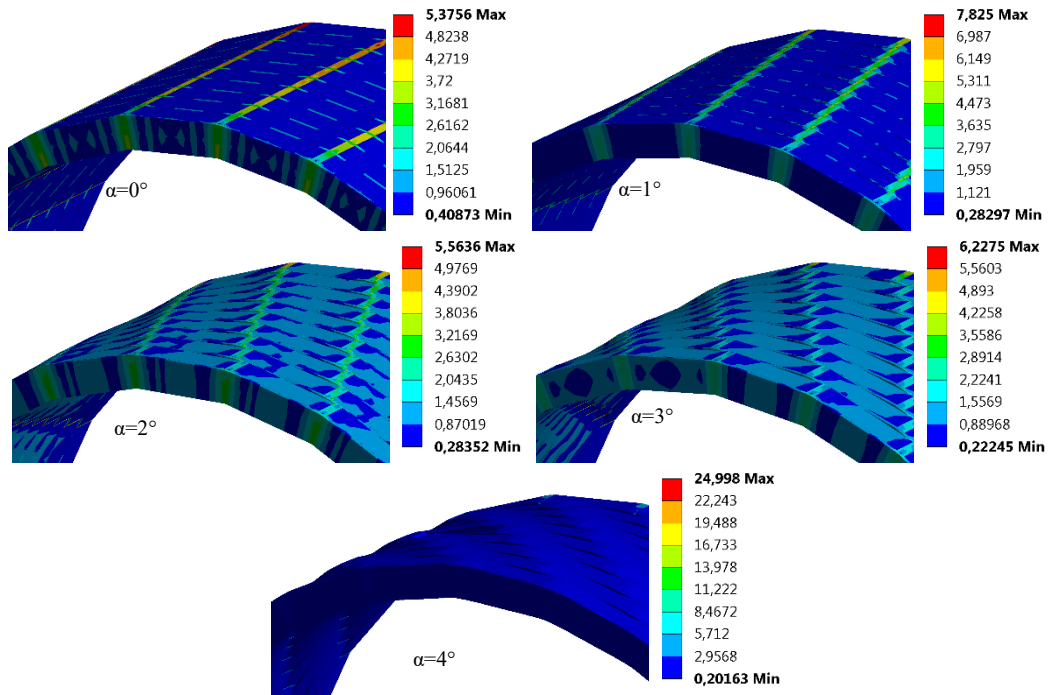


Figure 6. Von-Mises stresses (MPa) occurring in the chimney structure at different knitting rows

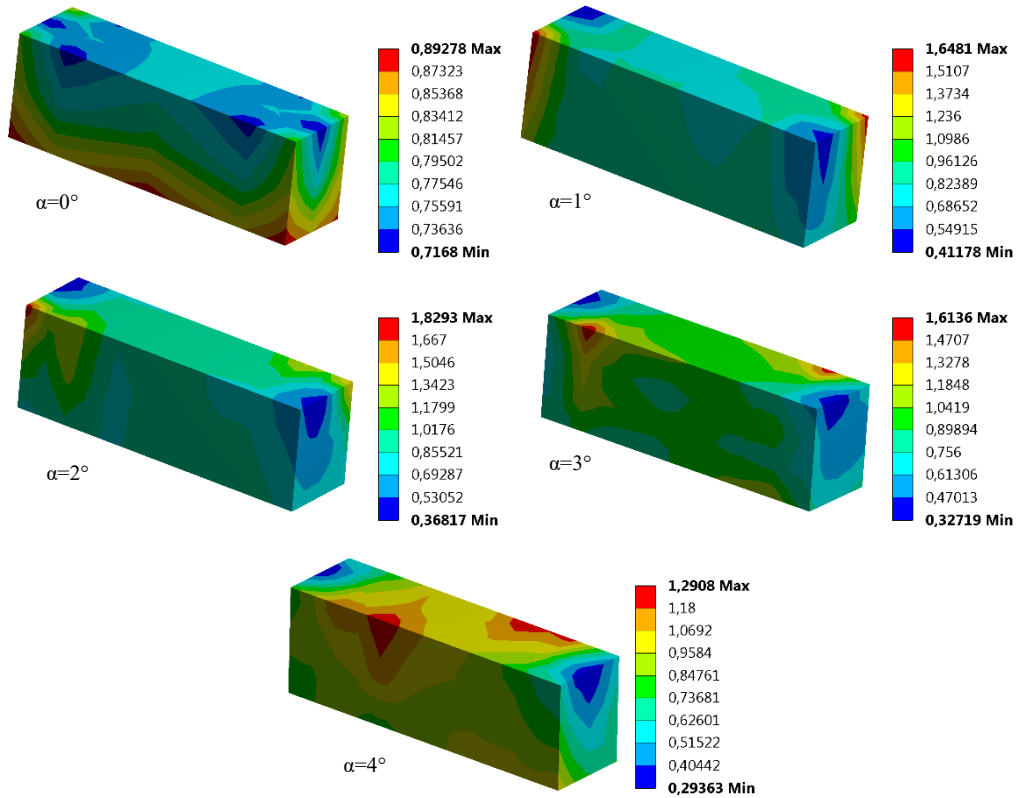


Figure 7. Von-Mises stresses (MPa) on a brick with chimney structural element at different lattice angles

4. Evaluation

In this study, the modal and static compression analyses of a layered chimney built with bar bricks with different knitting orders were numerically investigated. As a result of geometric irregularity, different stress and modal behaviours were obtained. If the findings are to be expressed item by item;

- Natural frequencies of chimneys with different knitting orders were observed between 250-290 Hz.
- The frequency difference between the modes was small and indicated the toughness of this structure to deformation.
- Knitting order differences have little effect on natural frequency.
- It is appropriate to use $\alpha=2^\circ$ knitting row as an alternative to the plain knitting order.
- The stresses were concentrated in the fillings located between the bricks in the same layer.
- In the cases of $\alpha=3^\circ$ and $\alpha=4^\circ$, the stresses occurring in the brick corners shifted toward the edges. This condition can reduce the breakage that may occur in the brick corners.

Declaration of Ethical Standards

The author of this article declares that the materials and methods used in this study do not require ethical committee permission and/or legal-special permission.

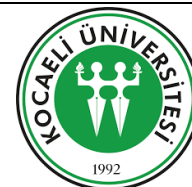
Conflict of Interest

The author declares that she has no known competing financial interests or personal relationships that could have appeared to influence the work reported in this paper.

References

- [1] Noble A.G., Geib M.M., 1984. Wood, brick, and stone. The North American Settlement Landscape. Vol. 2. Barns and Farm Structures. The University of Massachusetts Press.
- [2] Ramírez A., Nielsen J., Ayuga F., 2010. Pressure measurements in steel silos with eccentric hoppers. Powder Technology, **201**, pp. 7-20.
- [3] Winks R.G., Russell G.F. 1994. Effectiveness of SIROFLO in vertical silos. Proceedings of 6th International Working Conference on Stored-Protection, **2**, pp. 1245-1249.
- [4] Pande G.N., Liang J.X., Middleton J., 1989. Equivalent elastic moduli for brick masonry. Computers and Geotechnics, **8(3)**, pp. 243-265. [https://doi.org/10.1016/0266-352X\(89\)90045-1](https://doi.org/10.1016/0266-352X(89)90045-1)
- [5] Magenes G., Calvi G.M., 1997. In-plane seismic response of brick masonry walls. Earthquake Engineering and Structural Dynamics, **26**, pp. 1091-1112. [https://doi.org/10.1002/\(SICI\)1096-9845\(199711\)26:11<1091::AID-EQE693>3.0.CO;2-6](https://doi.org/10.1002/(SICI)1096-9845(199711)26:11<1091::AID-EQE693>3.0.CO;2-6)
- [6] Kaushik H.B., Rai D.C., Jain S.K., 2007. Stress-strain characteristics of clay brick masonry under uniaxial compression. Journal of Materials in Civil Engineering, ASCE, **19(9)**, pp. 728-739. [https://doi.org/10.1061/\(ASCE\)0899-1561](https://doi.org/10.1061/(ASCE)0899-1561)
- [7] Anthoine A., Magonette G., Magenes G., 1994. Shear-compression testing and analysis of brick masonry walls. Proceedings of the 10th European Conference on Earthquake Engineering, Vienna, Austria, 28 August - 2 September, pp. 1-6.
- [8] Valluzzi M.R., Valdemarca M., Modena C., 2001. Behavior of brick masonry vaults strengthened by frp laminates. Journal of Composites for Construction, **5(3)**, pp. 163-169.
- [9] Priestley M.J.N., Bridgeman D.O., 1974. Seismic resistance of brick masonry walls. Bulletin of the New Zealand Society for Earthquake Engineering, **7(4)**, pp. 167-187. <https://doi.org/10.5459/bnzsee.7.4.167-187>
- [10] Alforno M., Calderini C., Monaco, A., Venuti, F., 2019. Numerical modelling of masonry vaults with different brick pattern. Proceedings of IASS Annual Symposia, IASS 2019 Barcelona Symposium: Computational Methods, pp. 1-8. <https://doi.org/10.1007/s10518-022-01347-6>
- [11] Srinithya A., Kotagi N.M., Kumar G.M.V., Thammaiah, K.A. 2021. Parametric comparison of retrofitting methods in masonry using finite element analysis. IOP Conference Series: Earth and Environmental Science. **822**, 012017. <https://doi.org/10.1088/1755-1315/822/1/012017>
- [12] Lopez A., Fernandez-Davila V.I., 2017. Simplified method for evaluating seismic response of circular reinforced concrete silos. 16th World Conference on Earthquake, WCEE 2017, Paper No 2790.
- [13] Chi L., Lu S., Yaoc Y., 2019. Damping additives used in cement-matrix composites: a review. Composites Part B, **164**, pp. 26-36.

- [14] Leiben Z., Wang X., Wang Z., Yang B., Tian Y., He, R., 2018. Damping characteristics of cement asphalt emulsion mortars. *Construction and Building Materials*, **173**, pp. 201-208.
- [15] Zoltowski M., 2014. Investigations of harbour brick structures by using operational modal analysis. *Polish Maritime Research*, **21**, pp. 42-53. <https://doi.org/10.2478/pomr-2014-0007>



Design, Synthesis, and Biological Evaluation of 1,2,4-Triazole Derivatives as Potential Antimicrobial Agents

Yıldız UYGUN CEBECİ^{1,*}

¹ Department of Chemistry, Kırklareli University, Kırklareli, 39100, Turkey, **ORCID:** 0000-0001-7949-0329

Article Info

Research paper

Received : January 19, 2022

Accepted : October 18, 2022

Keywords

1,2,4-triazole,
fluoroquinolone,
antimicrobial activity,
multicomponent.

Abstract

In this study, we aimed to develop new biologically active compounds with antibacterial properties. 4-amino-5-methyl-2*H*-1,2,4-triazol-3(4*H*)-one (**1**) was converted to the corresponding Schiff bases (**2**) with the reaction with a 4-anis aldehyde. Acetic acid ethyl esters containing [1,2,4] triazole ring (**3**) were synthesized by the condensation of compounds (**2**) with ethyl bromoacetate in basic media. The reaction of compounds (**3**) with hydrazine hydrate led to the formation of acid hydrazides (**4**). The reaction of hydrazide (**4**) with phenyl isothio- and phenyl isocyanate produced the corresponding carbothioamide (**5a**) and carboxamide (**5b**). The basic treatment of carbothioamide (**5a**) and carboxamide (**5b**) produced 1,2,4-triazole (**6a**, **6b**) compounds, respectively. The reactions of (**6b**) with norfloxacin and ciprofloxacin in the presence of formaldehyde afforded the corresponding Mannich bases (**7a**, **7b**). The structural assignments of the new compounds were based on elemental analysis and spectral (IR, ¹H-NMR, and ¹³C-NMR) data. All newly synthesized compounds were screened for their antimicrobial activity. The in vitro antimicrobial activities of the compounds were evaluated against pathogenic microorganisms, and compounds 7a and 7b were found the most effective antimicrobial activity.

1. Introduction

Antimicrobial resistance (AMR), which has become a global problem, is a never-ending battle between humans and microbes. It is thought that the cause of 0.7 million deaths per year is microbial infection [1]. Antimicrobial resistance has become a major problem for health and development worldwide. Increasing antimicrobial resistance in the treatment of bacterial and fungal diseases has reached a dangerous level all over the world and affects people's health [2]. According to WHO studies on worldwide antimicrobial resistance, more than 10 million individuals are expected to be affected by multi-drug resistance diseases, with increased human mortality rates. Antimicrobial drug resistance is also likely to rise [3]. It is very important to increase research in this area to develop new and more effective antibacterial and antifungal drugs [4]. Standard antibiotic therapies such as β -lactams, aminoglycosides, tetracyclines, sulfonamides, quinolones, and others failed to prevent the spread of antimicrobial resistance (AMR) in specific locations during the twentieth

century by keeping bacteria inactive. As a result, there is a critical need in modern medicinal chemistry to develop and improve different ways of introducing a new active generation of antimicrobial drugs with alternative operating mechanisms in order to prevent antibiotic resistance in the future. When linked with other heterocyclic groups, 1,2,3-triazoles are remarkable scaffolds that have important biological effects [5-10]. N-containing heterocyclic chemicals are used in the pharmaceutical, agrochemical, and biological industries [11,12]. Among them, 1,2,3-triazoles and 1,2,4-triazoles exhibit a broad range of biological activities, such as antifungal [13-15], insomnia [16], anticancer [17], antineoplastic [18], antimicrobial [14,19–21,34], antibacterial [22,30], antioxidant [23,24,13], anti-inflammatory [25,26], antiviral [27,35], antimycobacterial [28,29], anticonvulsant [31], antidepressant [32], and anticoagulative [33] activities (Figure 1).

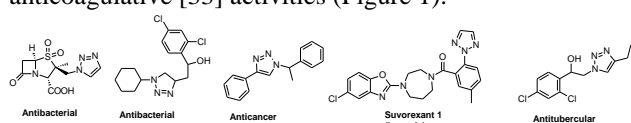


Figure 1. 1,3,4-Triazole-based biologically active agents.

* Corresponding Author: yildizuygun41@hotmail.com



A nitrogen atom links to an alkyl or aryl group in a Schiff base, providing a nitrogen-carbon double bond [34]. The presence of an electron pair on nitrogen in the azomethine group and the presence of heterocyclic structures connected to carbon and nitrogen in the azomethine group are the primary reasons for the biological and chemical significance of Schiff bases [35]. Many scientists have synthesized 1,2,4-triazole-Schiff base derivatives, which are generated by condensation of the 1,2,4-triazoles and the Schiff base structure, and studied their diverse biological and physicochemical features because of the benefits of both of these structural classes [36, 37].

The Mannich reaction serves as a useful model for comprehending how various drug synthesis processes work. The nucleophilic substitution process occurred through a carbon Mannich base or a nitrogen Mannich base. Mannich bases derived from various heterocycles exhibit unique biological activities, such as antitubercular [38], antimalarial [39] anticancer [40] and analgesic [41] properties.

Based on these observations, we believed that new bioactive compounds could be developed and synthesized in a series of 1,2,4-triazol-3-one derivatives in this research.

2. Experimental

2.1. Material and Methods

All the chemicals were purchased from Fluka Chemie AG Buchs (Switzerland) and used without further purification. Melting points of the synthesized compounds were determined in open capillaries on a Büchi B-540 melting point apparatus and are uncorrected. Reactions were monitored by thin-layer chromatography (TLC) on silica gel 60 F254 aluminum sheets (silica gel 60 GF254) and "0.25 mm thick silica gel plate. The mobile phase was ethyl acetate: diethyl ether, 1:1 (v:v) and detection was made using UV light. FT-IR spectra were recorded as potassium bromide pellets using a Perkin Elmer 1600 series FT-IR spectrometer. ¹H NMR and ¹³C NMR spectra were registered in DMSO-d₆ on a BRUKER AVANCE II 400 MHz NMR Spectrometer (400.13 MHz for ¹H and 100.62 MHz for ¹³C). The chemical shifts are given in ppm relative to Me₄Si as an internal reference, *J* values are given in Hz. The mass spectra were obtained on a Quattro LC-MS (70 eV) instrument.

2.1.1. 4-[(Z)-(4-methoxybenzylidene) amino]-5-methyl -2,4-dihydro-3H-1,2,4-triazol-3-one (2)

A solution of the corresponding compound **1** (10 mmol) in absolute ethanol was refluxed with anisaldehyde (10 mmol) for 3 h. After cooling the mixture to room temperature, a white solid appeared. This crude product was recrystallized from dimethyl sulfoxide/water (1:2) to afford the desired product.

Yield: 88 %, m.p: 190-192 °C. FT-IR (ν_{\max} , cm⁻¹): 3167 (NH), 3041 (aromatic CH), 1687 (C=O), 1512 (C=N). ¹H NMR (DMSO-*d*₆, δ ppm): 2.26 (3H, s, CH₃), 3.82 (3H, s, O-CH₃), 7.05 (2H, d, *J* = 8.0 Hz, arH), 7.78 (2H, d, *J* = 8.0 Hz, arH), 9.61 (1H, s, CH), 11.76 (1H, s, NH). ¹³C NMR (DMSO-*d*₆, δ ppm): 11.59 (CH₃), 55.87 (O-CH₃), arC: [114.93 (2CH), 126.46 (C), 129.93 (2CH), 144.68 (C)], 154.40 (CH), 151.80 (triazole C-3), 162.34 (triazole C-5). EI MS *m/z* (%): 233.40 ([M+1]⁺, 100), 103.33 (37), 114.21 (36), 215.22 (28), 182.20 (25), 152.26 (21).

2.1.2. Ethyl {4-[(Z)-(4-methoxybenzylidene) amino]-3-methyl-5-oxo-4,5-dihydro-1H-1,2,4-triazol-1-yl}acetate (3)

Compound **2** (10 mmol) was refluxed with 1 equivalent of sodium in absolute ethanol for 2 h. Then, ethyl bromoacetate

(10 mmol) was added and refluxed for an additional 8 h. After evaporating the solvent under reduced pressure, a solid appeared. The crude product was recrystallized from ethanol/water (1:2) to afford compound **4**.

Yield: 80 %, mp. 180-182 °C. FT-IR (ν_{\max} , cm⁻¹): 3058 (aromatic CH), 1685 (C=O), 1720 (C=O), 1510 (C=N). ¹H NMR (DMSO-*d*₆, δ ppm): 1.22 (2H, s, CH₂), 2.31 (2H, s, CH₂), 3.84 (3H, s, CH₃), 4.17 (3H, t, *J* = 4.0 Hz, CH₃), 4.57 (3H, s, O-CH₃), 7.07 (2H, d, *J* = 8.0 Hz, arH), 7.80 (2H, d, *J* = 8.0 Hz, arH), 9.56 (1H, s, CH). ¹³C NMR (DMSO-*d*₆, δ ppm): 11.40 (CH₃), 38.25 (CH₂), 49.20 (CH₂), 50.12 (CH₃), 55.87 (O-CH₃), arC: [111.20 (2CH), 122.52 (C), 128.12 (2CH), 141.85 (C)], 155.41 (CH), 152.79 (triazole C-3), 164.70 (triazole C-5), 170.64 (C=O). EI MS *m/z* (%): 319.20 ([M+1]⁺, 100), 247.30 (85), 149.45 (53).

2.1.3. 2-{4-[(Z)-(4-methoxybenzylidene)amino]-3-methyl-5-oxo-4,5-dihydro-1H-1,2,4-triazol-1-yl} acetohydrazide (4)

A solution of compound **3** (10 mmol) in ethanol was refluxed with hydrazine hydrate (30 mmol) for 5 h (controlled with TLC). After cooling it to room temperature, acetone was added to the mixture and was kept overnight in cold. The resulting solid separation was collected by

filtration and recrystallized from ethanol to afford the desired product.

Yield: 73 %, m.p: 189-191 °C. FT-IR (ν_{\max} , cm^{-1}): 3302 (NH_2), 3114 (NH), 3063 (aromatic CH), 1678 (C=O), 1703 (C=O), 1510 (C=N). ^1H NMR (DMSO-*d*₆, δ ppm): 2.08 (2H, d, J = 8.0 Hz, CH_2), 3.43 (2H, brs, $\text{NH}_2+\text{H}_2\text{O}$), 4.19 (3H, s, CH_3), 5.24 (3H, d, J = 4.0 Hz, CH_3), 6.88 (1H, s, arH), 7.40 (1H, d, J = 12.0 Hz, arH), 7.66 (1H, s, arH), 8.55 (1H, s, arH), 9.19 (1H, s, CH), 10.20 (1H, s, NH). ^{13}C NMR (DMSO-*d*₆, δ ppm): 12.98 (CH_3), 39.75 (CH_2), 41.10 (CH_2), 54.17 (O- CH_3), arC: [110.23 (CH), 111.74 (CH), 112.36 (CH), 120.47 (CH), 139.52 (C), 141.85 (C)], 155.37 (CH), 151.94 (triazole C-3), 166.64 (triazole C-5), 171.04 (C=O). EI MS m/z (%): 305.40 ($[\text{M}+1]^+$, 100), 273.18 (85), 190.12 (61).

General Procedure for the Synthesis of Compounds 5a-b

To a solution of corresponding compound 4 (10 mmol) in dichloromethane, phenylisocyanate (for **5b**) (20 mmol) or phenyl isothiocyanate (for **5a**) (20 mmol), was added and the mixture was stirred at room temperature for 24 hours. After evaporating the solvent under reduced pressure, a solid appeared. The crude product was recrystallized from ethanol to yield the target compounds.

2-[(4-[(1Z)-(4-methoxyphenyl)methylene]amino)-3-methyl-5-oxo-4,5-dihydro-1H-1,2,4-triazol-1-yl)acetyl]-N-phenylhydrazinecarbothioamide (5a)

Yield, 91 %; mp. 157-159 °C. FT-IR (ν_{\max} , cm^{-1}): 3112 and 3213 (3NH), 3067 (aromatic CH), 1687 (C=O), 1713 (C=O), 1578 (C=N), 1120 (C=S). ^1H NMR (DMSO-*d*₆, δ ppm): 2.09 (2H, d, J = 12.0 Hz, CH_2), 3.37 (3H, s, CH_3), 4.45 (3H, s, CH_3), 7.14-7.18 (3H, m, arH), 7.32-7.37 (3H, m, arH), 7.43-7.55 (3H, m, arH), 9.69 (1H, s, NH), 9.74 (1H, s, NH), 9.89 (1H, s, NH), 10.29 (1H, s, CH). ^{13}C NMR (DMSO-*d*₆, δ ppm): 12.10 (CH_2), 48.70 (CH_3), 56.45 (CH_3), arC: [111.20 (CH), 112.43 (CH), 117.64 (CH), 118.49 (CH), 120.13 (CH), 123.07 (CH), 126.73 (CH), 130.01 (CH), 138.10 (CH), 140.06 (C), 141.46 (C), 150.32 (C)], 154.37 (CH), 155.69 (triazole C-3), 158.30 (triazole C-5), 170.33 (C=O), 186.14 (C=S). EI MS m/z (%): 440.09 ($[\text{M}+1]^+$, 100), 319.41 (85), 200.76 (61), 174.20 (33).

2.1.4. 2-[(4-[(1Z)-(4-methoxyphenyl)methylene]amino)-3-methyl-5-oxo-4,5-dihydro-1H-1,2,4-triazol-1-yl)acetyl]-N-phenylhydrazine carboxamide (5b)

Yield, 90 %; mp. 160-162 °C. FT-IR (ν_{\max} , cm^{-1}): 3117 and 3215 (3NH), 3054 (aromatic CH), 1679 (C=O), 1748 (C=O), 1571 (C=N), 1129 (C=S). ^1H NMR (DMSO-*d*₆, δ ppm): 2.12 (2H, s, CH_2), 4.38 (3H, s, CH_3), 5.28 (3H, s, O- CH_3), 6.95-6.97 (2H, m, arH), 7.23-7.27 (3H, m, arH), 7.46-

7.50 (3H, m, arH), 7.98 (1H, s, arH), 8.21 (1H, s, NH), 8.70 (1H, s, NH), 8.79 (1H, s, NH), 9.97 (1H, s, CH). ^{13}C NMR (DMSO-*d*₆, δ ppm): 19.33 (CH_2), 49.41 (CH_3), 53.79 (CH_3), arC: [110.74 (CH), 118.14 (CH), 120.31 (2CH), 124.73 (2CH), 129.07 (2CH), 131.70 (CH), 136.49 (C), 138.36 (C), 140.19 (C)], 148.02 (CH), 153.55 (triazole C-3), 159.64 (triazole C-5), 170.76 (C=O), 173.42 (C=O). EI MS m/z (%): 424.87 ($[\text{M}+1]^+$, 100), 301.95 (81), 213.20 (73), 198.10 (49).

General Method For The Synthesis of Compounds 6a, 6b

A solution of corresponding compound 5 (10 mmol) in 2 N NaOH was refluxed for 3 h. The resulting solution was cooled to room temperature and acidified to pH 3-4 with 37% HCl. The precipitate formed was filtered, washed with water and recrystallized from ethanol/water (1:1) to afford the desired compounds

2.1.5. 2-[(5-mercapto-4-phenyl-4H-1,2,4-triazol-3-yl)methyl]-4-[(1E)-(4-methoxyphenyl)methylene]amino-5-methyl-2,4-dihydro-3H-1,2,4-triazol-3-one (6a)

Yield, 71 %; mp. 180-182 °C. FT-IR (ν_{\max} , cm^{-1}): 3071 (aromatic CH), 1691 (C=O), 1573 (C=N). ^1H NMR (DMSO-*d*₆, δ ppm): 2.02 (2H, s, CH_2), 4.79 (3H, s, CH_3), 5.06 (3H, s, O- CH_3), 6.91-7.57 (9H, m, arH), 8.56 (1H, s, CH), 13.37 (1H, s, SH). ^{13}C NMR (DMSO-*d*₆, δ ppm): 49.09 (CH_2), 50.76 (CH_3), 57.12 (O- CH_3), arC: [110.98 (CH), 112.09 (CH), 113.79 (2CH), 119.03 (2CH), 121.93 (CH), 123.73 (CH), 125.04 (CH), 130.55 (C), 134.77 (C), 139.10 (C)], 148.45 (CH), 151.77 (triazole C-3), 153.20 (triazole C-3), 158.88 (triazole C-5), 160.30 (triazole C-5). EI MS m/z (%): 422.30 ($[\text{M}+1]^+$, 100), 198.22 (73), 219.33 (54).

2.1.6. 4-[(1E)-(4-methoxyphenyl)methylene]amino-5-methyl-2-[(5-oxo-4-phenyl-4,5-dihydro-1H-1,2,4-triazol-3-yl)methyl]-2,4-dihydro-3H-1,2,4-triazol-3-one (6b)

Yield, 73 %; mp. 188-190 °C. FT-IR (ν_{\max} , cm^{-1}): 3077 (aromatic CH), 1698 (C=O), 1578 (C=N). ^1H NMR (DMSO-*d*₆, δ ppm): 1.24 (2H, s, CH_2), 3.35 (3H, s, CH_3), 5.76 (3H, s, O- CH_3), 6.93-6.97 (3H, m, arH), 7.23-7.27 (3H, m, arH), 7.48-7.50 (3H, m, arH), 8.00 (1H, s, CH), 8.84 (1H, s, NH). ^{13}C NMR (DMSO-*d*₆, δ ppm): 49.29 (CH_2), 51.37 (CH_3), 58.34 (O- CH_3), arC: [113.54 (CH), 114.09 (CH), 115.66 (2CH), 117.30 (2CH), 119.35 (CH), 120.31 (CH), 121.38 (C), 129.36 (C), 138.54 (C)], 143.53 (CH), 153.76 (triazole C-3), 155.20 (triazole C-3), 159.23 (triazole C-5),

161.57 (triazole C-5). EI MS m/z (%): 406.78 ($[M+1]^+$, 100), 119.20 (71), 298.25 (55).

2.2. General Method for the Synthesis of Compounds 7a-b

In the solution of corresponding compounds **6a** and **6b** (10 mmol) in dimethyl formamide (5 mmol), norfloxacin or ciprofloxacin (10 mmol) was added and the mixture was stirred at room temperature in the presence of formaldehyde (50 mmol) for 24 h. The solid precipitated was filtered off and recrystallized from dimethylsulfoxide: water (1:1, v/v).

(E)-7-(4-((3-((4-(4-methoxybenzylideneamino)-3-methyl-5-oxo-4,5-dihydro-1,2,4-triazol-1-yl)methyl)-5-oxo-4-phenyl-4,5-dihydro-1,2,4-triazol-1-yl)methyl) piperazin-1-yl)-1-cyclopropyl-6-fluoro-4-oxo-1,4-dihydro quinoline-3-carboxylic acid (7a)

Yield, 80 %; mp. 193-195 °C. FT-IR (ν_{\max} , cm^{-1}): 3324 (OH), 3110 (NH), 3075 (aromatic CH), 1703 (C=O), 1716 (C=O), 1578 (C=N). ^1H NMR (DMSO- d_6 , δ ppm): 1.18 (3H, s, CH_3), 1.31 (2H, s, CH_2), 2.73 (2H, s, CH_2), 2.83 (2H, s, CH_2), 2.89 (2H, s, CH_2), 3.35 (8H, s, $4\text{CH}_2+\text{H}_2\text{O}$), 3.81 (3H, s, $-\text{OCH}_3$), 6.96-8.65 (11H, m, arH), 8.94 (1H, s, CH), 8.99 (1H, s, CH), 9.19 (1H, s, CH), 15.22 (1H, s, OH). ^{13}C NMR (DMSO- d_6 , δ ppm): 11.78 (CH_3), 25.41 (CH_2), 28.78 (CH_2), 29.11 (CH_2), 30.03 (CH_2), 31.46 (CH_2), 33.89 (CH_2), 47.23 (CH_2), 51.76 (CH_2), 55.85 (O- CH_3), arC: [110.89 (CH), 111.75 (CH), 113.50 (CH), 119.30 (CH), 120.01 (CH), 121.28 (CH), 122.55 (CH), 123.52 (CH), 124.61 (CH), 126.74 (C), 127.39 (CH), 128.41 (CH), 129.47 (C), 130.53 (C), 132.34 (C), 133.79 (C), 135.06 (C), 136.80 (C), 139.80 (C)], 147.20 (CH), 148.85 (CH), 150.15 (CH), 155.20 (triazole C-3), 158.63 (triazole C-3), 160.61 (triazole C-5), 163.85 (triazole C-5), 170.11 (C=O), 171.06 (C=O). EI MS m/z (%): 301.85 (100), 749.52 ($[M+1]^+$, 77), 299.20 (63), 100.80 (41).

2.2.1. (E)-7-(4-((3-((4-(4-methoxybenzylideneamino)-3-methyl-5-oxo-4,5-dihydro-1,2,4-triazol-1-yl) methyl)-5-oxo-4-phenyl-4,5-dihydro-1,2,4-triazol-1-yl)methyl) piperazin-1-yl)-1-ethyl-6-fluoro-4-oxo-1,4-dihydro quinoline-3-carboxylic acid (7b)

Yield, 78 %; mp. 190-192 °C. FT-IR (ν_{\max} , cm^{-1}): 3320 (OH), 3108 (NH), 3061 (aromatic CH), 1710 (C=O), 1725 (C=O), 1581 (C=N). ^1H NMR (DMSO- d_6 , δ ppm): 1.17 (3H, s, CH_3), 1.42 (2H, s, CH_2), 2.73 (2H, s, CH_2), 2.89 (2H, s, CH_2), 3.39 (8H, s, $4\text{CH}_2+\text{H}_2\text{O}$), 4.14 (3H, d, $J = 8.0$ Hz, O- CH_3), 4.58 (3H, s, CH_3), 6.95-8.25 (11H, m, arH), 8.77 (1H, s, CH), 8.93 (1H, s, CH), 15.30 (1H, s, OH). ^{13}C NMR (DMSO- d_6 , δ ppm): 11.85 (CH_3), 26.10 (CH_2), 30.30 (CH_2),

39.52 (CH_2), 41.41 (CH_2), 42.85 (CH_2), 50.98 (CH_2), 51.36 (CH_2), 52.00 (CH_3), 56.18 (O- CH_3), arC: [110.03 (CH), 111.50 (CH), 115.55 (CH), 118.36 (CH), 120.18 (CH), 122.28 (CH), 123.61 (CH), 125.80 (CH), 126.78 (CH), 127.30 (C), 128.77 (CH), 129.60 (CH), 130.61 (C), 132.70 (C), 134.80 (C), 136.61 (C), 137.11 (C), 138.03 (C), 139.13 (C)], 148.12 (CH), 149.40 (CH), 154.79 (triazole C-3), 157.90 (triazole C-3), 160.66 (triazole C-5), 165.73 (triazole C-5), 169.80 (C=O), 171.28 (C=O). EI MS m/z (%): 257.85 (100), 759.80 ($[M+\text{Na}]^+$, 71), 360.12 (64), 414.30 (39).

2.3. General Method for the Synthesis of Compounds 8a-c.

A solution of the corresponding compound **4** (10 mmol) in

absolute ethanol was refluxed with an appropriate aldehyde

(10 mmol) for 3 hours. After cooling the mixture to room temperature, a white solid appeared. This crude product was recrystallized from dimethylsulfoxide/water (1:2) or ethanol to afford the desired product.

N'-[(1Z)-(4-methoxyphenyl)methylene]-2-(4-[[[(1E)-(4-methoxyphenyl)methylene] amino]-3-methyl-5-oxo-4,5-dihydro-1H-1,2,4-triazol-1-yl]acetohydrazide (8a)

Yield, 90 %; mp. 177-179 °C. FT-IR (ν_{\max} , cm^{-1}): 3113 (NH), 3051 (aromatic CH), 1675 (C=O), 1570 (C=N). ^1H NMR (DMSO- d_6 , δ ppm): 2.13 (3H, s, CH_3), 2.31 (2H, s, CH_2), 4.79 (3H, s, CH_3), 5.30 (3H, s, CH_3), 6.96-7.83 (8H, m, arH), 8.64 (1H, s, CH), 9.61 (1H, s, CH), 11.51 (1H, s, NH). ^{13}C NMR (DMSO- d_6 , δ ppm): 11.10 (CH_3), 11.46 (CH_3), 46.72 (CH_2), 55.85 (CH_3), arC: [114.76 (CH), 114.86 (CH), 114.99 (CH), 126.27 (C), 127.04 (C), 128.98 (CH), 129.05 (CH), 129.21 (CH), 130.09 (CH), 130.44 (CH), 145.27 (C), 154.01 (C)], 144.34 (CH), 144.62 (CH), 161.20 (triazole C-3), 162.15 (triazole C-3), 168.34 (C=O). EI MS m/z (%): 437.58 ($[M+1]^+$, 100), 217.52 (77), 120.63 (51), 109.41 (33).

2.3.1. 2-(4-[[[(1E)-(4-methoxyphenyl) methylene] amino]-3-methyl-5-oxo-4,5-dihydro-1H-1,2,4-triazol-1-yl]-N'-[(1Z)-phenyl methylene] acetohydrazide (8b)

Yield, 89 %; mp. 173-175 °C. FT-IR (ν_{\max} , cm^{-1}): 3116 (NH), 3071 (aromatic CH), 1703 (C=O), 1583 (C=N). ^1H NMR (DMSO- d_6 , δ ppm): 2.34 (2H, s, CH_2), 4.91 (6H, s, 2CH_3), 7.43-8.26 (9H, m, arH), 9.73 (1H, s, NH), 11.61 (1H, s, CH), 11.70 (1H, s, CH). ^{13}C NMR (DMSO- d_6 , δ ppm): 11.44 (CH_3), 46.78 (CH_2), 55.91 (CH_3), arC: [127.45 (CH), 127.62 (CH), 128.27 (CH), 128.82 (CH), 129.27 (CH),

129.50 (CH), 130.51 (CH), 132.07 (CH), 133.79 (C), 134.35 (C), 143.83 (CH), 144.80 (C), 148.17 (CH), 154.58 (CH), 150.69 (triazole C-3), 163.87 (triazole C-3), 168.21 (C=O). EI MS m/z (%): 407.12 ($[M+1]^+$, 100), 309.41 (73), 198.74 (49).

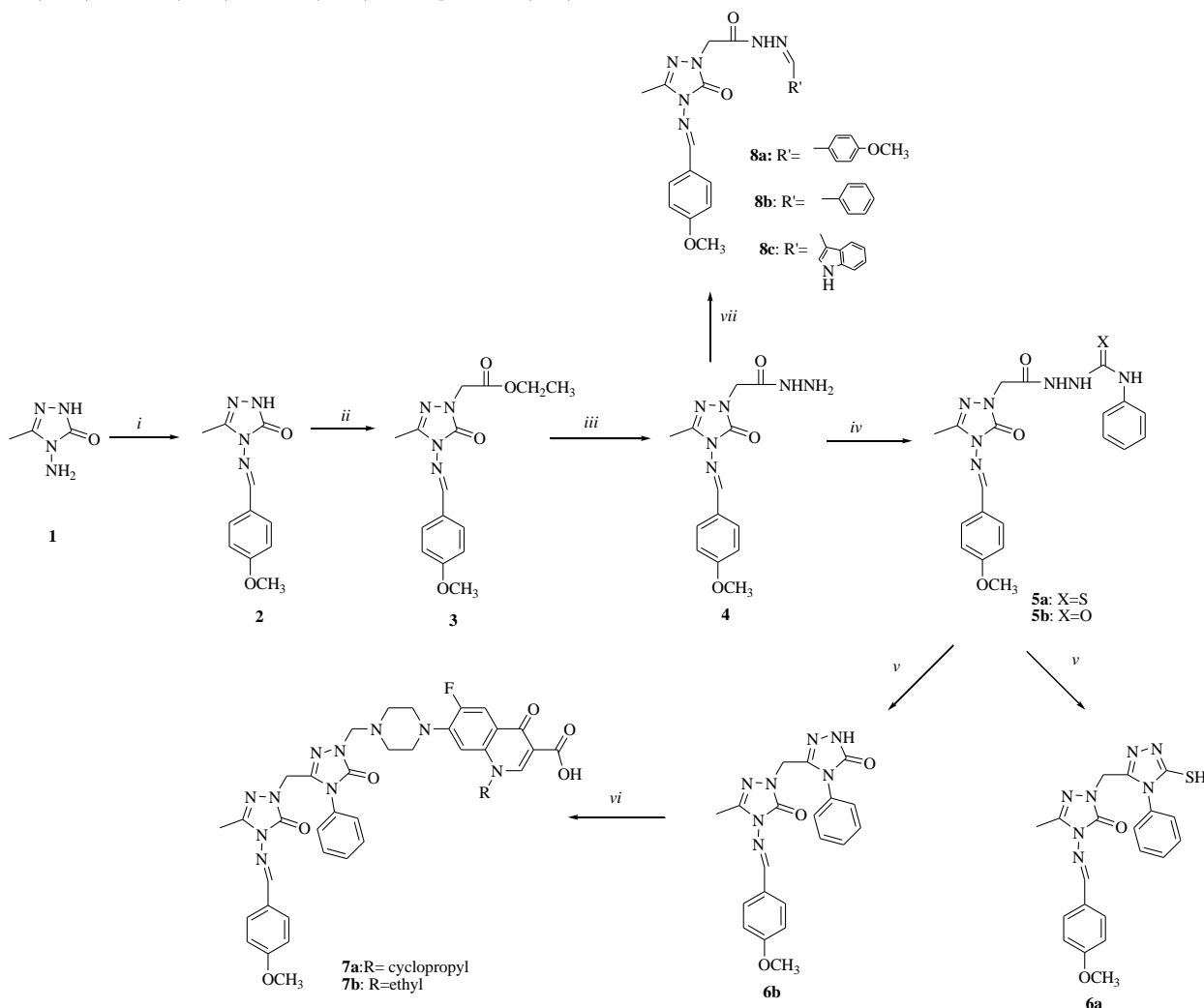
2.3.2. N'-[(1Z)-1H-indol-3-ylmethylene]-2-(4-[[[(1E)-(4-methoxyphenyl)methylene] amino]-3-methyl-5-oxo-4,5-dihydro-1H-1,2,4-triazol-1-yl)acetohydrazide (8c)

Yield, 91 %; mp. 180-182 °C. FT-IR (ν_{\max} , cm^{-1}): 3120 (NH), 3080 (aromatic CH), 1710 (C=O), 1570 (C=N). ^1H NMR (DMSO- d_6 , δ ppm): 2.14 (2H, s, CH_2), 4.37 (3H, s, CH_3), 4.84 (3H, s, CH_3), 6.98-8.39 (8H, m, arH), 9.74 (1H, s, NH), 10.15 (1H, s, NH), 11.29 (1H, s, CH), 11.54 (1H, s, CH), 11.83 (1H, s, CH). ^{13}C NMR (DMSO- d_6 , δ ppm): 11.51 (CH_3), 47.20 (CH_2), 55.85 (CH_3), arC: [111.41 (CH),

112.50 (CH), 113.61 (CH), 114.39 (CH), 115.34 (CH), 118.52 (CH), 121.75 (CH), 124.60 (CH), 130.41 (C), 134.85 (C), 135.90 (C), 137.50 (C), 141.97 (C), 148.85 (CH), 150.10 (CH), 158.52 (triazole C-3), 160.28 (triazole C-3), 170.01 (C=O). EI MS m/z (%): 446.10 ($[M+1]^+$, 100), 250.47 (73), 100.19 (49).

3. Results And Discussion

The goal of the study is to create new antibacterial hybrids that include a variety of pharmacophore groups. The previous observation of Scheme 1 was completed and intermediate molecular processes were accomplished. The components were synthesized using traditional methods, and the synthesis was finalized using the thin-layer chromatography (TLC) method. The basic spectral and physicochemical data formed the basis for all compound structures.



Scheme 1. Reactions and conditions. *i*: anisaldehyde, 115-120 °C, oil bath, 2 h; *ii*: absolute ethanol, Na, ethyl bromoacetate, reflux for 8 h; *iii*: absolute ethanol, hydrazine hydrate, reflux for 12 h; *iv*: phenyl isothiocyanate (for **6a**), or phenyl isocyanate (for **6b**) in dichloro-methane, room temperature for 24 h; *v*: 2 N NaOH in ethanol/water (1:1), reflux for 6 h; *vi*: HCl, formaldehyde, ciprofloxacin (for **7a**), norfloxacin (for **7b**),

By investigating on our previous study on antimicrobial drugs, we set out to develop new compounds with significant activity in our lab. **6a-b** are 1,2,4-triazole derivatives that were synthesized in this article. Compounds were characterized using ^1H and ^{13}C NMR, EI-MS, FT-IR, and mass spectrometry for all synthesized compounds. The known compound **1** was reacted with anisaldehyde and afforded the desired product of compound **2** known as a Schiff base. The characterization of this compound shows that the reaction was successfully achieved from the FT IR spectrum that the peak of NH_2 was not observed and the additional peak was added such as aromatic CH in 3041 cm^{-1} . Also in NMR spectra the aromatic protons resonated between $7.05\text{--}7.78\text{ ppm}$ and the imine --CH bond resonated downfield at 9.61 ppm in ^1H NMR spectra. In ^{13}C NMR the additional aromatic carbon atoms and imine carbon were detected. Another evidence of compound **2** is the molecular ion peak as $\text{M}+1$. Ethyl (4-[(2,4-dichlorophenyl)methylene]amino)-3-methyl-5-oxo-4,5-dihydro-1*H*-1,2,4-triazol-1-yl)acetate (**3**) was synthesized from compound **2** with ethyl bromoacetate in the presence of a protic solution and resulted with an additional sharp C=O peak in 1720 cm^{-1} , the additional ester group ($\text{--OCH}_2\text{CH}_3$) protons were resonated respectively between 2.31 ppm and 4.57 ppm . The $\text{M}+1$ value shows the reliability of the corresponding compound **3**. FT IR data of the acetohydrazide derivative of compound **4** give details of the --NHNH_2 group in 3302 and 3114 cm^{-1} that take place instead of the ester group. The NH_2 and NH protons were resonated respectively in 3.43 and 9.20 ppm and controlled exchanging with D_2O solution. 2-[4-[(*Z*)-(4-methoxybenzylidene)amino]-3-methyl-5-oxo-4,5-dihydro-1*H*-1,2,4-triazol-1-yl]aceto hydrazide (**4**) was reacted with different iso(thio)cyanates to convert to carbothiohydrazide **5a** and carbohydrazide **5b** derivatives. Compared the carbo(thio)hydrazide derivatives (**5a-b**) with its starting material of compound **4**, an additional NH and C=S peak for compounds **5a**, or C=O peak for compound **5b** was seen in their FT IR spectra.

The cyclization reaction of compound **5a-b** in basic media resulted in a 1,2,4-triazole ring in the molecule of compound **6** derivatives. The cyclization reactions of compounds **6a-b** were also supported by the NMR data, for **6a** --SH tautomeric form resonated approximately at 13.37 ppm whereas for the compound **6b** the --NH tautomeric form occurred and resonated at 8.84 ppm . The molecular ion peak of these compounds was detected in electron impact

ionization techniques. In the mannich reaction with norfloxacin or ciprofloxacin in the presence of formaldehyde, compounds **6a-b** were allowed to bind the large molecule to the starting material to afford the target molecule **7a-b**. It is seen in the IR spectra that additional C=O peaks between $1703\text{--}1725\text{ cm}^{-1}$, aromatic CH peak and in the ^{13}C or ^1H NMR spectra additional CH_2 carbon atoms and protons of piperazine ring, aromatic carbons and protons also were resonated differently from the starting material.

In excellent yields, arylmethyleneacetohydrazides (**8a-c**) were synthesized by reacting compound **4** with different aromatic aldehydes in ethanol solutions. ^1H -NMR, ^{13}C -NMR, IR, and mass spectroscopy methods can all be used to prove the synthesis of compounds **8a-c**. Additional signals coming from the arylidene moiety have been seen in the aromatic area of the ^1H -NMR spectra of compounds **8a-c**. Additionally, signals were observed at 9.61 , 11.61 , and 11.54 ppm , whereas the signal associated with the --NHNH_2 moiety, which had previously been observed at 3.43 ppm in the ^1H -NMR spectrum, disappeared.

Antimicrobial Activity

Antimicrobial activity or susceptibility tests were performed to determine the in-vitro activity of the antimicrobial agent against a particular bacterial species. Two techniques are used to measure susceptibility testing of microorganisms, including "diffusion" and "dilution". The disc diffusion technique is a frequently used technique and the sensitivity of the antibiotic absorbed into paper discs (the solution to be measured by antibacterial activity) is based on the diffusion of the organism to the medium in which the organism is inoculated.

This study found that most of the compounds synthesized in this study were able to bind to the test chemicals (Table 1). There were seven compounds that showed outstanding activity on Gram-positive and Gram-negative bacteria of the test microorganisms with MIC values 0.24 g/mL , including **7a-b**, which had fluoroquinolone nuclei in their structures. The carboxamides, **4a**, **4b**, and triazoles, **5a**, **5b**, which were obtained from intramolecular cyclisation of **4a**, **4b**, displayed selective activity on a Gram-positive coccal bacterium, *Staphylococcus aureus* (Sa), and *Mycobacterium smegmatis* (Ms), atypical tuberculosis factor leading to morbidity and mortal

Table 1. Screening for the activity of newly synthesized compounds.

Comp No	Microorganisms and Minimal Inhibitory Concentrations (µg/mL)								
	Ec	Yp	Pa	Sa	Ef	Bc	Ms	Ca	Sc
2	-	-	-	125	-	-	-	-	-
3	-	-	-	-	-	500	-	-	-
4a	31.3	31.3	31.3	125	-	-	62.5	-	-
4b	31.3	31.3	31.3	125	-	125	62.5	-	-
5a	-	-	-	62,5	-	-	31.3	-	-
5b	-	-	-	31.3	-	125	15.65	-	-
6a	-	-	-	125	-	-	31.3	-	-
6b	-	-	-	125	-	-	31.3	-	-
7a	<0.24	<0.24	<0.24	<0.24	<0.24	<0.24	-	-	-
7b	<0.24	<0.24	<0.24	<0.24	<0.24	<0.24	-	-	-
8a	31.3	31.3	31.3	125	-	-	62.5	-	-
8b	62.5	31.3	31.3	62.5	125	125	62.5	125	125
8c	125	62.5	62.5	125	250	259	62.5	250	125
Amp.	0	8	128	0	5	5			
Strep.									
Flu								<8	<8

Ec: *Escherichia coli* ATCC 25922, Yp: *Yersinia pseudotuberculosis* ATCC 911, Pa: *Pseudomonas aeruginosa* ATCC 43288, Sa: *Staphylococcus aureus* ATCC 25923, Ef: *Enterococcus faecalis* ATCC 29212, Bc: *Bacillus cereus* 702 Roma, Ms: *Mycobacterium smegmatis* ATCC607, Ca: *Candida albicans* ATCC 60193, *Saccharomyces cerevisiae* RSKK 251, Amp.: Ampicillin, Str.: Streptomycin, Flu.: Fluconazole, (—): no activity.

4. Conclusion

Norfloxacin and ciprofloxacin moieties have been converted into various pharmacophore heterocycles in various new hybrid drugs described in this work. Thus, we integrated all of these potentially useful chemotherapeutic units, namely the 1,2,4-triazole, norfloxacin, and ciprofloxacin moieties, in this study. Antimicrobial screening studies were also conducted as part of the study. The 1,2,4-triazole and ciprofloxacin or norfloxacin moiety (**7a**, **7b**) synthesized compounds showed good-moderate activity against a variety of test microorganisms.

Declaration of Ethical Standards

The author of this article declares that the materials and methods used in this study do not require ethical committee permission and/or legal-special permission.

Conflict of Interests

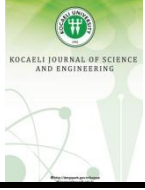
The authors of this study have stated that they have no conflicts of interest that could have affected the outcomes.

References

- [1] World health organization, Global antimicrobial report, 2019. Only available online: <https://www.who.int/health-topics/antimicrobial-resistance>. **27**.
- [2] Jagadale S., Chavan A., Shinde A., Sisode V., Bobade, V.D., Mhaske P. C., 2020. Synthesis and antimicrobial evaluation of new thiazolyl-1, 2, 3-triazolyl-alcohol derivatives. *Medicinal Chemistry Research*, **29**, pp. 989-999.
- [3] Li D., S Qiao, Y. G., Yi, F., Jiang, J. Y., Xu, X. X., Piao, X. S., Han, In K., Thacker. P., 2000. Performance of Growing-Finishing Pigs Fed Sesame Meal Supplemented Diets Formulated Using Amino Acid Digestibilities Determined by the Regression Technique. *Asian-Australasian Journal of Animal Sciences* **13**, pp. 46-52.
- [4] Ferreira, M.L.G., Pinheiro, L.C.S., Santos-Filho, O. A. Peçanha, M.D. S., Sacramento, C.Q. Machado, V., Ferreira, V.F. Moreno, T., Souza & Núbia Boechat L.. 2014. Design, synthesis, and antiviral activity of new 1H-1,2,3-triazole nucleoside ribavirin analogs. *Medicinal Chemistry Research* **23**, pp. 1501–1511

- [5] Hong, M.C., Hsu, D.I., Bounthavong, M., 2013. Ceftolozane/tazobactam: a novel antipseudomonal cephalosporin and β -lactamase-inhibitor combination. *Infect Drug Resist*, **29**, pp. 215–223.
- [6] Shaikh, M.H., Subhedar, D.D., Kalam, F. A., Jaiprakash, K., Sangshetti, N., Shingate, B.B., 2016. 1, 2, 3-Triazole incorporated coumarin derivatives as potential antifungal and antioxidant agents. *Chinese Chemical Letters*, **27**, pp. 295-301.
- [7] Dofe, V.S., Sarkate, A.P., Kathwate, S. H., Gill, C.H., 2017, Synthesis, antimicrobial activity and anti-biofilm activity of novel tetrazole derivatives. *Heterocyclic Communications*, **23**, pp. 325–330.
- [8] Khloya, P., Kumar, S., Kaushik, P., Surain, P., Kaushik, D., Sharma, P. K., 2015. Synthesis and biological evaluation of pyrazolylthiazole carboxylic acids as potent anti-inflammatory-antimicrobial agents. *Bioorg Med Chem Lett*. **25(6)**, pp. 1177-1181
- [9] Ceylan, S.; Bektas, H.; Bayrak, H.; Demirbas, N.; Alpay-Karaoglu, S.; and Ülker, S. 2013. Syntheses and Biological Activities of New Hybrid Molecules Containing Different Heterocyclic Moieties. *Arch. Pharm. Chem. Life Sci.*, **346**, pp. 743–756.
- [10] Chen, M.D., Lu, S.J., Yuag, G.P., Yang, S.Y., Du, X.L., 2000. Synthesis and antibacterial activity of some heterocyclic beta-enamino ester derivatives with 1, 2, 3- triazole, *Heterocycl. Commun*, **6**, pp. 421-427.
- [11] Holla, B.S., Sarojini, B.K., Sooryanarayana, R., Akberali, P.M., Kumari, N.S., Shetty, V., 2001. Synthesis of some halogen-containing 1,2,4-triazolo-1,3,4-thiadiazines and their antibacterial and anticancer screening studies—Part I, II *Farmaco*, **56**, pp. 565–570.
- [12] Ozdemir, S.B., Cebeci, Y.U., Bayrak, H., Mermer, A., Ceylan, S., Demirbas, A., Karaoglu, S.A., Demirbas, N., 2017. Synthesis and antimicrobial activity of new piperazine-based heterocyclic compounds. *Heterocycl. Commun.*, **23(1)**, pp. 43-54.
- [13] Uygun Cebeci, Y., Ceylan, S., Demirbas, N., Alapay Karaoglu, S., 2021. Conventional and Microwave Assisted Synthesis of Novel 1,2,4- Triazole Derivatives Containing Tryptamine Skeleton and Investigation of Antimicrobial Activity, *Letters in Organic Chemistry*. **18 (2)**, pp.143-155.
- [14] Mentese, M.Y., Bayrak, H., Uygun, Y., Mermer, A., Ulker, S., Karaoglu, S.A., Demirbas, N. 2013. Microwave assisted synthesis of some hybrid molecules derived from norfloxacin and investigation of their biological activities. *Eur. J. Med. Chem.*, **67**, pp. 230-242.
- [15] Ceylan, S., Bayrak, H., Demirbaş, A.; Ulker, S.; Karaoğlu Alpay, S.; Demirbas, N., 2014. Synthesis of Some New Hybride Molecules Containing Several Azole Moieties and Investigation of Their Biological Activities, *Russian Journal of Bioorganic Chemistry*, **40**, pp. 314–329.
- [16] Choudhary, M. I.; Adhikari, A.; Rasheed, S.; Bishnu, P. M.; Hussain, N.; Kaleem, Atta-ur-Rahman, W. A. 2011. *Phytochemistry. Lett.*, **4**, pp. 404–406.
- [17] Molecular Operating Environment (MOE) C. C. G. I., 1010 Sherbooke St. West, Suite 910, Montreal, QC, Canada, H3A 2R7, 2015.
- [18] National Committee for Clinical Laboratory Standard, 1993, 13.
- [19] Ebner, C., Culhane, J. C.; Winkelman, T. N.; Haustein, M. D.; Dittyb J. L. and Ippolitia J. T., 2008, Synthesis of novel oxazolidinone antimicrobial agents, *Bioorg. Med. Chem.*, **16**, pp. 2651–2656.
- [20] Demirbas, N., Ugurluoglu, R., Demirbas, A., 2022, Synthesis of 3-Alkyl (Aryl)-4-alkylidenamino-4,5-dihydro-1H-1,2,4-triazol-5-ones and 3-Alkyl-4-alkylamino-4,5-dihydro-1H-1,2,4-triazol-5-ones as Antitumor Agents, *Bioorg. Med. Chem.*, **10**, pp. 3717.
- [21] Avramova, P., Danchev, N., Buyukliev, R., Bogoslovova, T., 1998, Synthesis, toxicological, and pharmacological assessment of derivatives of 2-aryl-4-(3-arylpropyl) morpholines. *Arch. Pharm.*, **331**, pp. 342–346.
- [22] Lebouvier, N., Giraud, F., Corbin, T., MinNa, Y., Baut, Le, G., Marchanda, P., Borge Le, M., 2006. Synthesis, structural determination and photo-antiproliferative activity of new 3-pyrazolyl or isoxazolyl substituted 4-hydroxy-2 (1H)-quinolinones. *Tetrahedron Lett*. **47**, pp. 6479–6483.
- [23] Fang, K. C., Chen, Y. L., Sheu, J. Y., Wang, T. C., Tzeng, C. C., 2000. Synthesis, antibacterial, and cytotoxic evaluation of certain 7-substituted norfloxacin derivatives. *J. Med. Chem.* **43**, pp. 3809.
- [24] Aher, N. G., Pore V. S., Mishra, N. N., Kumar, A., Shukla, P. K., Sharma, A., Bhat, M. K., 2009. Synthesis and antifungal activity of 1, 2, 3-triazole containing fluconazole analogues, *Bioorg. Med. Chem. Lett*. **19 (18)**, pp. 759–763.
- [25] Rezaei, Z., Khabnadideh, S., Pakshir, K., Hossaini, Z., Amiri, F., Assadpour, E., 2009. Design, synthesis, and antifungal activity of triazole and benzotriazole derivatives. *Eur. J. Med. Chem.* **44(11)**, pp. 3064–3067.

- [26] Holla, B.S., Udupa, K.V., 1991. Synthesis of Novel 5-Mercapto-striazolo[3,4-c]-as-triazino[5,6-b]indoles and Their Mannich Bases. *Heterocycles*, **32**, pp. 1081-1088.
- [27] Bhawsar, S.B., Mane, D.V., Shinde, D.B., Shingare, M.S., Deokate, A.S., Gangawane, L.V., 1996. Syntheses of 8-[(6'-Substituted1',3'-Benzothiazol-2'-Yl) Aminomethyl]-Substituted Hydrooxycoumarins And Their Antimicrobial Activity. *Indian J. Heterocycl. Chem.*, **6**, pp. 135-138.
- [28] Huang, Z.Y., Yang, J.F., Chen, Q., Cao, R.J., Huang, W., Hao, G.F., Yang, G.F., 2015, An efficient one-pot access to N-(pyridin-2-ylmethyl) substituted biphenyl-4-sulfonamides through waterpromoted, palladium-catalyzed, microwave-assisted reactions. *RSC Advances*, **5(92)**, pp.75182-75186.
- [29] Christophe, T. 2009. et al. High content screening identifies decaprenyl-phosphoribose 2' epimerase as a target for intracellular antimycobacterial inhibitors. *PLoS pathogens*, **5**, pp. 1000645.
- [30] *Clin Exp Immunol. PubMed*, 1977, 272-7.
- [31] Yang, F., Yu, L.Z.T., Diao, P.C., et al. 2019. Novel [1,2,4]triazolo[1,5-a]pyrimidine derivatives as potent antitubulin agents: design, multicomponent synthesis and antiproliferative activities. *Bioorg Chem.* **92**, pp. 103260.
- [32] Naaz, F., Haider, M.R., Shafi, S., Yar, M.S., 2019. Anti-tubulin agents of natural origin: targeting taxol, vinca, and colchicine binding domains. *Eur J Med Chem.* **171**, pp. 310-331.
- [33] Mirzaei, H., Emami, S., 2016. Recent advances of cytotoxic chalconoids targeting tubulin polymerization: synthesis and biological activity. *Eur J Med Chem.* **121**, pp. 610-639.
- [34] Close A. Benmohammed, D. Hadji, A. Guendouzi, Y. Mouchaal, A. Djafri, A. Khelil, 2021. *J. Electro. Mater.*, **50**, pp. 5282-5293, 10.1007/s11664-021-09046-9.
- [35] Mermer, A. Faiz, O. Demirbas, A. Demirbas, N. Alagu, muthu, M. S. 2019. Arumugam Piperazine-azole-fluoroquinolone hybrids: conventional and microwave irradiated synthesis, biological activity screening and molecular docking studies *Bioorg. Chem.*, **85**. pp. 308-318.
- [36] Wajda-Hermanowicz, K. Pieniączak, D. Zatajska, A. Wrobel, R. Drabent. K. 2015. A study on the condensation reaction of 4-amino-3,5-dimethyl-1,2,4-triazole with benzaldehydes: structure and spectroscopic properties of some new stable hemiaminals *Molecules*, **20**, pp. 17109-17131.
- [37] Akin, S. Ayaloglu, H. Gultekin, E. Colak A., Bekircan, O. Yildirim-Akatin, M., 2019. Synthesis of 1,2,4-triazole-5-on derivatives and determination of carbonic anhydrase II isoenzyme inhibition effects *Bioorg. Chem.*, **83**. pp. 170-179.
- [38] S. Joshi, N. Khosla, P. Tiwari 2004. *Bioorg. Med. Chem.*, **12** p. 571.
- [39] F. Lopes, R. Capela, J.O. Gonçalves, P.N. Horton, M.B. Hursthouse, J. Iley, C.M. Casimiro, J. Bom, R. Moreira, 2004. *Tetrahedron Lett.*, **45**, p. 7663.
- [40] Close B.S. Holla, B. Veerandra, M.K. Shivanada, B. Poojary, 2003. *Eur. J. Med. Chem.*, **38**, p. 759.
- [41] W. Malinka, P. Świątek, B. Filipek, J. Sapa, A. Jezierska, A. *Koll II Farmaco* 2005. **60**. p. 961



Optimization of Traffic Network Signal Durations with Heuristic Algorithm and the Effect of Number of Individuals

Cihan KARAKUZU ^{1,*} , Emin TOPAL ² 

¹ Department of Computer Engineering, Engineering Faculty, Bilecik Şeyh Edebali University, Bilecik, 11230, Turkey, **ORCID:** 0000-0003-0569-098X

² Department of Computer Engineering, Institute Graduate Programs, Bilecik Şeyh Edebali University, Bilecik, 11230, Turkey, **ORCID:** 0000-0001-6206-231X

Article Info

Research paper

Received : August 8, 2022

Accepted : December 27, 2022

Keywords

Differential Evolution Algorithm
Heuristics Algorithms
Modeling and Simulation
Traffic Lights Optimization
Traffic Network Simulation
Soft Computing

Abstract

In the traffic network that we frequently use in our daily life, the primary demand of people has been to reduce the time they spend in traffic and to travel to the points they want to reach as quickly as possible. Developing countries want to meet this demand with the least cost in order to meet this demand. This study aims to manage the traffic network with the best times by optimizing the traffic signal durations in order to minimize the travel time for a road network chosen as a benchmark. For the optimization process, it is aimed to run a population-based heuristic algorithm with different numbers of individuals and obtain the best travel time. With the help of an open-source code traffic simulation program, which was run by modeling the benchmark road network, the received traffic data was also visually analyzed and compared. The effects of the heuristic algorithms applied with different numbers of individuals on the travel times according to the starting-destination points were examined before and after the optimization. As a result of the study, it has been observed that travel times and traffic signal times can be reduced with heuristic algorithms. Based on both numerical metrics and visual results, it has been determined that optimized traffic light durations give better results than non-optimized ones.

1. Introduction

Traffic is the name given to the structure that includes various vehicles and the units that manage these vehicles, and that we have to use in order to travel to the points we want to reach in our daily life. In developing countries, the increasing number of vehicles and the inadequacy of road capacities for travel demands have led to an increase in the time spent on transportation and the problem of traffic road networks. It has been stated that the increased transportation times and the length of time spent in traffic have a negative effect on people and lead the authorities to seek to solve this problem [1]. The authorities, who are in search of different methods, have proposed methods such as expanding the road capacity, increasing the units that control the traffic instantly, and methods that are high in cost and open to human error [2]. However, since these methods are both costly and non-continuous applications,

searching for different solution methods is reasoning. Optimizing the traffic lights in the road network system stands out among them in terms of both cost-effectiveness and applicability. For this reason, many researches and studies have been carried out to optimize the related parameter of the traffic network and to minimize the travel time.

In the studies examined, it has been seen that heuristic approaches give very good results in optimizations for the traffic problem. For example, in [3], Rutger et al. aimed to find the best routes for vehicles and obtain the best travel times by using Ant Colony Optimization to optimize travel times. Jindal and Bedi, on the other hand, aimed to avoid congested roads and direct vehicles to less-used roads by using route information to minimize traffic congestion in a city using the Hybrid Ant Particle Optimization (IHAPPO) heuristic approach [4]. They tested it using SUMO for traffic simulation and reported that the travel time is reduced significantly. In [5], the authors aimed to solve the travel problem of congested

* Corresponding Author: cihan.karakuzu@bilecik.edu.tr



roads by applying low-level and high-level optimization operations on the test network of Allsop and Charlesworth [6]. The Allsop and Charlesworth test road network, which was used in many studies, was determined by the authors as a benchmark in optimization for this study. Sheffi et al. [7] performed signal duration optimization by keeping the traffic flows constant. Başkan et al. [8], on the other hand, aimed to minimize traffic signal durations reducing travel times to the most suitable level for vehicles with the two-layer optimization method called TRACOM, which they developed using the Allsop and Charlesworth road network. The authors drew attention to the importance of using traffic lights with optimized duration, where vehicles perform better than non-optimized traffic lights.

In the current literature, studies on traffic optimization continue. Control of traffic lights in a road network of a large city is an extremely complicated task. For this reason, it is observed that these studies are carried out with different perspectives on traffic. For instance, [9] shows that artificial neural networks and randomized algorithms of stochastic approximation allow building systems for traffic light operation control that take into account various non-linear stochastic relations between locally observed network loads. Another approach was proposed by Safadi and Haddad in [10]. They presented an optimal analytical solution coupling both traffic routing and signal control in a continuous-time model for simple traffic networks. Another analytical solution proposed in [11] is a two-stage model based on period-dependent area traffic signal control. From a different perspective, for intelligent traffic light control multi-agent broad reinforcement learning was used in [12]. For multi-intersection traffic signal control, a deep reinforcement learning-based cooperative approach was presented in [13]. In [14], introduced a traffic light scheduling algorithm called SmartLight that controls the competing traffic flows at the road intersections.

Heuristic algorithms come to the fore with their applicability in optimization processes and traffic problems. For example, in [15] Tong et al. compared two different heuristics in a simulation environment. Using a new hybrid algorithm, the authors carried out the study on a test road network. Abdalhaq et al. examined the effects of the Genetic algorithm, Tabu Search algorithm (TS), Particle Swarm Optimization and Stochastic Approach algorithms on a traffic model in the SUMO simulation program in [16]. Testing heuristics in different simulation environments, Gabriel et al. [17] examined the effect of model-based heuristics on traffic travel problems. The authors, who sought solutions with different heuristic approaches to solving nonlinear problems, stated the usability and efficiency of the algorithms [18] [19]. Akgüngör et al., on the other hand, aimed to develop

heuristic approaches and find the best travel time for scenarios with high traffic density in [20].

As can be understood from the literature summary given above, a wide variety of approaches and solutions have been presented in traffic optimization. In this study, a heuristic algorithm is used to optimize traffic light durations on a test traffic road network in a SUMO simulation environment. Among the heuristic algorithms, the DE algorithm, which stands out in terms of high performance and stable solution generation, was preferred. By integrating DE with SUMO, optimizing has been carried out by avoiding the drawbacks of multi-individual (swarm) heuristics, focusing on operating with only one individual, which is unusual for DE. The experimental results obtained were compared with those obtained in multi-individual operations.

2. Softwares and Methods Used in the Study

In this section, the programming languages, heuristic algorithm methods and additional programs used in the study are given.

2.1. Auxiliary softwares

The auxiliary softwares used within the scope of the study are briefly described below and their intended use is expressed.

a) *Programming language:* The Python programming language, which can be easily integrated with different programs and environments, stands out with its compilability and simple syntax compared to other languages.

b) *Extensible markup language (XML):* It is a language that is generally used for data exchange and has a hierarchical tree structure. XML markup language is also used in the SUMO program structure, and certain XML files are processed with data transfer to enable simulation. In this study, XML markup language is used to operate the simulation program and integrate the heuristic approach into the simulation while the optimization process is run.

c) *Operating Systems:* Analysis processes were carried out under the Windows operating system. It is widely used as the main operating system in our computers where code editor programs and SUMO simulation programs are installed.

The SUMO simulation program can be used on different operating systems. The main operating system was determined as Windows, but the Linux operating system was also used because the SUMO program was easier and faster to obtain data in the Linux operating system for obtaining the result data.

d) Source Code Editor: Visual Studio Code was used as a code editor program to compile Python programming language, edit XML markup language codes and process the obtained data. It has been used as a code editing environment for this study due to its easy-to-use and colorful interface.

e) Simulation of Urban Mobility (SUMO): SUMO is an open-source, free simulation environment for small or large-scale traffic systems. Developed by members of the German Aerospace Center, SUMO was released in 2001. SUMO is an open-source space-continuous road traffic simulator commonly used for testing vehicular networks [21] SUMO allows one to obtain outputs visually and provides analysis by creating the output of an XML file. In this study, real-time traffic network modeling was done by exchanging data with XML files. SUMO can automatically model country and city road networks with the help of Google Maps and it also allows to create different traffic scenarios manually. The most important reason why it was chosen as a simulation program in this study is that it can be easily integrated with other software languages and allows to reach results easily close to reality.

2.2. Heuristic method and SUMO simulation for a benchmark road network

Differential Evolution (DE) algorithm, which is a swarm-based heuristic approach, has been used to optimize traffic signal durations. The DE algorithm used in the solution of nonlinear problems has been determined as the heuristic approach because it is stable and easy to code. The algorithm discovered by Storn and Price in 1996 maintains its popularity today and is used in many

researches. In this study, it was used to determine the best light durations by running simulations with different numbers of individuals.

Developed by Allsop and Charlesworth in 1977, the road network is a test network used by researchers to aim to get the best travel time by passing specific routes to vehicles. The road network used in many studies in the literature was determined as a benchmark and simulated in the SUMO program.

The Allsop and Charlesworth road network has a total of 7 start and end points, 6 traffic light intersections, 23 road link indicators and 14 green light duration variables. In Figure 1, the image of the road network modeled in the SUMO environment is given. Numbered arrows correspond to lanes in which vehicles can move. The points starting with the letter A and progressing to the letter G represent the starting and destination points of vehicles.

The right of way given to vehicles for one or more lanes in traffic is called phase. There are 14 phases in the Allsop and Charlesworth test road network. Phase arrangements in the SUMO program are made with the help of the "Net.Edit" program, and sample phase arrangements for an intersection are given in Figure 2.

In the road network given in Figure 1, the right-of-way matrix for the indicated numbered arrows is given in Table 1. For example, at junction 1, the right of way is given to lanes 1 and 16 in the first phase. In the second phase, there is a right of way for lanes 1, 2 and 19. Likewise, there are 3 phases for junction 4, for example. In the first phase, the transition exists for routes 5, 11 and 12. There is a right of way for lanes 10 and 12 in the 2nd phase and lanes 5, 6 and 13 in the 3rd phase.

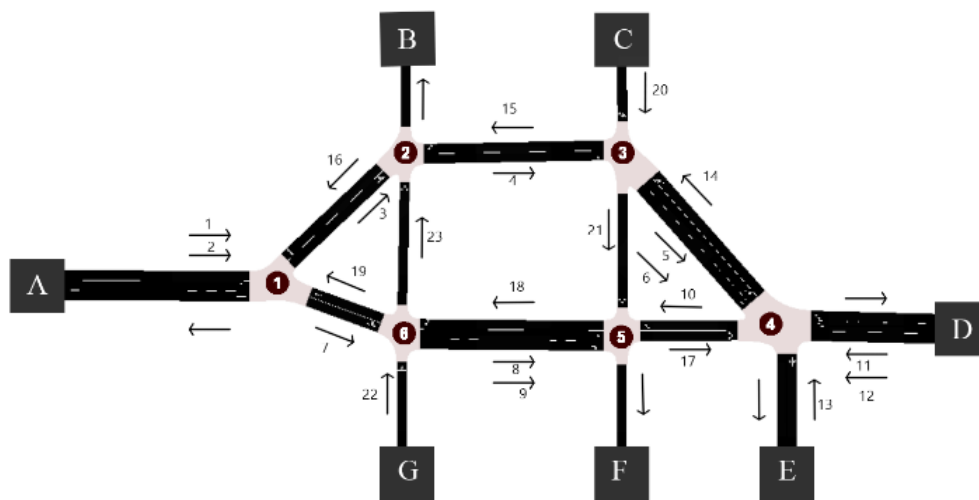


Figure 1. Allsop and Charlesworth road network modeled in SUMO environment

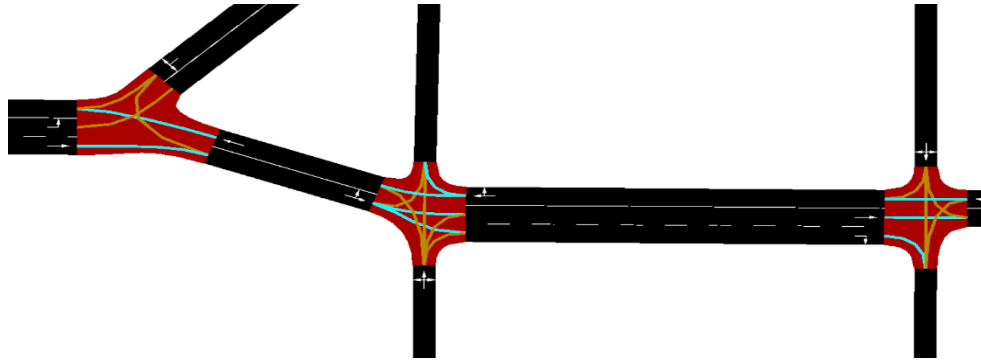


Figure 2. SUMO benchmark road network phase arrangements

Table 1. Road network phase matrix

J# \ Phases	1	2	3	4	5	6
Phase 1	1, 16	3, 15	20	5, 11, 12	8, 9	7, 18
Phase 2	1, 2, 19	23	4, 14	10, 12	8, 17	22
Phase 3	-	-	-	5, 6, 13	21	-

The sample traffic signal duration for the phases given in Table 1 is given in Table 2. According to the table, for example, a green signal time of 30 seconds is given in Phase 1 of traffic controller number 1. In phase 2, 20 seconds of green signal time is given for traffic controller number 1. The light duration (C) corresponds to the total green light duration.

Table 2. Example green signal duration matrix arranged by phase

Total Signal Duration (C)	Junction Number (i)	Phase 1 Green 1	Phase 2 Green 2	Phase 3 Green 3
50	1	30	20	-
70	2	20	50	-
80	3	30	50	-
120	4	40	40	40
110	5	20	40	50
70	6	30	40	-

2.3. Heuristic optimization of traffic signals

The first step of optimization signals of traffic networks defined in the previous subsections above is to determine the cost function used by the heuristic algorithm. The cost function used in the algorithm run throughout the simulation is given in Equation (1). The value of i in the equation shows the points where the vehicles starting the simulation from the T position can go as the destination point. The T position is given as the starting point, and the value of $J(T)$ represents the value of the cost function. In this study, since it is aimed to reduce travel time, the

individual quality calculation function given in Equation (1) was used.

$$J(T) = \sum_i \frac{(Time\ to\ reach\ T\ to\ i)(number\ of\ vehicles\ reaching\ i)}{(number\ of\ vehicles\ coming\ out\ of\ T)} \quad (1)$$

In order to obtain the best travel time on the road network, the population-based DE algorithm was run with different numbers of individuals and compared. The DE algorithm was operated with 1, 4, 6, 8 and 10 individuals in this study. For the problem-solving used in this study, all traffic signal phases were taken as a space dimension of the individual and a swarm consisting of 14 dimensional individuals was used. Each individual has phases of the traffic signal in size.

Due to its structure, the DE algorithm is operated by at least 4 individuals. In this study, apart from the conventional method, algorithmic calculations were carried out in the space dimension of a single individual. In the algorithm, 14-dimensional a single individual whose elements are the green light duration for each phase is used. Each element of the individual is used to generate a candidate individually, and the pseudo-code of the algorithm we used is given in Algorithm 1.

Individuals consisting of candidate traffic signal durations obtained with the running DE algorithm were subjected to balancing transactions in order to get meaningful values for the real world. Applicable values are obtained by proportioning very high signal times or very low signal times with the balancing process. Limiting conditions are given in Equation 2. According to the equation, C_{max} corresponds to the sum of the maximum green and red signal duration, C_{min} corresponds to the minimum total cycle value, Q_{min} corresponds to the minimum green light duration, Q_{max} corresponds to the maximum green signal duration, and Q corresponds to the green signal duration.

$$\left. \begin{aligned} C_{max} &\leq 120 \\ C_{min} &\geq 25 \\ Q_{min} &\geq 8 \\ Q_{max} &< C_{max} \\ Q_{min} &< Q < C_{max} \end{aligned} \right\} \quad (2)$$

In Figure 3, the flow chart showing the balancing transaction steps of the candidate individual obtained with the heuristic algorithm operated is given.

Optimization process was operated after integration of SUMO and DE algorithm. SUMO consists of three main files and uses that files created with XML tree structure [22]. In this study, Python file and SUMO XML files are interacted with each others in order to integrate the SUMO program and DE algorithm as given in Figure 4. The result values obtained by running SUMO simulation at

each algorithm step are sent to be used in the heuristic algorithm. In Figure 4, the working diagram of the SUMO files and the Python file in which the heuristic algorithm is implemented is given. According to the figure, “*yol.rou.xml*” containing vehicle information and “*yol.net.xml*” containing traffic signal durations were used for updating operations. The “*result.xml*” file is used for obtaining meaningful data to be used in the cost function, which outputs the SUMO simulation program.

Generate randomly initial individual elements in the interval of $[Q_{min}, C_{max}]$
Balance random assigned individual is balanced based on limitation of $C_{max}, Q_{max}, C_{min}$ and Q_{min}
Set mutation factor $F \in [0,2]$, crossover rate $CR \in (0,1)$
Do (Main Loop)
 Equalize candidate individual (U_{light}) and the main individual (X_{light})
 For each x_i element of a single individual ($x_i \in X_{light}$)
 Generate 3 random integers ($r_1, r_2, r_3 \in [1,D]$ and $r_1 \neq r_2 \neq r_3 \neq i$)
 Generate a random integer $j_{rand} \in [1,D]$
 $u_i \in U_{light}$

$$u_i = \begin{cases} x_{r1} + F(x_{r2} - x_{r3}) & \text{if } (rand \leq CR \vee i = j_{rand}) \\ x_i & \text{otherwise} \end{cases}$$

 Balance Candidate individual is balanced based on limitation of $C_{max}, Q_{max}, C_{min}$ and Q_{min}
 End For
 Calculate: Balanced U_{light} is sent to cost function and calculate travel time
 If candidate U_{light} is better than X_{light}
 $X_{light} = U_{light}$
 End If
Until: Stop criterion is met
Solution: The last individual found will be the solution to the problem.

Algorithm 1. Pseudo-code of DE algorithm run with a single individual

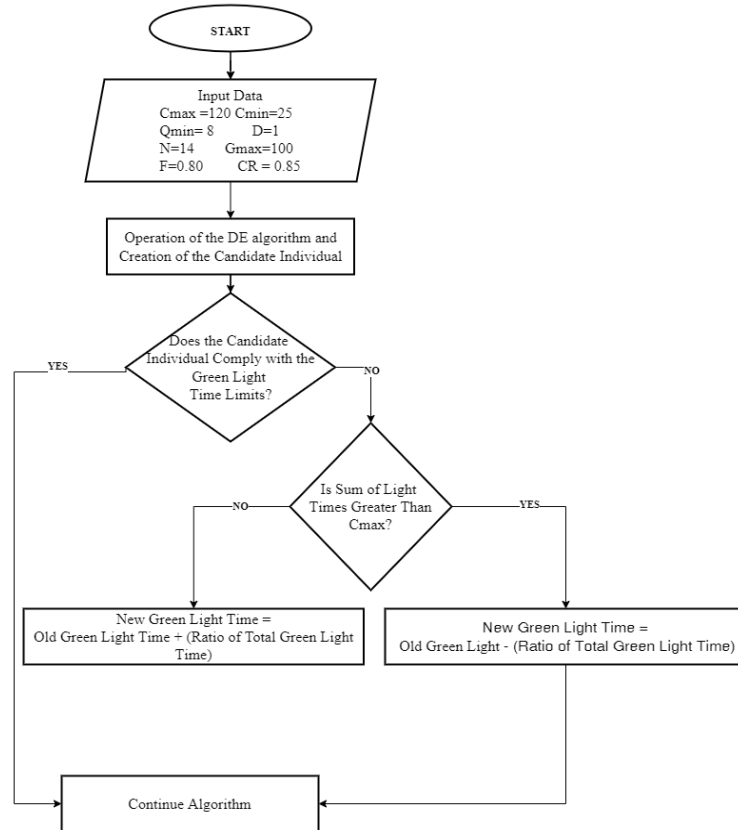


Figure 3. Transaction steps for balancing the traffic signal times

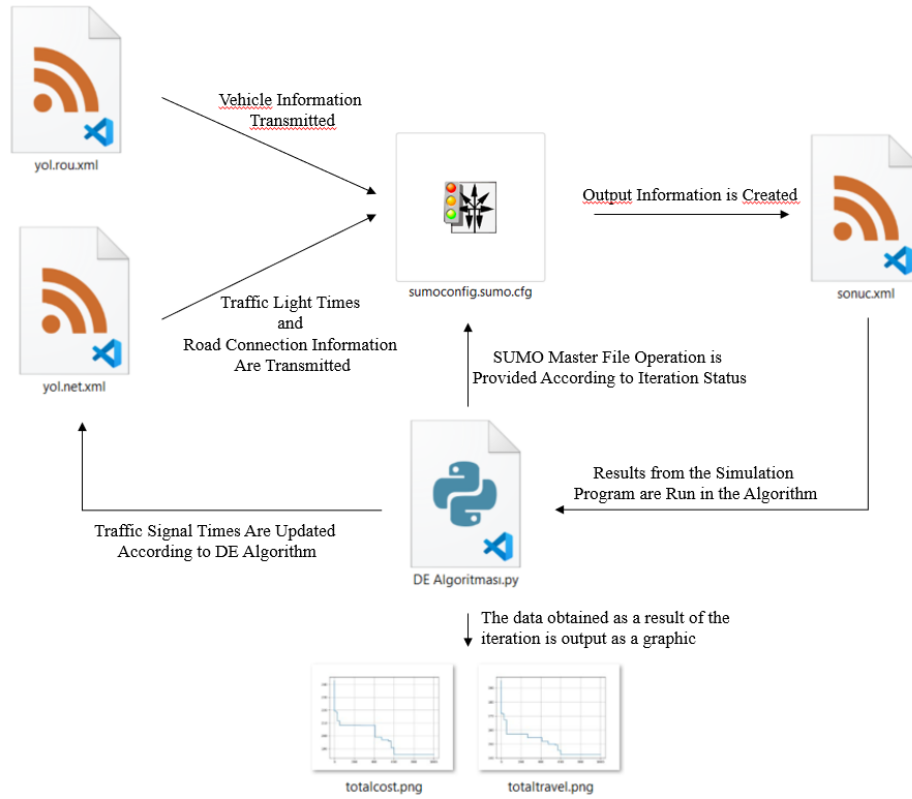


Figure 4. Integration scheme of SUMO and the heuristic approach

3. Experimental Results and Discussions

In this section, the performances before and after operated the algorithm are examined by applying the methods given above to the modeled benchmark road network. The optimized signal durations are examined both among themselves and with the pre-optimization data.

For the CR and F parameters, which are the basic parameters used in the DE algorithm, the CR = 0.85 and F = 0.80 values specified in [23] and suitable for the test road network were used. The DE algorithm was operated with 1, 4, 6, 8 and 10 individuals in this study. In an individual, the green signal duration of each phase was taken as an element as a space dimension of the individual. Hence, a swarm consisting of 14-dimensional individuals was used.

In Table 3, the number of vehicles in the traffic road network and the starting-arrival matrix of these vehicle numbers are given for each swarm size (1, 4, 6, 8 and 10). The initial traffic signal durations used on the benchmark road for each run of the approach proposed in this paper are given in Table 4.

Table 3. Starting-arrival matrix of vehicles used in the benchmark road network

Dest. \ Start	A	B	D	E	F	Total
A	0	250	700	30	200	1180
C	40	20	200	130	900	1290
D	400	250	0	0	100	750
E	300	130	0	0	20	450
G	550	450	170	60	20	1250

Table 4. Traffic signal durations before optimization

Total Light Durations C(s)	Traffic Light Number (i)	Phase 1 Green 1	Phase 2 Green 2	Phase 3 Green 3
100	1	50	50	-
100	2	50	50	-
100	3	50	50	-
120	4	40	40	40
120	5	40	40	40
100	6	50	50	-

In Table 5, the simulation results obtained with the signal durations in Table 4 and the number of vehicles in Table 3 are given in [23]. The resulting total travel time is 198.85 minutes. It is aimed to optimize the average vehicle arrival times based on the starting points given in Table 5.

Table 5. Average arrival times in minute before the optimization according to starting points

Starting Points	A	C	D	E	G	Total Time
Average Arrival Time	80,22	44,35	18,13	30,34	25,81	198,85

The optimized traffic signal durations obtained after 1000 iterations of the heuristic approach applied to the simulation model with swarm sizes of 1, 4, 6, 8 and 10 are given totally in Table 6. In each step of the DE algorithm, candidate individual balancing process and constraints were applied and real-world data were obtained. When the traffic signal times in Table 6 and the number of vehicles in Table 3 are used, the average arrival times of the vehicles are given in Table 7.

Table 6. Optimized traffic signal durations

Total Light Durations C(s)	Traffic Signal Number (i)	Phase 1 Green 1	Phase 2 Green 2	Phase 3 Green 3
With single individual/Swarm size=1				
67,510	1	33,51	34,00	-
71,880	2	48,82	23,06	-
67,670	3	35,71	31,96	-
114,810	4	40,00	34,81	40,00
116,970	5	42,54	45,63	28,80
67,560	6	46,07	21,49	-
With four individuals/Swarm size=4				
111,813	1	33,40	78,40	-
117,228	2	58,95	58,27	-
44	3	19,96	25,03	-
118,128	4	30,11	34,53	53,47
102,025	5	46,59	38,93	16,49
100,018	6	56,01	44	-
With six individuals/Swarm size=6				
115,281	1	44,65	70,62	-
76,531	2	42,40	34,12	-
114,386	3	46,29	68,09	-
120,000	4	38,28	43,63	38,07
116,537	5	42,82	44,69	29,02
91,017	6	51,09	39,92	-
With eight individuals/Swarm size=8				
88,394	1	30,70	57,68	-
108,687	2	64,04	44,64	-
102,185	3	44,47	57,71	-
98,302	4	14,95	37,33	46,01
115,262	5	58,63	33,69	22,93
98,650	6	60,80	37,84	-

Table 7. (Cont.) Optimized traffic signal durations

Total Light Durations C(s)	Traffic Signal Number (i)	Phase 1 Green 1	Phase 2 Green 2	Phase 3 Green 3
With ten individuals/Swarm size=10				
116.906	1	16.73	100.17	-
108.885	2	50.33	58.54	-
87.877	3	45.70	42.17	-
109.260	4	29.92	47.93	31.39
75.428	5	43.09	22.04	10.29
68.000	6	40.13	27.86	-

The average travel times after the optimization are given in Table 7. According to the table, it is seen that better times are obtained at the traffic light durations determined by the heuristic optimization compared to times before optimization given in Table 5. The best values obtained in the table are written underlined, and the percent values given under each value show gain (↓) or loss (↑) from the time obtained according to values of the before optimization situation. According to Table 5, as an example, the average travel time for point C, which was 44.35 minutes before the optimization, decreased to 30.52 minutes with the signal durations determined by the algorithm operated with a single individual. This value shows that 31.18% of the travel time is saved. For vehicles starting from point C, an increase of 7% was determined for the algorithm operated with four individuals and 3% for the algorithm operated with eight individuals, resulting in a loss in travel time.

Table 8. Average travel times in minute using signal durations optimized

Number of individuals (Swarm size)	Starting Points					Total Average Arrival Time
	A	C	D	E	G	
1	<u>48,84</u> ↓%39	<u>30,52</u> ↓%31	14,64 ↓%19	17,34 ↓%42	23,97 ↓%7	<u>135,31</u> ↓%32
4	70,54 ↓%12	47,50 ↑%7	14,73 ↓%19	17,95 ↓%41	<u>21,33</u> ↓%17	172,05 ↓%13
6	70,57 ↓%12	36,16 ↓%18	13,37 ↓%26	17,79 ↓%41	25,18 ↓%2	163,07 ↓%18
8	67,36 ↓%16	45,69 ↑%3	<u>11,61</u> ↓%36	<u>11,73</u> ↓%61	18,77 ↓%27	155,16 ↓%22
10	57,48 ↓%28	43,47 ↓%2	14,46 ↓%20	17,58 ↓%42	31,21 ↑%21	164,20 ↓%17

As can be seen in Table 7, the optimization with the best travel time was achieved with a single individual, and the worst travel time was obtained with 4 individuals. It is seen that the results of the optimizations made with 6, 8 and 10 individuals are close to those obtained with 4 individuals on the basis of total travel time. For points A

and C, the best results were obtained in a single-individual heuristic run. For points D, E and G, running with eight individuals gave the best results. While points D, E and G are narrower roads, points A and C are roads with wider lanes, and the number of individuals may show different effects according to road capacities.

In Figure 5, the instant traffic visuals corresponding to the 1.26 moment of the simulation done with the SUMO program using unoptimized signal durations are given. For the sake of comparison, the visual states of the simulation at the same simulation time for the two best cases in terms of the total average arrival times of the vehicles in Table 7 are given in Figure 6 and Figure 7, respectively. According to the pre-optimization traffic density visual given in Figure 5, when Figures 6-7 are examined after the optimization, it may be clearly seen that traffic density decreases. It has been determined that the proportional increase or decrease of the number of individuals does not increase or decrease the traffic density or indirectly travel time to a certain extent. In this context, it has been seen that the number of suitable individuals is among the parameters that should be carefully determined.

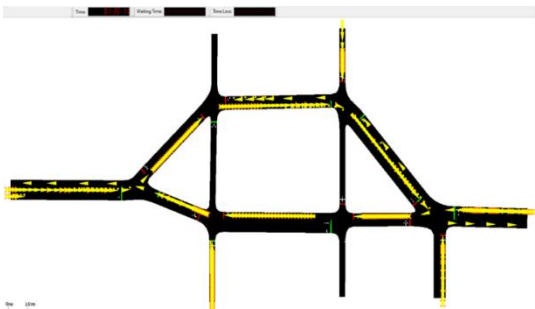


Figure 5. Traffic visual at the 1.26 moment of the simulation done with unoptimized traffic signal durations

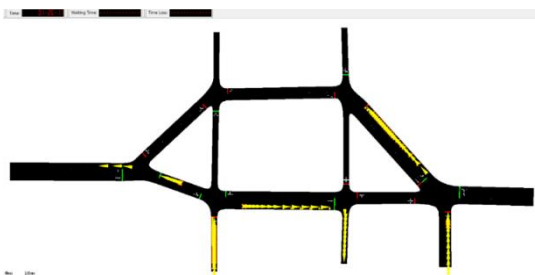


Figure 6. Traffic visual at the 1.26 moment of the simulation done with optimized traffic signal durations using only a single individual

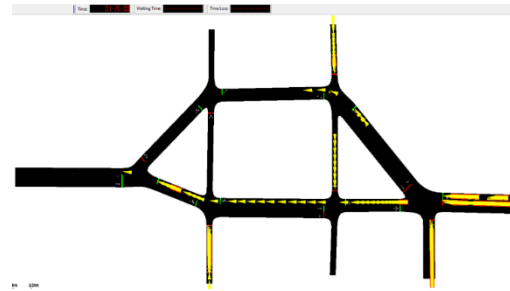


Figure 7. Traffic visual at the 1.26 moment of the simulation done with optimized traffic signal durations using a swarm of 8 individuals

In Figure 8, the training graph obtained as a result of the heuristic approach operated with different numbers of individuals is given. According to the graph, for example, there is a regular improvement for the algorithm run with a single individual and eight individuals. For the algorithm operated with four, six and ten individuals, no change was obtained after the first 10 iterations.

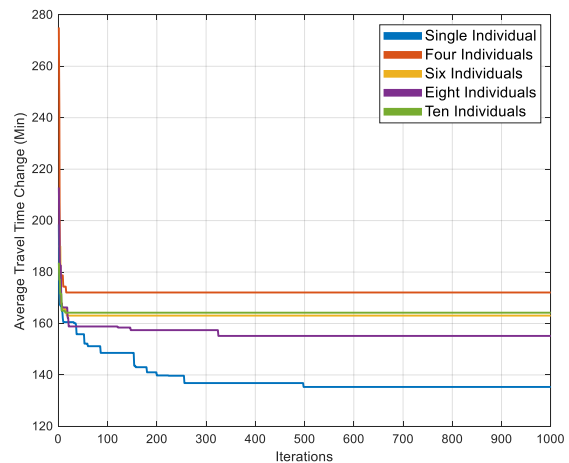


Figure 8. Training graph based on the number of individuals for the heuristic algorithm run with 1000 iterations

The average travel time of the vehicles leaving the starting points is given according to the number of individuals in Figure 9. According to the graph, for example, for vehicles starting from point A, it was seen that the time before optimization, which was 80.22 minutes, took the lowest value for a single individual. The first values in the graph where the number of individuals is 0 correspond to the values before the optimization.

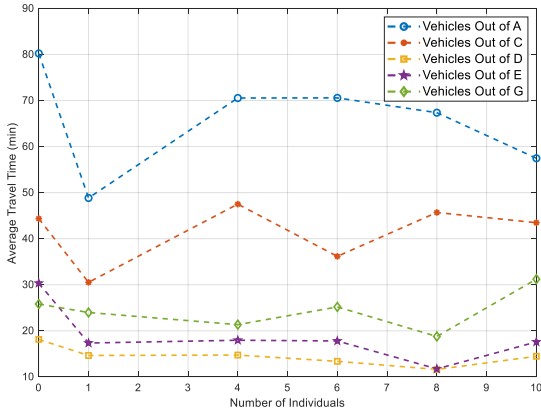


Figure 9. Change in the average travel time of vehicles leaving their starting points according to the number of individuals

In Figure 10, the average travel time bar graph is given according to the exit points of the vehicles that started their journey. According to the figure, for example, for point A, the best value of the average travel time is the algorithm run with a single individual colored orange, and the worst is the travel time before the optimization.

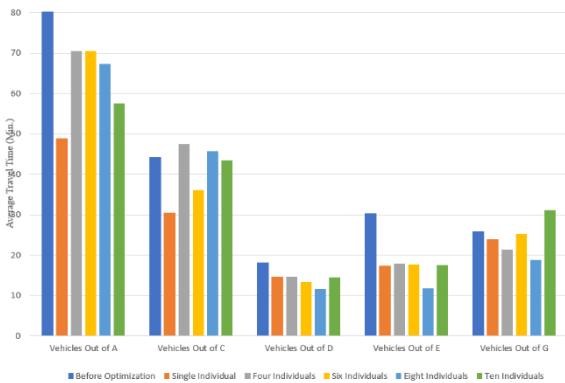


Figure 10. Average travel time bar graph by individual number of vehicles leaving their starting points

In Figure 11, the variation of the total average travel times depending on the number of individuals is given in the form of a line graph. According to the figure, the 0 point where the number of individuals is not present represents the travel time before the optimization. As the number of individual increase, the change in the average travel time changes in a fluctuating manner and it has been observed that a result is not obtained in proportion to the large or small number of individuals. It can be understood from this graph that the number of individuals is important for the optimization of the problem.

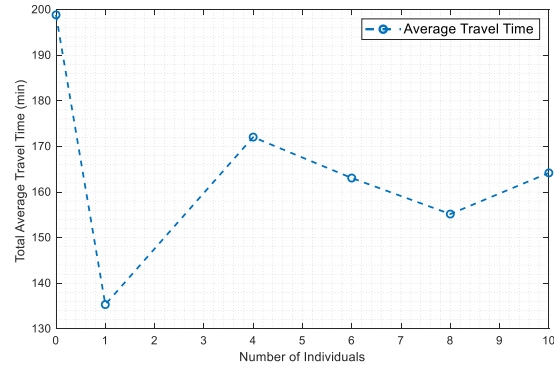


Figure 11. Variation of total average travel times depending on the number of individuals

In Figure 12, the completion time graph of the road network traffic signal durations optimization process, which is operated according to the number of individuals, is given. For example, when the algorithm operated with 4 individuals is used, the average completion time of an iteration is 2.02 minutes, and as a result of 1000 iterations, this time is calculated as 2020 minutes. When the algorithm operated with a single individual is used, it has been observed that the application of balancing processes in each dimension of the individual increases the completion time of the optimization process.

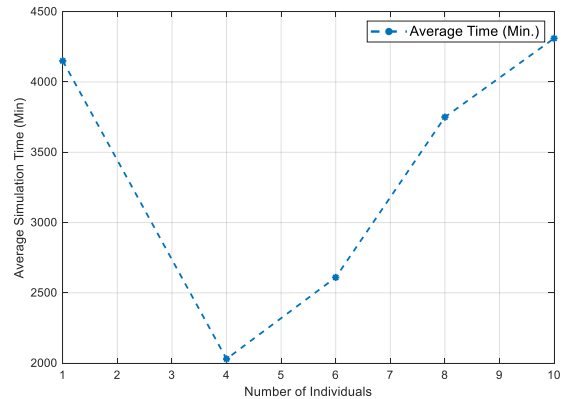


Figure 12. Completion time graph of the optimization process according to the number of individuals (1000 iterations)

4. Conclusion

With the study carried out, first of all, it has been shown that traffic light times can be optimized with a heuristic approach. Although the traffic optimization process is done in a simulation environment, it can take a long time. The operation of swarm-based heuristic algorithms with a large number of individuals, that is, with large swarm sizes unfortunately, increases this optimization process dramatically. Based on this

determination, in this study, we focused on operating a heuristic algorithm with a single individual in order to reduce the optimization process. It is very unusual to work with a single individual for the DE algorithm, which is one of the heuristic algorithms that stands out with its easy applicability, performance and stability, and was deliberately chosen to be used in this study due to these features. Because the algorithm has a structure to work with at least 4 individuals. The most valuable contribution of this study is to demonstrate the usability of DE for optimization by running it with only one individual. Another contribution is to examine the effect of the number of individuals on the optimization with the heuristic approach based on the optimal traffic light duration determination problem studied here. It has been shown that the number of individuals is a very effective parameter in the optimization processes in heuristic algorithms and directly affects the optimization process. Based on the proportional change in the number of individuals, it did not affect the travel times proportionally. This shows us that too many individuals or too few individuals are not better and that it should be subjected to the optimization process for individuals as well as parameter optimization by making different experiments to determine the best number of individuals in each problem.

As a result of the study, positive results were obtained by gaining travel time according to the traffic scenario before the optimization in all the number of individuals. It has been observed that the difference in the number of individuals shows differences in the travel times of the main roads and side roads. It has been determined that the fixed-term traffic lights have lost their adequacy today and that supporting them with smart systems will be beneficial for everyone in the traffic network. In this context, it is recommended for future studies to adapt the optimized traffic signal times with smart systems, as was done in this study.

Declaration of Ethical Standards

The authors of this article declare that the materials and methods used in this study do not require ethical committee permission and/or legal-special permission.

Conflict of Interest

The authors declare that they have no known competing financial interests or personal relationships that could have appeared to influence the work reported in this paper.

Acknowledgements

For his support in understanding the traffic network and related concepts used in this study, the authors would like to thank Dr. Hasan BOZKURT.

References

- [1] Pan J., Popa I. S., Zeitouni K. and Borcea C., 2013. Proactive Vehicular Traffic Rerouting for Lower Travel Time. *IEEE Transactions on Vehicular Technology*, **62** (8), pp. 3551-3568.
- [2] Namlı R., 2015. Köprülü kavşaklar ve trafik güvenliği. *Erciyes Üniversitesi Fen Bilimleri Enstitüsü Fen Bilimleri Dergisi*, **31**(2), pp. 129-134.
- [3] Claes R. and Holvoet T., 2011. Ant Colony Optimization Applied to Route Planning Using Link Travel Time Predictions. 2011 IEEE International Symposium on Parallel and Distributed Processing Workshops and Phd Forum, 16-20 May, pp. 358-365.
- [4] Jindal V. and Bedi P., 2018. An improved hybrid ant particle optimization (IHAPSO) algorithm for reducing travel time in VANETs. *Applied Soft Computing*, **64**, pp. 526-535.
- [5] Chiou S. -W., 1998. Bi-level formulation for equilibrium traffic flow and signal settings. *Mathematics in Transport Planning and Control*. Emerald Group Publishing Limited, Bingley, pp. 59-68.
- [6] Allsop R. E. and Charlesworth J. A., 1977. Traffic in a signal-controlled road network: An example of different signal timings including different routing. *Traffic Engineering & Control*, **18**(5), pp. 262-264.
- [7] Sheffi Y. and Powell W. B., 1983. Optimal signal settings over transportation networks. *Journal of Transportation Engineering*, **109**(6), pp. 824-839.
- [8] Başkan Ö., Ceylan H., Ozan C., 2020. Investigating Acceptable Level of Travel Demand Before Capacity Enhancement for Signalized Urban Road Networks. *Teknik Dergi*, **31**(2), pp. 9897-9917.
- [9] Krylatov A., Puzach V., Shatalova N., Asaul M., 2020. Optimization of traffic lights operation using network load data. *Transportation Research Procedia*, **50**, pp. 321-329.
- [10] Safadi Y., Haddad J., 2021. Optimal combined traffic routing and signal control in simple road networks: an analytical solution. *Transportmetrica A Transport Science*, **17**(3), pp. 308-339.

- [11] Chiou S.W., 2019. A two-stage model for period-dependent traffic signal control in a road networked system with stochastic travel demand. *Information Sciences*, **476**, pp. 256-273.
- [12] Zhu R., Li L., Wu S., Lv P., Li Y., Xu M., 2023. Multi-agent broad reinforcement learning for intelligent traffic light control. *Information Sciences*, **619**, pp.509-525.
- [13] Haddad T.A., Hedjazi D., Aouag S., 2022. A deep reinforcement learning-based cooperative approach for multi-intersection traffic signal control, *Engineering Applications of Artificial Intelligence*, **114**, 105019.
- [14] Younes M.B., Boukerche A., De Rango F., 2022. SmartLight: A smart efficient traffic light scheduling algorithm for green road intersections. *Ad Hoc Networks*, 103061.
- [15] Tong C. O. and Wong S. C., 2010. Heuristic algorithms for simulation-based dynamic traffic assignment. *Transportmetrica*, **6**(2), pp. 97-120.
- [16] Abdalhaq B. K. and Baker M. I. A., 2014. Using meta heuristic algorithms to improve traffic simulation. *Journal of Algorithms*, **2**(4), pp. 110-128.
- [17] Rodrigues de Campos G., Falcone P., Hult R., Wymeersch H. and J. Sjöberg, 2017. Traffic coordination at road intersections: Autonomous decision-making algorithms using model-based heuristics. *IEEE Intelligent Transportation Systems Magazine*, **9**(1), pp. 8-21.
- [18] Erdoğan P., 2018. A New Solution Approach for Non-Linear Equation Systems with Grey Wolf Optimizer. *Sakarya University Journal of Computer and Information Sciences*, **1**(3), pp. 1-11.
- [19] Yüzgeç U. and İnaç T., 2016. Adaptive Spiral Optimization Algorithm for Benchmark Problems. *Bilecik Şeyh Edebali Üniversitesi Fen Bilimleri Dergisi*, **3**(1), pp. 8-15.
- [20] Akgüngör A., Yılmaz Ö., Korkmaz E., Doğan E., 2019. Meta-Sezgisel Yöntemlerle Sabit Zamanlı Sinyalize Kavşaklar için Optimum Devre Süresi Modeli. *El-Cezeri Journal of Science and Engineering*, **6**(2), pp. 259-269.
- [21] Bautista P.B., Aguiar L.U., Igartua M.A., 2022. How does the traffic behavior change by using SUMO traffic generation tools. *Computer Communications*, **181**, pp. 1-13.
- [22] Krajzewicz D., 2010. Traffic simulation with SUMO—simulation of urban mobility. In: Barceló, J. (eds) *Fundamentals of Traffic Simulation*. *International Series in Operations Research & Management Science*, **145**, pp. 269-293.
- [23] Topal E., Karakuzu C., Bozkurt H., 2021. Denektaşı bir yol-kavşak ağı için basit bir sezgisel yaklaşım ile trafik ışık sürelerinin eniyilenmesi. *Cukurova 7th International Scientific Researches Conference*, Adana, Türkiye, 7- 8 September, pp. 1149-1164.

